Superconducting Single Photon Imaging X-ray Spectrometers

A Dissertation
Presented to the Faculty of the Graduate School
of
Yale University
in Candidacy for the Degree of
Doctor of Philosophy

by
Stephan Friedrich
December 1997

Dissertation Director: Prof. D. E. Prober

Abstract

Superconducting Single Photon Imaging X-ray Spectrometers

Stephan Friedrich

Yale University

1997

X-ray detectors based on superconductor-insulator-superconductor (SIS) tunnel junctions combine potentially high energy resolution with high absorption efficiency and intrinsic imaging capabilities. Photons absorbed in a superconductor generate excess charge carriers that can be detected as an increase in the subgap current of an SIS tunnel junction. If a single superconducting absorber is used with two detector junctions, one on either side, two signals are produced providing information on both x-ray energy and absorption location. We present the development of imaging x-ray spectrometers based on Nb-Ta-Al-AlOx-Al thin film structures for x-ray astronomy applications. At present, these detectors exhibit an energy resolution of 54 eV at 6 keV with a spatial resolution of 1 μm over a 30 μm range. This exceeds the best energy resolution of conventional semiconductor based devices by a factor of two, and provides effectively 30 pixels with just two channels of readout. In addition, these detectors have been used to study non-equilibrium quasiparticle dynamics in superconductors. A quantitative analysis of the device response is presented and is used to outline future device designs. Scaling to larger areas and significant improvements of the energy resolution appear possible.

Acknowledgments

Although there is a single name on its front page, this dissertation is very much the result of a collaborative effort with different researchers contributing their particular expertise to the overall result. It is my pleasure to thank my advisor Dan Prober for the guidance over the last six years, and for the freedom he gave me to develop my abilities as an independent researcher. I admire his ability to reduce complex problems to their essence, and I am grateful for his optimism and his confidence in the eventual success even at times when progress was stagnating.

I must also thank my thesis committee members: Bob Wheeler for his contagious enthusiasm and interest in science, Peter Kindlmann for his insight into the subtleties of innocuous looking amplifier circuits, Doug Stone for his help with the theoretical aspects of the work, and Mike Nahum from Harvard for serving as the outside reader.

I am indebted to our NASA collaborators Andy Szymkowiak and Harvey Moseley for their generous support. They have provided not only stable funding, but also direction and motivation for this work throughout the years. Without them, this research would not have been possible.

I enjoyed working with Ken Segall over the last three years. The shared interest in detectors and our countless discussions kept the project on track, and I am especially grateful for his help in the last few months. Ken has also written all the computer simulations. He and Chris Wilson will be a good team for the continuation of the project. Mike Gaidis deserves credit for the fabrication of the devices. His unwavering opinions still serve as a yardstick against which to measure new explanations. David Toledano and Ben Weiss also wrote some of the programs.

Dexter Crowley, Dave Johnson, Lou Berman, and Larry Foster provided reliable technical support, and Jayne Miller, Pat Brodka and the late Marilyn Shanahan made sure that the department was run smoothly.

My time at Yale would have been much less educational without my friends. Anurag Mittal kept my sanity during our first year at Yale and was a late night discussion partner on topics ranging from phase coherence to the meaning of life. Whye-Kei Lye served in that role during the last few months. I am glad to have met James Hanley, Josh Collins, Matthew Ryan and David Toledano, who all have contributed to making graduate student life enjoyable.

Most importantly, I would like to thank my parents who instilled the love of learning in me and laid the foundation that allowed me to pursue this degree. This thesis is dedicated to them.

Table of Contents

Acknowledgments iii

Table of Contents v

List of Figures vii

List of Tables x

List of Symbols and Abbreviations xi

Chapter 1: Introduction 1

1.1. Motivation 1

1.2. Current State of Research 3

Chapter 2: Overview 6

2.1. Superconducting Tunnel Junctions 6

2.2. Operating Principle 7

2.3. Device Design 15

2.4. Cryogenics 22

2.5. Data Acquisition 27

2.6. Time Scales 30

2.7. Current Pulse Simulations 38

Chapter 3: Electronics 45

3.1. DC current bias vs. DC voltage bias 45

3.2. Circuit design 48

3.3. Circuit performance 54

Chapter 4: Non-Equilibrium Quasiparticle Dynamics 60

4.1. Quasiparticle Generation 60

4.2. Quasiparticle Diffusion 67

4.3. Quasiparticle Trapping 73

4.4. Quasiparticle Tunneling........ 81
4.5. Quasiparticle Recombination........ 85
Chapter 5: Device Performance........ 92
5.1. Substrate Events........ 92
5.2. Digital Filtering........ 95
5.3. Device Resolution........ 97
5.4. Spatial Resolution........ 101
5.5. Discussion........ 104
Chapter 6: Summary........ 109

Appendix A: Materials Parameters in Tantalum and Aluminum........ 112
Appendix B: Summary of Important Runs........ 115
Appendix C: Summary of Device Parameters........ 116

References........ 117

List of Figures

2.1.1. Schematic of an SIS tunnel junction I(V) characteristic 7

2.2.1. Energy gap profile in trapping geometry 9

2.2.2. Energy gap profile and basic processes in double junction detector 9

2.2.3. Ideal charge output from double junction detector 10

2.2.4. Charge output for different trapping times 11

2.2.5. Charge output for different quasiparticle lifetimes 13

2.2.6. Energy gap profile and quasiparticle propagation including backtunneling 15

2.3.1. Device geometry 17

2.3.2. Critical current vs. magnetic field 19

2.3.3. Optical photographs of typical devices 21

2.4.1. Cross section of ^{3}He stage of the cryostat 24

2.4.2. Heat flow in ^{3}He stage of the cryostat 26

2.4.3. Temperature variation of subgap current 27

2.5.1. Change in bias point during pulse 29

2.6.1. Time scales for quasiparticle diffusion 30

2.6.2. Inelastic scattering times 32

2.6.3. Tunneling times 34

2.6.4. Thermal recombination times 35

2.7.1. Tunneling processes 39

2.7.2. Set of coincident pulses and their model fits 44

3.1.1. Device I(V) characteristics 46

3.1.2. Schematics of DC current bias and DC voltage bias circuits 47

3.1.3. Schematic of double junction voltage bias circuit 48

3.2.1. Amplifier gain characteristics vs. frequency 49

3.2.2. Circuit diagram for single junction readout 50

3.3.1. Amplifier noise characteristics 54

3.3.2. Bias dependence of low frequency noise 56

4.1.1. Energy distribution during initial relaxation process in tantalum.................... 62

4.1.2. Number distribution during initial relaxation process in tantalum (log scale)...... 62

4.1.3. Number distribution during the initial relaxation process (linear scale)............ 63

4.1.4. Energy relaxation in aluminum.. 65

4.2.1. Delay time measurements in tantalum.. 68

4.2.2. Delay time measurements in aluminum.. 69

4.2.3. Average non-equilibrium diffusion constant in tantalum.......................... 71

4.3.1. Fractional charge collection vs. trapping time.................................. 74

4.3.2. Charge output of tantalum device.. 75

4.3.2. Charge output of aluminum device.. 76

4.3.4. Gap profile in tantalum-aluminum bilayer.. 78

4.3.5. Quasiparticle multiplication upon trapping...................................... 80

4.4.1. Energy diagram for the various tunneling processes............................. 81

4.4.2. Non-equilibrium quasiparticle distribution in aluminum........................... 82

4.4.3. Bias dependence of peak current and charge..................................... 84

4.4.4. Charge output from center of absorber... 85

4.5.1. Charge output at different operating temperatures............................... 87

4.5.2. Peak currents at T = 0.24K... 88

4.5.3. Total collected charge vs. absorption location.................................. 89

4.5.4. Charge output from the center of the device vs. temperature...................... 91

5.1.1. Charge collection from substrate events.. 92

5.1.2. Device cross section including substrate... 93

5.1.3. Charge vs. distance for substrate events 94

5.2.1. Resolution of electronic pulses for different digital filters 96

5.2.2. Noise and signal spectra 96

5.3.1. Scatter plot Q_1 vs. Q_2 of filtered charge pulses 98

5.3.2. Total charge vs. absorption location 99

5.3.3. Device resolution over the entire length of the absorber 100

5.3.4. Device resolution over a 30 μm range 101

5.4.1. Histogram of absorption locations for localized irradiation 103

5.4.2. Proposed detector design to directly measure spatial resolution 103

5.5.1. Proposed detector design to eliminate quasiparticle losses at Nb contact 105

5.5.2. Charge profiles in y-direction 106

List of Tables

3.3.1. Projected circuit performance.. 58

4.1.1. Quasiparticle generation in tantalum and aluminum.................................. 66

4.2.1. Quasiparticle diffusion in tantalum and aluminum.................................... 72

App. A. Materials parameters for tantalum and aluminum.................................. 112

App. B. Summary of important runs...115

App. C. Device parameters of sample XN93..116

List of Symbols and Abbreviations

α	Loss parameter, $\alpha = L/\sqrt{(D\tau_{loss})}$
α	Phonon transmission coefficient into the substrate
A	Junction area
$\overline{\overline{A}}$	Tridiagonal matrix
A_{OL}	Open loop gain
β	Trapping parameter, $\beta = \sqrt{(\tau_{trap}/\tau_{loss})}$
β	Feedback reduction factor
B	Magnetic field
c	Speed of light
$\bar{c}$	Effective speed of light inside junction
c_{ph}	Phonon velocity
C_{in}	Total input capacitance
C_{jct}	Junction capacitance
C_F	Feedback capacitance
C_{FET}	Capacitance of the input FET
C_{leads}	Lead capacitance
C_V	Heat capacity
d	Film thickness
δ	Variance (of any parameter)
D	Diffusion constant
D_N	Diffusion constant in the normal state
D_{SC}	Diffusion constant in the superconducting state
Δ	Superconducting energy gap
e	Electron charge
e_n	Voltage noise density

ε	Average energy to create a single quasiparticle
E	Energy
E_{Debye}	Debye energy
E_F	Fermi energy
E_x	X-ray energy
f	Frequency
f_c	Cutoff frequency
$f(E)$	Fermi function
F	Fano factor
$F(f)$	Filter function of digital filter
FWHM	Full width at half maximum
g_m	Transconductance
γ	Linear coefficient of electronic specific heat
G	Fano factor for backtunneling
h	Planck's constant
$\hbar$	Planck's constant divided by 2π
i_n	Current noise density
I	Current
I_{bias}	Bias current
I_C	Critical current
I_{pair}	Current component carried by pairs
I_{qp}	Current component carried by quasiparticles
k_B	Boltzmann's constant
k_F	Fermi wavevector
λ	London penetration depth
$\lambda_{e\text{-}ph}$	Electron-phonon coupling constant
$\lambda_{e\text{-}e}$	Electron-electron coupling constant

L	Absorber length
L_{jct}	Junction length in direction perpendicular to the magnetic field
L_{trap}	Trapping length ($L_{trap}=\sqrt{D\tau_{trap}}$)
m^*	Effective electron mass
n	Particle density ($n=n(x,t)$)
n_{th}	Thermal quasiparticle density
$n(E_F)$	Normal metal density of states at the Fermi energy for both spin directions
n_{qp}	Quasiparticle density of states
N_{CE}	Total number of quasiparticles in the counterelectrode
N^i_{CE}	Number of quasiparticles in the counterelectrode at energy E_i
N^i_{qp}	Number of quasiparticles in the absorber at energy E_i
N^i_{ph}	Number of phonons in the absorber at energy E_i
N_{trap}	Total number of quasiparticles in the trap
N^i_{trap}	Number of quasiparticles in the trap at energy E_i
N_0	Number of initially created quasiparticles
N_x	Number of excess quasiparticles available for self-recombination
$P_{cooling}$	Cooling power
P_i, $i=1,2$	Tunneling probabilities out of electrode i of a tunnel junction
P_{in}	Input power into cold stage of dewar
Q	Charge
Q_0	Initial charge ($=eN_0$)
Q_1, Q_2	Charge collected in junction 1 and 2
Ω	Phonon energy
qp	Quasiparticle
R	Recombination coefficient per unit quasiparticle density
R_{Bias}	Bias resistance
R_{dyn}	Dynamic resistance of the junction at the bias voltage

R_F	Feedback resistance
R_{NN}	Normal state resistance of the tunnel junction
RRR	Residual resistance ratio
σ	Variance
σ_{Ntrap}	Variance of measured x-ray energy due to qp multiplication upon trapping
σ_{Nloss}	Variance of measured x-ray energy due to qp loss
t	Time
τ_0	Material specific time scale for electron-phonon interactions
τ_{diff}	Diffusion time
τ_{esc}	Phonon escape time into the substrate
τ_{esc}	Phonon escape time into the substrate
$\tau_{hotspot}$	Time for hotspot relaxation
τ_{loss}	Effective quasiparticle lifetime
τ_{out}	Time for quasiparticles to diffuse out of the counterelectrode volume
τ_{pb}	Pair breaking time
τ_{rec}	Thermal quasiparticle recombination time
$\tau_{rec,\ eff}$	Phonon enhanced recombination time
$\tau_{rec,\ self}$	Quasiparticle recombination time including self-recombination
τ_{trap}	Trapping time
τ_{tun}	Tunneling time
$\tau_{tun}^{i\rightarrow j}$	Tunneling time from initial energy i to final energy j
$\tau_{tun,\ CE}$	Tunneling time for tunneling from the counterelectrode
$\tau_{tun,\ trap}$	Tunneling time for tunneling from the trap
τ_s	Total inelastic scattering time through phonon emission
$\tau_s^{i\rightarrow j}$	Inelastic scattering time from initial energy i to final energy j
T	Temperature
T_{lr}	Tunneling matrix element

T_C	Critical temperature
v_F	Fermi velocity
V, V_{bias}	Bias Voltage
V_{out}	Preamplifier output voltage
V_n	Voltage of the n-th Fiske mode
x_0	Absorption location
Z	Atomic number
Z_{in}	Input impedance (R_{dyn}//C_{in})
Z_F	Feedback impedance (R_F//C_F)

Chapter 1: Introduction

1.1. Motivation

Scientific discoveries have often been facilitated by improved detection techniques. Many of these discoveries rely on the detection of photons or other single particles. In this dissertation we describe the development of high resolution single photon x-ray detectors with imaging capabilities for the energy range from 0.1 to 10 keV. These detectors are based on superconductor thin film technology. They rely on the absorption of an x-ray in a superconducting film and readout of the excess charge carriers with a superconductor-insulator-superconductor (SIS) tunnel junction.

Our research is motivated by space based x-ray astronomy applications. Stellar x-ray sources range from supernova remnants over active galactic nuclei and hot interstellar plasmas to binary systems [Charles, 1995]. X-ray astronomy would profit greatly from improved detector capabilities, as there are several interesting astrophysical questions that can not be adequately addressed with present technology. As an example [Gijsbertsen, 1995] consider intergalactic plasmas with temperatures of several million degrees that emit radiation in the soft x-ray band. Present day detectors with a resolution $E/\delta E \leq 50$ can resolve characteristic lines to deduce the elemental composition of the plasmas and their temperature. However, these results depend on assumptions about the processes that heat and maintain the plasmas at million degrees of temperature. Detectors with an energy resolution $E/\delta E \geq 200$ could provide model-independent information about the elemental abundances in hot plasmas. For an energy resolution $E/\delta E \geq 1000$, line profiles can be studied to examine the source velocity though measurements of the redshift.

Aside from higher energy resolution, it is highly desirable to have detectors with spatial resolution for focal plane imaging. Imaging is important not only for the analysis of

spatially extended sources; it also allows scanning the sky more quickly in surveys. Furthermore, the requirements on a detector are not only determined by astrophysical considerations. Equally important constraints arise from the fact that the atmosphere is opaque to x-rays and measurements have to be performed in a satellite or rocket where observation time is very expensive and the number of channels that can be used for data transmission is limited.

An ideal detector would combine the following characteristics. Most importantly it would combine high energy resolution $E/\delta E \approx 1000$ with imaging capabilities. High absorption efficiency is essential to image faint sources within the observation time constraints. On the other hand, a fast readout is desirable to improve the dynamic range of the detectors for imaging bright sources. The effective detector area should be large, preferably at least 5 mm by 5 mm, to allow for drifts in the grazing-incidence mirrors of the telescope.

Conventional detectors satisfy several of these requirements, but not all of them simultaneously. Crystal grating spectrometers offer high energy resolution, but are inefficient and can not be used to examine faint objects. They also provide only one dimensional imaging. Detectors based on semiconductor technology like charge-coupled devices (CCDs) have sufficiently high detection efficiencies and provide imaging over large effective areas, but their energy resolution is limited to about 100 eV for 6 keV x-rays.

Superconducting x-ray detectors based on tunnel junction technology have the potential to combine many of the desired features. Excitation energies in superconductors are of order meV, as compared to eV excitation energies in semiconductors. X-rays therefore generate 1000 times more free charge carriers in superconductors. This translates into a theoretical energy resolution limit that is predicted to improve upon existing semiconductor technology by more than an order of magnitude. At 6 keV the theoretical energy resolution is around 3 eV full-width at half-maximum (FWHM). High resolution at

6 keV is of interest for astrophysicists because characteristic iron x-ray lines fall into this energy range.

In addition, a single superconducting absorber can be used with two separate tunnel junction detectors for readout. In this geometry, the device has intrinsic imaging capabilities. Alternatively, one could of course use separate devices for imaging. However, this would require separate channels of readout for each individual device. This is impractical in space based applications. An essential advantage of the detectors discussed in this dissertation is that they provide imaging with a limited number of readout channels.

Other areas of research where improved photon/ particle spectrometers will provide new insights include dark matter searches, neutrino physics and material analysis. Novel applications in biophysics like for fluorescence spectra of metaloproteins are emerging. The field of low temperature detectors has experienced a rapid expansion during the last decade. It is likely to continue to grow with the continued need for higher sensitivity measurements.

1.2. Current State of Research

A variety of novel cryogenic detection schemes are presently being developed to improve the energy resolution of single photon x-ray detectors. Conference proceedings show the recent progress in this field [Brogiato, 1990; Booth, 1992; Labov, 1993; Girard, 1995; Ott, 1996]. Several approaches have yielded impressive results over the last decade. The most important ones for the benchmark 6 keV x-rays are summarized below.

Microcalorimeters measure the temperature increase of a thermistor upon x-ray absorption. Their performance is ultimately limited by thermodynamic fluctuations of the temperature. The NASA/Wisconsin collaboration has obtained a very high energy

resolution of 7.3 eV at 6 keV using doped silicon thermistors with a HgCdTe absorber [McCammon, 1991].

The same calorimetric principle can be used in superconducting transition edge bolometers. In these devices, the resolution can be further improved with the use of electrothermal feedback [Irwin, 1995a,b]. The group at NIST Boulder has measured 8 eV resolution at 6 keV with an Al/Ag bilayer biased at its transition [Wollmann, 1997].

If x-rays are absorbed in a normal metal that forms one electrode of a Superconducting-Insulator-Normal metal tunnel junctions (SIN), the excess subgap current provides an alternative measure of the resulting increase in the electron temperature. 6 keV x-rays have been detected with a 22 eV energy resolution at NIST using a Au/Ag absorber with an Al counterelectrode [Nahum, 1995].

Several other groups are pursuing the development of SIS junction detectors [e.g. Ott, 1996]. The best energy resolution attained so far with SIS tunnel junction detectors is 29 eV at 6 keV by the group at Lawrence Livermore using Nb-Al-AlOx-Al-Nb structures with a SQUID readout [Frank, 1996]. The same approach is being pursued by the European Space Agency, with a best result of 48 eV [Verhoeve, 1994]. Alternative materials systems that have been investigated at the Paul-Scherrer-Institute are Sn-SnOx-Sn junctions, which have yielded 65 eV resolution [Twerenboldt, 1986]. Experiments on Nb-Ta-Al-AlOx-Al-Nb devices at the Naval Research Laboratory show 60 eV resolution [Porter, 1996]. These devices, as well as all devices mentioned above, consist of a single pixel and do not offer imaging capabilities.

Double junction detectors for imaging have first been developed at the Technical University in Munich [Kraus, 1989a,b]. In fact, the early results on devices with Sn absorbers with Al-AlOx-Al readout junctions were largely responsible for exciting interest in tunnel junction detectors. The Munich group obtained an energy resolution of 60 eV with a simultaneous position resolution of 5 μm over an effective length of 53 μm. The resolution could be improved to 52 eV if the effective area was reduced. However, tin is a

soft metal and the devices could not be thermally cycled without damaging their properties. This is unacceptable for space based applications where extensive testing prior to launch is essential. Our work is an attempt to improve upon the Munich results by switching to a more stable all-refractory materials system.

This dissertation is organized as follows. Chapter 2 provides an overview of the operating principle and the processes involved in the charge detection. Device design for optimum detector performance and other experimental aspects of this work are discussed. Chapter 3 is concerned with how to optimize the readout electronics for minimum noise and waveform distortion. Chapter 4 follows with an analysis of the pulse waveforms to experimentally determine the time scales of the charge dynamics in the device. Chapter 5 shows the present performance of the device, discusses the limiting factors and suggests possible future experiments. Chapter 6 concludes with a summary of the results.

Chapter 2: Overview

2.1. Superconducting Tunnel Junctions

Superconductivity is the phenomenon of a vanishing electrical resistance in certain materials below a material-specific characteristic temperature T_C. In conventional superconductors, it occurs because of an attractive phonon mediated interaction between electrons [Bardeen, 1957]. Electrons condense into bound states at the Fermi energy called Cooper pairs. There is a finite binding energy associated with the Cooper pairs that manifests itself as an energy gap Δ by which the lowest lying single particle excitations are separated from the Cooper pairs. These excitations are called quasiparticles and their density of states is given by

$$n_{qp} = n(E_F)\left(\frac{|E|}{\sqrt{E^2 - \Delta^2}}\right). \qquad 2.1.1.$$

Here $n(E_F)$ is the density of states at the Fermi surface in the normal state and energies E are measured relative to the Fermi energy. The quasiparticle density of states diverges at the gap energy and is zero for lower energies. At finite temperature, some quasiparticles are thermally excited above the gap.

Tunnel junctions consist of two metals separated by an insulator. If the insulator is sufficiently thin, charges can traverse the barrier through quantum mechanical tunneling. A finite tunneling current results whenever filled states on the one side of the barrier face empty states on the other side. For normal metal electrodes the tunneling I(V) characteristics is linear with a resistance R_{NN}. For metals in the superconducting state and voltages below the gap voltage $2\Delta/e$, only thermally excited quasiparticles can tunnel and

contribute to the subgap current. Above that voltage, Cooper pairs can be broken resulting in a sharp current increase due to the divergent density of states. At high voltage, the I(V) characteristics asymptotically approaches the normal metal value.

In addition, there is a Cooper pair contribution to the dc current at zero voltage due to the Josephson effect [Josephson, 1962]. The magnitude and the polarity of the dc Josephson effect depends on the phase difference between the two superconductors on either side of the barrier. The Josephson current has a maximum value of $\pm I_C$ and can be suppressed with a magnetic field in direction parallel to the tunnel barrier. Suppressing I_C is necessary in order to stably bias a junction in the subgap region with a circuit whose load line resistance exceeds the normal state resistance R_{NN} of the junction. A schematic of a typical I(V) characteristic is shown in figure 2.1.1.

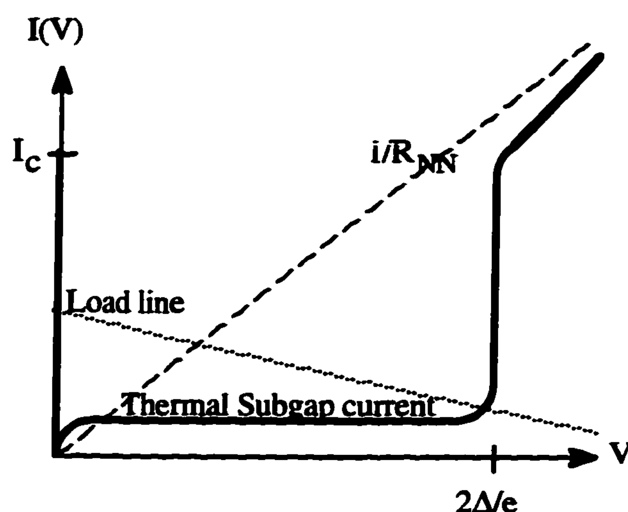

Figure 2.1.1.: I(V) characteristic of a Superconductor-Insulator-Superconductor (SIS) tunnel junction. In our system, the normal state resistance is typically around 0.5 Ω with a 6 Ω dc load line

2.2. Operating Principle

X-rays absorbed in a superconductor relax their energy in a complex cascade involving electron-electron scattering, electron-phonon scattering and pair-breaking. At the

end of the relaxation process, a certain fraction of the x-ray energy is converted into quasiparticles with energies just above the superconducting gap, and the remainder is lost to subgap phonons whose energy is insufficient to break any further Cooper pairs. The number N_0 of quasiparticles is proportional to the x-ray energy E_x. The average number and its standard deviation are given by

$$N_0 = \frac{E_x}{\varepsilon} \pm \sqrt{F\varepsilon E_x}. \qquad 2.2.1.$$

Here F is the Fano factor that characterizes the correlated nature of the quasiparticle generation [Fano, 1947; see also section 4.1.], and ε is the energy required to create a single quasiparticle. If the superconducting absorber forms one electrode of a superconductor-insulator-superconductor (SIS) tunnel junction, the quasiparticles can be detected as an increase in its subgap current. The energy resolution of such a detector is ultimately limited by the statistical fluctuations in the number of initially created quasiparticles. Since ε is of order the gap energy in superconductors and $F \approx 0.2$ [Kurakado, 1982], these detectors can have an energy resolution of a few eV for x-rays in the keV range. This is obtained if each quasiparticle is counted exactly once. The Fano limit for a typical superconductor is roughly 30 times better than the limit for semiconductor technology; this provides the principal motivation for our work.

The detectors need to fulfill two conflicting requirements. The absorber volume should be large for high absorption efficiency and large area coverage. The tunnel electrode volume should be small to ensure the quasiparticle tunnel before they recombine. This problem can be addressed by quasiparticle trapping through superconductor bandgap engineering [Booth, 1987]. A large superconducting absorber with high energy gap is used in conjunction with a small lower gap tunnel junction. Quasiparticles in the absorber that diffuse to the lower gap region scatter inelastically and are then confined close to the

tunnel barrier. Quasiparticle trapping separates absorber and detector functions and allows optimizing each one individually. The same concept is applied to prevent quasiparticles from diffusing from the absorber into the electrical contacts. A large gap superconducting contact will reflect quasiparticles at the interface, provided that they have scattered below the contact's gap edge (figure 2.2.1.).

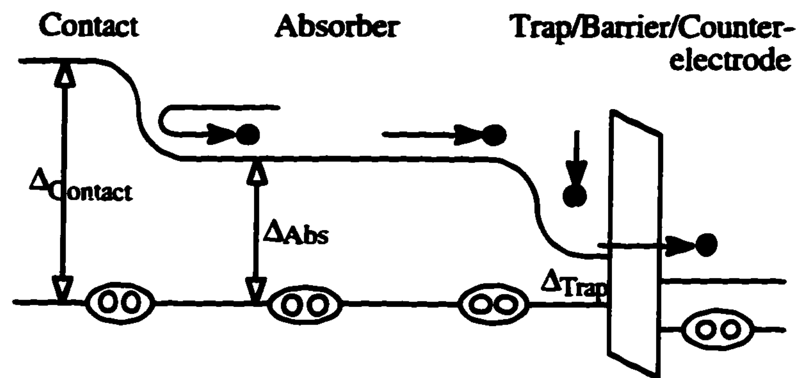

Figure 2.2.1. Energy gap profile in trapping detector with bandgap engineering

To use such a trapping detector in an imaging configuration, two detector junctions are connected to a single superconducting absorber, one on either side [Kraus, 1989a,b]. Quasiparticles created in the absorber by a single x-ray will split up diffusively and will be trapped and produce signals in both junctions (figure 2.2.2.).

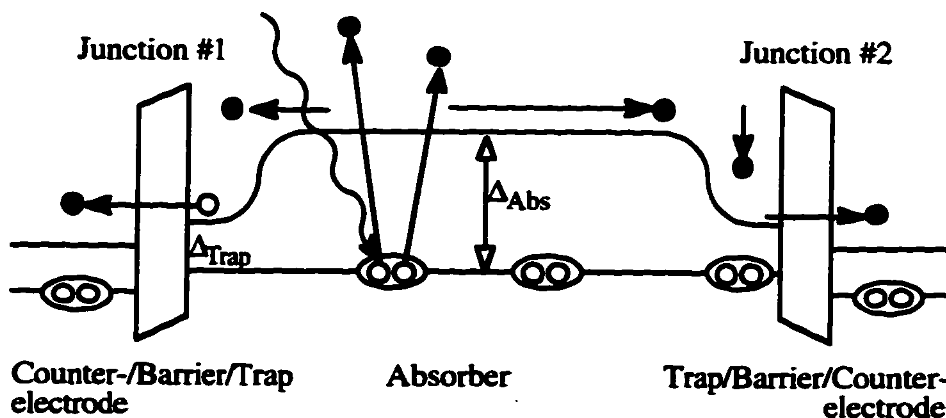

Figure 2.2.2.: Schematic of the energy gap profile and the basic processes involved in a double junction x-ray detector

The sum of the signal charges is related to the x-ray energy, and their ratio provides information about the absorption location. Plots of the two detected charges like the one shown schematically in figure 2.2.3. then reveal both energy and location of the absorbed photon. This way, position information can be obtained with just two channels of readout.

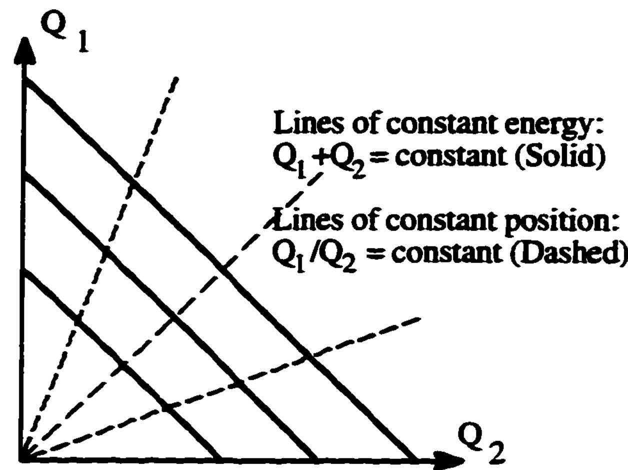

Figure 2.2.3.: Ideal charge output (no loss) from an imaging double junction detector for irradiation with different energy x-rays.

Analytic Solutions

For a more general quantitative analysis of such a double junction detector consider an absorber of length L with traps on either side at $x=\pm L/2$. An x-ray is absorbed at time t=0 and position $x=x_0$. The dynamics of the quasiparticle distribution n(x,t) inside the absorber can be described by a standard diffusion equation including a term for quasiparticle loss on a time scale of τ_{loss} to account for the finite quasiparticle lifetime. Since the process of quasiparticle generation is fast on time scale of the diffusion inside the absorber, the initial distribution can be assumed to be point-like. Quasiparticles at the absorber-trap interfaces at $\pm L/2$ will diffuse into the trap over a characteristic length $L_{trap} = \sqrt{D\tau_{trap}}$ before scattering inelastically. Setting the diffusion current $D\partial n/\partial x$ at the interface equal to $n(\pm L/2)L_{trap}/\tau_{trap}$ determines the boundary condition at the absorber-trap interface. The resulting differential equation

$$\frac{\partial n(x,t)}{\partial t} = D\frac{\partial^2 n(x,t)}{\partial x^2} - \frac{n(x,t)}{\tau_{loss}}$$

$$\text{with } n(x,t=0) = N_0\delta(x - x_0) \quad \text{and} \quad \left.\frac{\partial n}{\partial x}\right|_{x=\pm L/2} = \frac{n|_{x=\pm L/2}}{L_{trap}} \qquad 2.2.2.$$

can be solved analytically [Jochum, 1993]. The charges Q_1 and Q_2 collected in the two detector junctions in the most general case of finite trapping time and finite quasiparticle life time is found to be

$$Q_{1/2}(x_0) = Q_0\frac{\sinh(\alpha(1/2 \pm x_0)) + \beta\cosh(\alpha(1/2 \pm x_0))}{(1+\beta^2)\sinh(\alpha) + 2\beta\cosh(\alpha)}, \qquad 2.2.3.$$

where $Q_0=eN_0$ is the total charge initially created by the absorption of the x-ray. The parameter $\alpha\equiv\sqrt{(\tau_{diff}/\tau_{loss})}$ with $\tau_{diff}\equiv L^2/D$ reflects competing mechanisms of quasiparticle diffusion and loss in the absorber. Similarly, $\beta\equiv\sqrt{(\tau_{trap}/\tau_{loss})}$ is a measure for the relative time scales of trapping and loss. Figure 2.2.4. shows a plot of the charge output from different events for uniform illumination of the absorber for $\alpha=1$ and different trapping times.

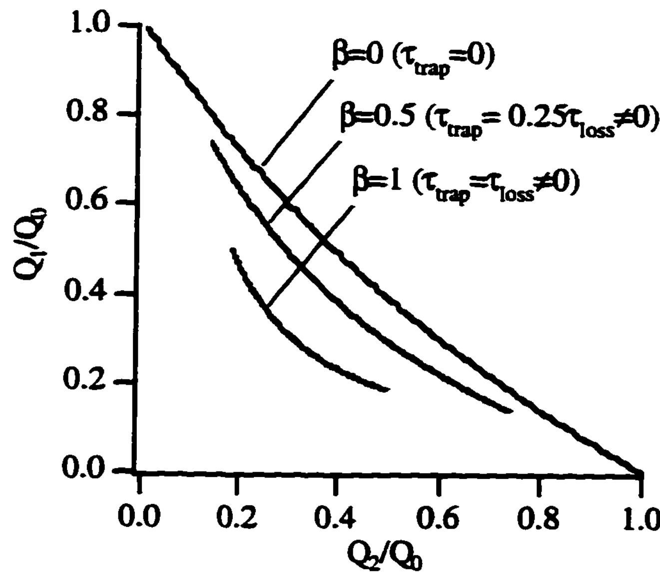

Figure 2.2.4.: Charge output for different trapping times τ_{trap}.

For longer trapping times, i.e., increasing β, even quasiparticles created close to one end of the absorber are not necessarily captured in the adjacent low gap region, but have a finite probability to diffuse to the opposite junction and produce a signal there. Slow trapping therefore manifests itself in a finite minimum charge and scatter plots not extending all the way to the axes. Slow trapping reduces the position sensitivity and enhances the effects of quasiparticle loss as the quasiparticles remain in the absorber longer before being detected.

A successful detector requires fast trapping for efficient charge collection and high spatial resolution. This requires clean absorber-trap interfaces for high quasiparticle transmission and fast inelastic scattering in the lower-gap trap region. In this limit ($\tau_{trap} \rightarrow 0$) the boundary condition at the absorber-trap interfaces reduces to $n(x=\pm L/2)=0$ and the charge output is given by [Kraus, 1989]

$$Q_{1/2}(x_0) = Q_0 \frac{\sinh(\alpha(1/2 \pm x_0))}{\sinh(\alpha)}. \qquad 2.2.4.$$

Figure 2.2.5. shows plots for three different values of $\alpha \equiv \sqrt{(\tau_{diff}/\tau_{loss})} = L/\sqrt{(D\tau_{loss})}$. If the quasiparticle lifetime is of the same order as the time $\tau_{diff} \equiv L^2/D$ it takes the charges to diffuse to the trap, quasiparticles created in the center of the absorber are more likely to recombine before being detected. This produces a reduced charge output from the center of the device and some curvature in the scatter plot. The curvature is used to determine α experimentally.

Equation 2.2.4. for the measured charges Q_1 and Q_2 allows us to infer the initial charge Q_0 and the absorption location x_0 even in the presence of quasiparticle loss in the absorber. Solving for Q_0 and x_0, one finds

$$Q_0 = \sqrt{Q_1^2 + Q_2^2 + 2Q_1Q_2\cosh(\alpha)}$$
$$x_0 = \frac{L}{2\alpha}\ln\left(\frac{Q_1 e^{-\alpha/2} + Q_2 e^{\alpha/2}}{Q_1 e^{\alpha/2} + Q_2 e^{-\alpha/2}}\right) \qquad 2.2.5.$$

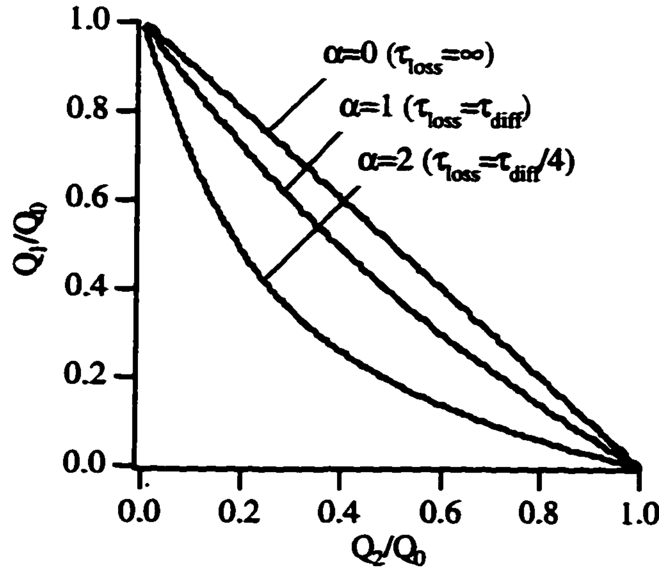

Figure 2.2.5.: Charge output for different quasiparticle lifetimes τ_{loss}.

For negligible quasiparticle loss, i.e. $\alpha=\sqrt{(\tau_{diff}/\tau_{loss})}\rightarrow 0$, these equations reduce to

$$
\begin{aligned}
Q_0 &= Q_1 + Q_2 \\
x_0 &= \frac{L}{2}\frac{Q_1 - Q_2}{Q_1 + Q_2}
\end{aligned}
\qquad 2.2.6.
$$

This corresponds to the ideal case shown already in figure 2.2.3. in which every quasiparticle generated in the initial energy relaxation process is counted exactly once. The average distance $\sqrt{(D\tau_{loss})}$ over which quasiparticles diffuse before recombining must ideally be much larger than the absorber dimension L. That requires absorber films of high purity for large diffusivity D and operation at low temperatures such that thermal recombination does not limit the quasiparticle lifetime. Quasiparticle loss not only reduces the charge signal, but also introduces additional uncertainty σ_{Nloss} to the energy measurement, because there are fluctuations in the number of quasiparticles lost in different events.

Fluctuations

There are other processes that can introduce noise. The first is related to the gap difference between absorber and trap. If the gap in the absorber exceeds the gap in the trap by at least a factor of 3, phonons emitted upon trapping can have an energy greater than $2\Delta_{trap}$. This is sufficient to break pairs in the trap and create additional quasiparticles [Booth, 1987]. Statistical fluctuations in this number will also introduce an additional uncertainty σ_{Ntrap} to the x-ray energy measurement [Mears, 1993].

The second is due to a process called backtunneling or Gray effect [Gray, 1978] and is illustrated in figure 2.2.6.. Quasiparticles in the counterelectrode that are scattered to the gap edge can no longer reverse tunnel directly, as they face the energy gap on the other side of the barrier. They can, however, break Cooper pairs in the trap to form another pair in the counterelectrode. This process is called backtunneling as it transfers an unpaired quasiparticle back into the trap, but transfers net charge in the *same* direction as the direct forward tunneling process. Forward tunneling and backtunneling can continue to multiply the detected charge until the quasiparticles either recombine or diffuse into the leads. Since the individual tunneling events are uncorrelated, fluctuations in the number of backtunneling events will be an additional source of noise [Goldie, 1994]. In the general case where the probabilities P_1 and P_2 for tunneling from the two films are different, the excess noise is given by

$$\sigma_{backtunneling} = \sqrt{\varepsilon E_x G} \text{ with } G = \frac{P_1 - P_1^2 + 3P_1P_2 + P_1^2P_2}{(P_1 + P_1P_2)^2}. \qquad 2.2.7$$

The tunneling probability $P = \tau_{tun}^{-1} / (\tau_{tun}^{-1} + \tau_{loss}^{-1})$ describes how likely a quasiparticle will tunnel across the barrier at a rate τ_{tun}^{-1} compared to leaving the junction electrode by any other process at a rate τ_{loss}^{-1}, be this due to recombination or outdiffusion. In the case where the tunneling probabilities are identical one obtains $G=1+\tau_{tun}/\tau_{loss}$, where τ_{tun}/τ_{loss} is the average number each quasiparticle tunnels across the barrier.

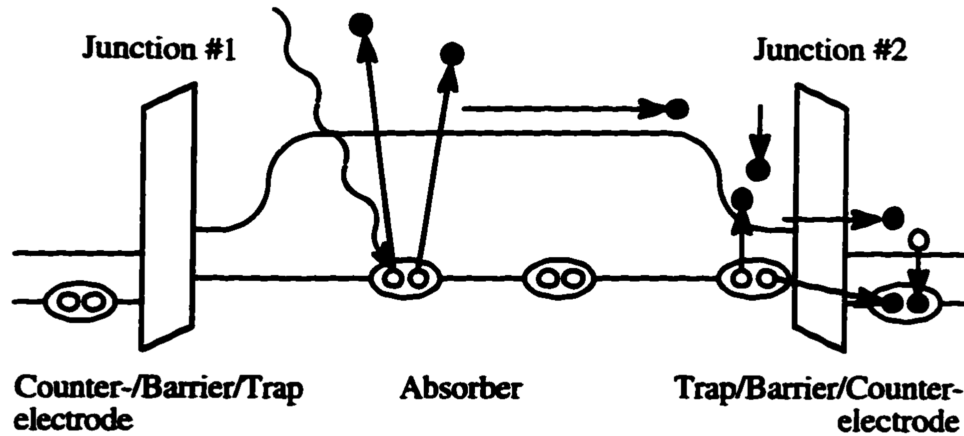

Figure 2.2.6.: Energy gap profile and quasiparticle propagation including backtunneling (Gray effect) in a double junction detector

Aside from the statistical processes outlined above, the device resolution can further be deteriorated by noise in the readout electronics or spatial variations of the detector response. The ultimate device resolution

$$E_{FWHM} = 2.355\sqrt{\varepsilon E_x(F+G) + \sigma^2_{Ntrap} + \sigma^2_{Nloss} + \sigma^2_{electronics} + \dots} \qquad 2.2.8.$$

will therefore only be Fano limited if all other sources of noise are sufficiently well suppressed.

2.3. Device design

The design of a single photon imaging x-ray spectrometer is guided by the need for high absorption efficiency, effective charge collection and device durability. Quasiparticle lifetimes have to be long on a time scale set by diffusion and tunneling. Trapping out of the absorber must be fast for high spatial resolution. Charge multiplication processes that add statistical noise should be eliminated. Separating absorber and detector function by using

quasiparticle trapping allows optimizing each of them individually. In this section we will summarize materials choices and device geometry as well as sample fabrication and device parameters. Details can be found in the dissertation of Mike Gaidis [Gaidis, 1994], who fabricated the devices that were used in this work.

Materials

Tantalum emerges as the absorber material of choice. Its high atomic number (Z=73) translates into the shortest absorption length of all superconducting materials with convenient T_C. Characteristic time scales for inelastic scattering and pair-breaking in tantalum predict a fast conversion of photon energy into excess quasiparticles. The intermediate gap size (Δ_{Ta} = 700 μeV) allows the use of a trapping configuration, and the quasiparticle lifetime is expected to be long at typical operating temperatures below 0.3K. Furthermore, unlike niobium, tantalum does not have metallic suboxides whose low energy gap would provide unwanted trapping sites in the absorber [Halbritter, 1987]. Other alternative absorber materials with short absorption lengths like lead or tin are not refractory and degrade with thermal cycling [Kraus, 1989].

Aluminum is chosen as a junction material, because its low energy gap (Δ_{Al} = 170 μeV) allows effective trapping at the absorber-trap interface. That does, however, make operating temperatures below 0.4 K necessary to ensure sufficiently long quasiparticle lifetimes in the trapping regions [Gray, 1971]. Aluminum also forms a robust insulating oxide needed to create a high quality tunnel barrier. It has a low atomic number (Z=13) and consequently few x-rays will be absorbed in the junction area directly.

To make electrical contact to the absorber, we use a thin strip of niobium, whose high energy gap (Δ_{Nb} = 1500 μeV) prevents quasiparticles from diffusing out into the leads. Possible trapping sites at metallic suboxides are only of concern if these oxides form right at the tantalum-niobium interface.

All materials are refractory and are not expected to degrade with time and thermal cycling. We did not observe any changes in the device's I(V) characteristics with time and repeated thermal cycling over a three year period.

Device Geometry

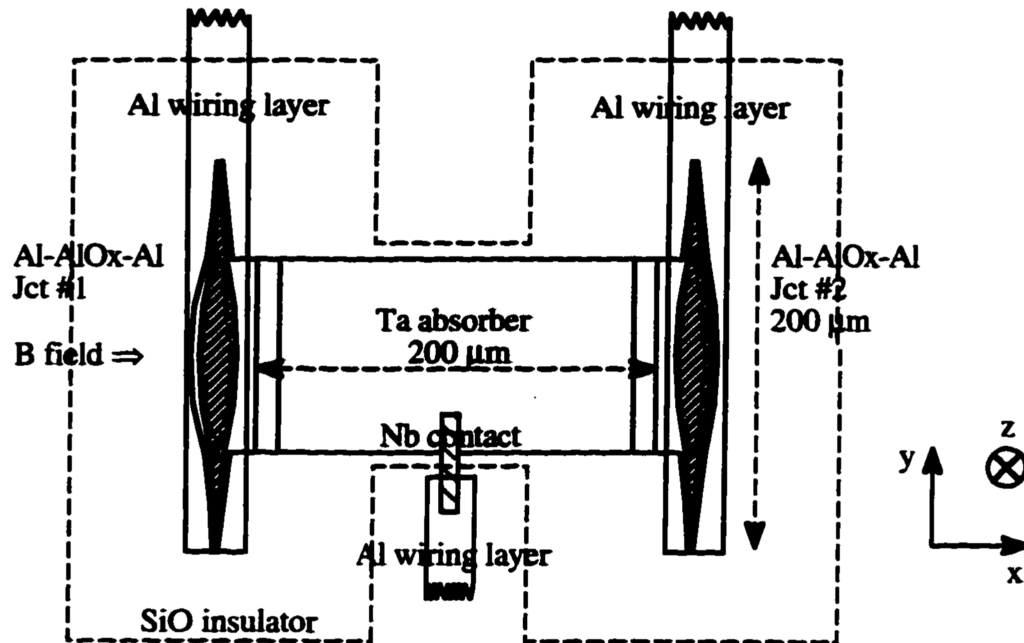

Figure 2.3.1.: Device geometry: The device provides imaging in x-direction. The z-direction is perpendicular to the plane of the device.

Figure 2.3.1. shows a picture of the device geometry. The absorber dimensions of 200 μm x 100 μm reflect a compromise between a desirably large area of at least 1 mm^2 and the concern that some unexpected effect might reduce the quasiparticle lifetime below the time it takes the charges to diffuse to the trap region. At the time of the device design, the lifetimes had never been measured in tantalum. In niobium, the lifetimes were found to be much lower than predicted from theory.

The niobium contact is small to reduce the number of absorption events in it. The large niobium gap prevents quasiparticles from diffusing out of the absorber *and* quasiparticles from absorption events in the Al leads from entering the absorber.

The aluminum traps overlap the tantalum absorber by 10 μm so that the large area of overlap ensures good quasiparticle transmission in case parts of the absorber surface are dirty or oxidized. In the overlap region, the aluminum gap is increased above its bulk value due to the proximity effect [de Gennes, 1964]. Depending on the exact gap profile and the location and of the scattering event that traps the quasiparticle, the emitted phonon can have an energy above $2\Delta_{Al}$ and add fluctuations to the number of quasiparticles by breaking pairs in the aluminum. This concern did not outweigh the advantages aluminum has to offer as a junction material for the design of the device.

When designing the device there was a lot of concern about trapping flux in it. That creates regions of reduced gap and limits the quasiparticle lifetime. The performance of the best devices at that time was affected by trapped flux [Kraus, 1989b]. It was caused by the magnetic field used to suppress the dc Josephson current, which had a small component perpendicular to the detector. One can affect the required magnetic field using non-standard junction geometries, because the total critical current is an integral of the current density over both dimensions of the junction area [Broom, 1980]. For minimum required field, the junction shape in our detectors follows an approximation to a fourth order polynomial [Peterson, 1991]. For the same reason the junction is stretched out in the direction perpendicular to the magnetic field. The junction is symmetric about the center of the absorber and its shape s(y) (with y in units of the junction length L_{jct}) can be parametrized as

$$s(y) = \pm 9(1 - 4y^2 + 4y^3 - y^4). \qquad 2.3.1.$$

Figure 2.3.2. shows by how much the critical current at a given magnetic field is suppressed compared to the value expected for a rectangular junction of the same cross sectional area in direction perpendicular to the magnetic field. The suppression is effective, although not quite as effective as predicted because of small deviations from the ideal shape

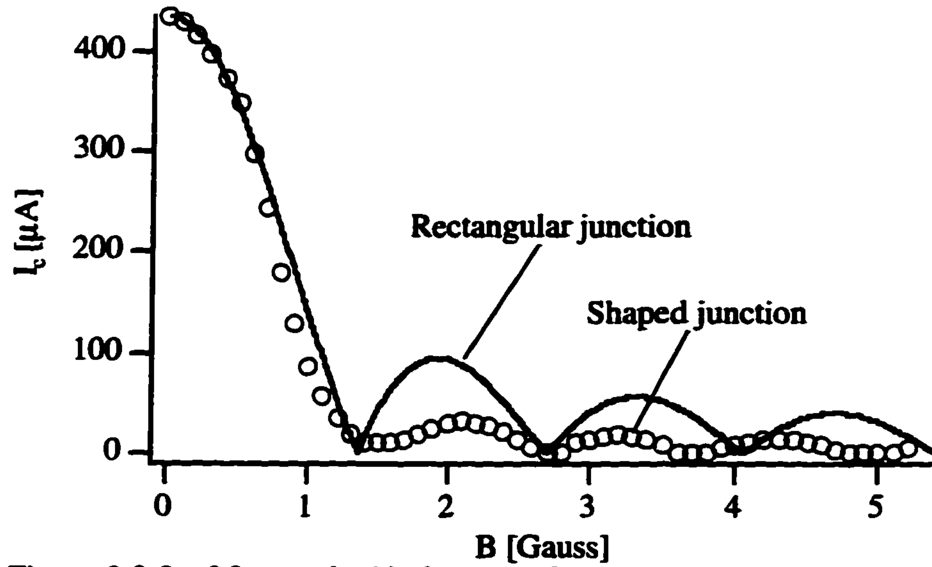

Figure 2.3.2.: Measured critical current for a shaped junction with R_{NN} = 0.6Ω compared to the |sin(x)/x| pattern expected for a rectangular junction

introduced in the fabrication process and by the finite width of the junction at the edges. Also, shaped junctions exhibit wider minima of $I_C(B)$ compared to rectangular junctions, facilitating suppressing the critical current in both junctions simultaneously.

Choosing the junction length to L_{jct} = 200 μm turned out to be somewhat problematic, because it also lowered the voltage for the first Fiske mode to 110 μV. Fiske modes are resonances that occur whenever the ac Josephson effect excites signals at a frequency of the eigenmodes of the cavity formed between the two junction electrodes [Fiske, 1964]. They manifest themselves as peaks in the junction's I(V) characteristics. They increase the subgap current and cause excess noise when biasing in their vicinity (cf. figure 3.1.1.). In rectangular junctions, Fiske mode resonances occur at equidistant voltages [Eck, 1964]

$$V_n = n\frac{\hbar\pi\bar{c}}{2eL_{jct}} \quad \text{with} \quad \bar{c} = c\sqrt{\frac{d_{oxide}}{\varepsilon(2\lambda_{Al} + d_{oxide})}}. \qquad 2.3.2.$$

Here L_{jct} is the junction dimension in direction perpendicular to the magnetic field and the effective speed of light $\bar{c}$ inside the junction is reduced by more than factor of 10 compared to its free space value [Swihart, 1961]. In shaped junctions, the peak voltages are no longer evenly spaced, but the voltage for the lowest resonance can still be estimated from the above formula for $n = 1$. In our devices, a resonance voltage of 110 μV corresponds to an oxide thickness $d_{oxide} = 18$Å. That is a reasonable value for tunneling diodes.

The wiring layer is made out of aluminum designed to ensure fast diffusion of quasiparticles away from the trap to prevent an increase in noise due to backtunneling. A silicon monoxide insulator separates the wiring layer from the trap and the absorber to avoid shorting the junction.

Fabrication

Tantalum films 6000 Å thick are deposited by dc magnetron sputtering at a rate of 40 Å/s with the substrate held at a temperature of 700 °C. This yields bcc tantalum films with a transition temperature above 4.2 K, a resistivity of 14.5±1.5 μΩcm, somewhat above the bulk value of 12.3±0.2 μΩcm, and a residual resistance ratio $R_{300K}/R_{10K} = 30$. The absorber pattern is defined by wet etch in a 3:1 solution of $FeCl_3/HCl$ and HF that ensures sloped edges for good edge coverage even if the aluminum trap is significantly thinner than the absorber.

One should keep in mind that despite the short x-ray absorption length in Ta, even a 6000 Å film will only absorb about 25% of all incoming photons at 6 keV, where the iron emission lines are. This is sufficient for test devices, but for practical usage a higher absorption efficiency would be desirable. That would require either 2 μm thick films or the use of a tantalum crystal as absorber [Netel, 1996]. Of course, for lower energy x-rays the absorption efficiency is much higher.

The aluminum trap is thermally evaporated at 200 Å/s for a thickness of 1500 Å. The films have a normal state resistance of 2.9±0.3 μΩcm and a residual resistance ratio of 13. They are thermally oxidized at room temperature for 3 hours in 600 mTorr of oxygen.

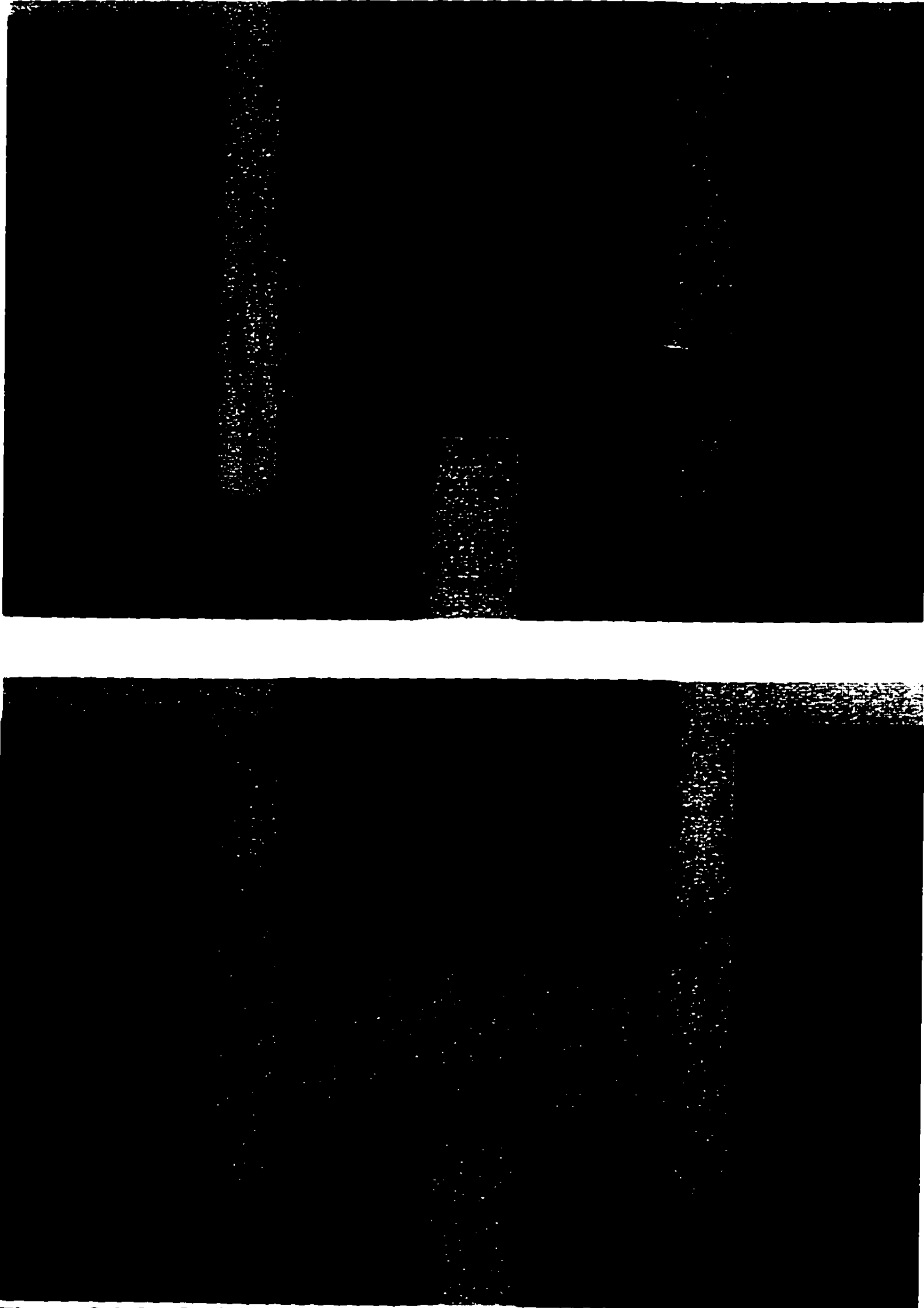

Figure 2.3.3.: Optical photograph of typical devices:
1) 10 μm overlap between aluminum trap and tantalum absorber
2) aluminum trap overlaps entire tantalum absorber

The counterelectrode is thermally evaporated at a much lower rate of 15 Å/s to prevent the impinging atoms from damaging the barrier. This process yields tunnel junctions with a normal state resistance of $R_{NN} \approx 0.5\ \Omega$ corresponding to a current density of 30 A/cm^2. In zero magnetic field, they exhibit the full zero voltage current of 500 μA according to $I_c R_{NN} = \pi/4 \cdot (2\Delta_{Al}/e)$ and their low voltage subgap current decreases with decreasing temperature down to our dewar's base temperature of 0.235K.

We have investigated two types of devices, located on the same chip. In the first device, the aluminum traps overlap the Ta absorber by only 10 μm. In the second device, shown in figure 2.3.4., the aluminum trap overlaps the entire tantalum absorber. X-ray photons will be absorbed almost exclusively in the tantalum film because of its high atomic number. However, the quasiparticles will immediately scatter into the lower gap aluminum film and will diffuse in it toward the junctions. There will still be a certain degree of trapping between the proximity enhanced aluminum film on top of the absorber and bulk aluminum of the junction, but it will be comparably weak because the quasiparticles are injected into the junction area at a lower energy where the inelastic scattering time is longer. This device was initially designed to avoid quasiparticle propagation in tantalum, whose properties in regard to quasiparticle diffusion and lifetime had never been experimentally investigated. It also allows us to study non-equilibrium quasiparticle dynamics in aluminum films.

2.4. Cryogenics

The use of aluminum detector junctions requires operating temperatures below 0.4K for long quasiparticle lifetimes. Furthermore, low temperatures decrease the junction's thermal dark current and increase its dynamic resistance, thereby lowering the electronic noise. For our junctions with a normal state resistance $R_{NN} \approx 0.5\ \Omega$ operating

temperatures not above 0.25 K were desirable to increase the dynamic resistance above 10 kΩ such that the amplifier's voltage noise did not dominate the resolution.

All experiments were performed in a two stage ^{3}He cryostat fabricated by Infrared Systems [Pernic, 1995]. Its cold stage attains a base temperature of 0.235 K by lowering the vapor pressure above the liquid ^{3}He with a charcoal absorption pump. The purpose of the second ^{3}He stage is to cool the pumping line of the cold stage to 0.3K and thereby reduce the heat load into the cold stage. Figure 2.4.1. shows a cross section of the two ^{3}He stages (usually referred to as the 0.3K and the 0.2K stage) and their suspension inside a toroidal ^{4}He tank. For successful condensation of ^{3}He good heat sinking of the condensing blocks and a small heat leak into the 0.3K stage from the higher temperature portions of the dewar are essential. This required the use of Bellville® washers and Apiezon N® thermal grease to ensure good thermal contact between the condensing blocks and the aluminum cylinder and between the copper braids and the ^{4}He tank even at low temperatures. We have also reduced the heat load into the 0.3K stage by encasing the charcoal pumps in a solid aluminum shield bolted to the ^{4}He stage.

We have estimated the heat flow in this cryostat to characterize its performance and to estimate base temperature and power levels required for experiments at elevated temperatures. The base temperature of a dewar is determined through the condition that the cooling power $P_{cooling}$ be equal to the total heat leak P_{in} into the cold stage, such that

$$P = P_{in} - P_{cooling} = C_V \frac{\partial T}{\partial t} = 0. \qquad 2.4.1.$$

The main contributions to the heat leak P_{in} into the 0.2K stage held at $T_{0.2K}$ are due to heat flow through the pumping lines and the wiring connections and radiation from the ^{4}He stage. Heat transfer through residual gases is neglected, since they are frozen out at cryogenic temperatures. The pumping line between the 0.2 K stage and the 0.3 K stage (1"

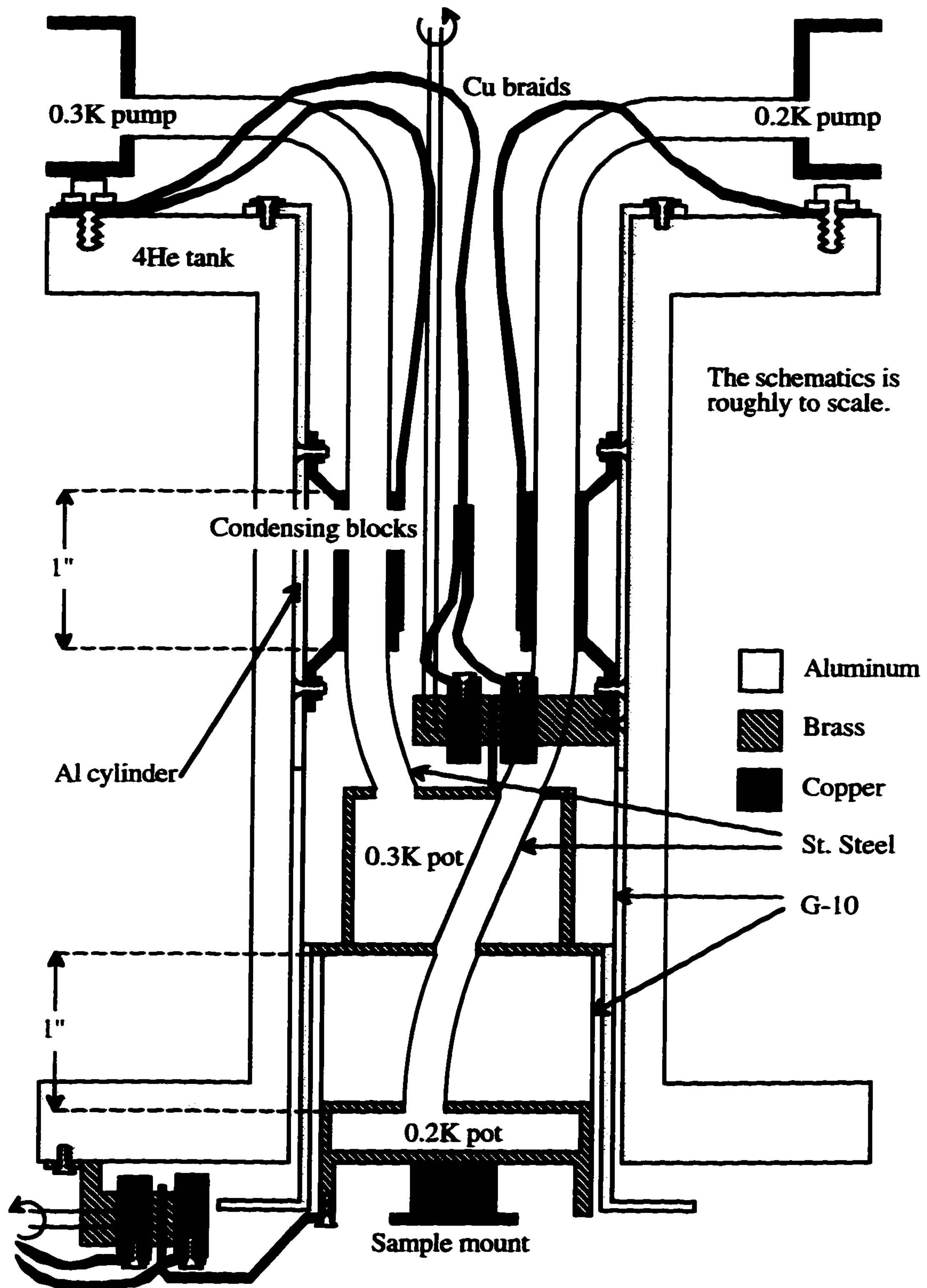

Figure 2.4.1.: Cross section of the ^{3}He stages in our cryostat. Thin-walled G-10 cylinders center the two cold stages inside the Al cylinder

length 1/4" diameter 321 stainless steel flex tubing with 0.006" wall thickness) has a thermal conductivity of 0.15 T [W/Km] [Lounaasma, 1974] and causes a heat load of 8.8μW ($T_{0.3K}^2$-$T_{0.2K}^2$). There are also 16 superconducting NbTi wires to the cold stage (0.005" diameter, 4" length) with a constant thermal conductivity of 0.2 [W/Km] [Dubeck, 1968]. They are heat sunk at the 0.3K stage and add a heat load of 0.4 μW($T_{0.3K}$ - $T_{0.2K}$). For a cold stage surface area of 116 cm^2 and the ^{4}He stage held at 1.5 K, radiation adds constant 3.3 nW to the parasitic heat.

The cooling power $P_{cooling}$ depends on how fast heat can be extracted from the ^{3}He liquid by evaporative cooling. It is given by the product of latent heat of the liquid-gas transition of ^{3}He, gas density and pumping speed. The cooling power decreases rapidly with temperature, because the ^{3}He vapor pressure which determines the gas density follows a roughly exponential temperature dependence. Values for the latent heat can be found in the literature [Roberts, 1964]. The ideal gas equation gives an appropriate approximation to the gas density [Keller, 1955]. The geometry of the pumping line sets an upper limit of 0.1 l/s to the pumping speed at 1 K [White, 1989]. However, diffusion and absorption processes inside the charcoal pump usually limit the pumping speed to much lower value [Pernic, 1995].

With the above expressions determining the heat flow, it is most convenient to solve equation 2.4.1. graphically. Figure 2.4.2. shows the both the heat leak into the cold stage and cooling power as a function of $T_{0.2K}$ for constant $T_{0.3K}$ = 0.3K. The base temperature corresponds to the temperature where both curves intersect. Under the assumption that the pumping speed and thus the cooling power is limited by the dimensions of the pump line (dashed line), the predicted base temperature is well below the observed value of 0.235K. For an experimental estimate of the cooling power we have added 10 μW to the heat load, much more than all other sources of heat, through a 100 kΩ resistor. The increase in base temperature to 0.298 K shows that the above discrepancy is in fact due to an overestimate of the cooling power (rather than an underestimate of the heat leak). The

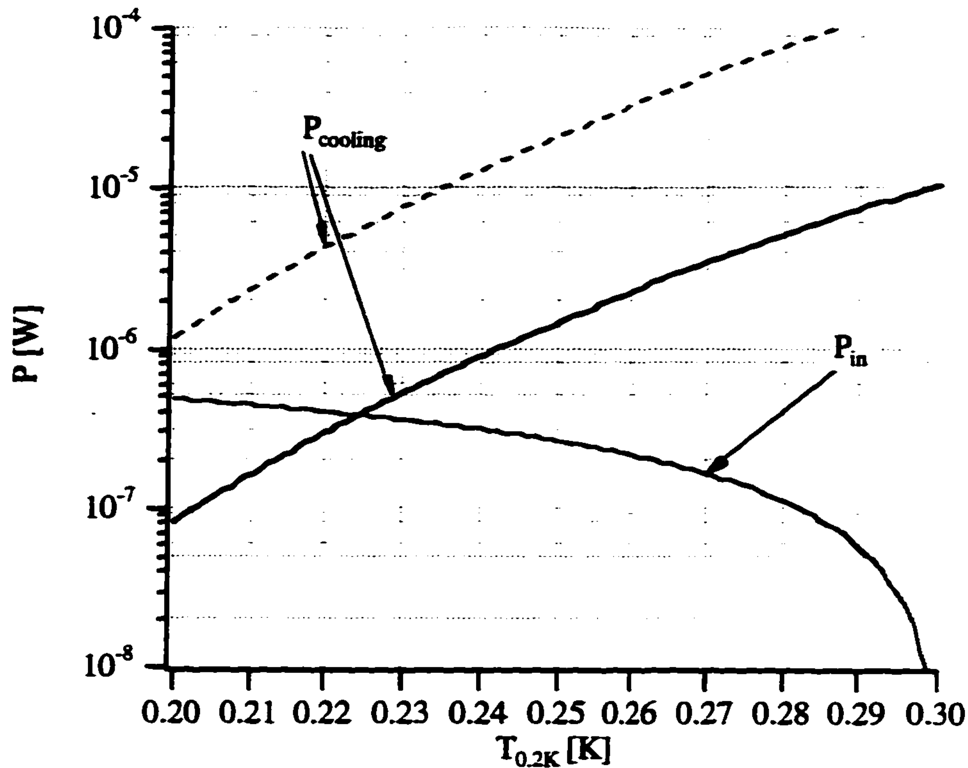

Figure 2.4.2.: Heat flow in our cryostat as a function of cold stage temperature. The dashed line is the predicted cooling power if the pumping speed were limited by the dimensions of the pumping line. It is adjusted (solid line) to match the experimental value of 10 μW at 0.298K. At the base temperature, the cooling power matches the input power P_{in}.

cooling power was then reduced by a constant factor to match the input power of 10 μW at 0.298 K (solid line). There remains a small discrepancy between the new predicted base temperature of 0.225 K and the observed value of 0.235 K. However, the power level of 0.5 μW required to explain this discrepancy is well within the experimental uncertainties in the estimate of the dominant heat leak of the pumping line.

The cold stage temperature is inferred from a Lakeshore germanium resistance thermometer (model GR-200A-50). The resistance is read out with a Keithley 195A digital multimeter at a dc sensor current of 200 nA to avoid self-heating. Despite averaging over ten measurements, the internal resolution of the multimeter limits the temperature resolution

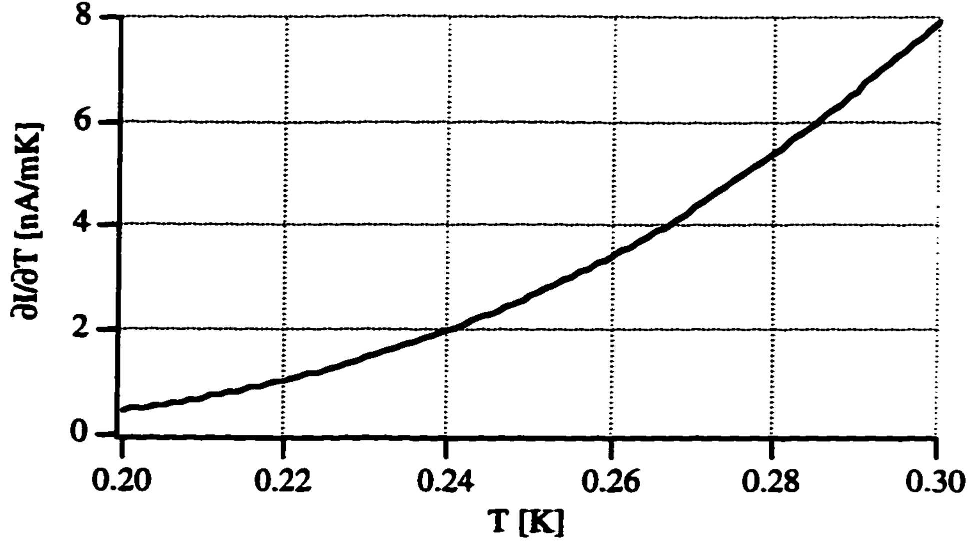

Figure 2.4.3: Temperature variations of the subgap current for a 0.5 Ω junction and a bias voltage of 70 μV.

to ±0.5 mK. We therefore use the fluctuations of the quasiparticle contribution to the subgap current

$$I(V,T) = \frac{2(V+\Delta/e)}{R_{NN}} e^{-\Delta/kT} \sqrt{\frac{2\Delta}{eV+2\Delta}} \sinh\left(\frac{eV}{2k_BT}\right) K_0\left(\frac{eV}{2k_BT}\right) \qquad 2.4.2.$$

as a measure of temperature stability [van Duzer, 1981]. Since we use a dc voltage bias (see chapter 3), we can infer the temperature stability of our setup directly by differentiating equation 2.4.3. For voltages around 70 μV, ∂I/∂T is not a strong function of bias.We do not use any temperature stabilization in our dewar. We measure a drift in the subgap current of order 0.2 nA at the base temperature of our dewar over a time scale of a typical half hour run. This corresponds to a temperature stability of 0.1 mK

2.5. Data Acquisition

The device is cooled to the desired operating temperature, typically around 0.24 K, and irradiated uniformly with a 100 μCi radioactive ^{55}Fe source. The source material decays into manganese by electron-capture and emits x-rays, 88% of which are Mn K_α photons with an energy of 5.89 keV and 12% of which are Mn K_β photons with an energy of 6.49 keV. The source is mounted on a rotating arm and can be turned away to confirm that all events are in fact x-ray induced. It is located at a distance of about 1" from the detector resulting in a count rate of about 1 event per second in the Ta absorber.

The x-ray induced signals are amplified with a current sensitive preamplifier that will be described in detail in chapter 3. The preamplifier bandwidth is sufficient to ensure that pulse height and rise time even for the fastest pulses are not distorted by more than 5%. The unfiltered current waveforms are captured with an HP54510A digital oscilloscope. This oscilloscope features an 8-bit A/D converter with a sampling frequency of 1 GHz. However, if data are taken at a lower sampling rate, the oscilloscope in the raw data mode performs a moving average and reports data with 10 bit precision. The entire set of current waveforms -typically we capture between 500 and 2000 events- is then saved on disk using LabVIEW programs and a Macintosh IIci. This procedure allows us to extract physical information from the unfiltered current pulses and later integrate them numerically and apply digital filters for best device resolution.

To measure the electronic noise we inject current pulses from an HP33120A arbitrary waveform generator through a 1 MΩ resistor into the amplifier input with the junction connected. We can download model pulses from our simulation (see chapter 2.7.) into the waveform generator to have as close a match between the pulse shape of the injected and the x-ray induced pulses as possible. This also allows us to estimate the distortion the amplifier introduces to the detected waveforms. However, there remains a certain difference between injected and x-ray induced pulses. X-rays temporarily change

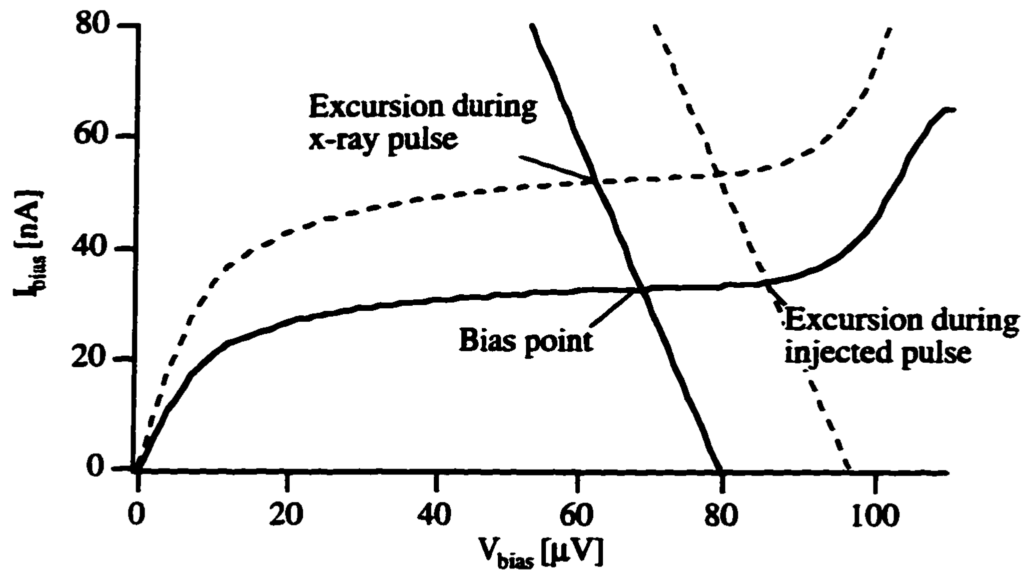

Figure 2.5.1.: The change in bias during an x-ray pulse occurs along the load line (straight solid line); during an injected pulse it occurs along the dc I(V) characteristics. The slope of the load line drawn is exaggerated (400 Ω) for illustration.

the I(V) characteristic in the device causing an excursion of the bias point along the fixed load line of the circuit. Injected pulses effectively change the load line temporarily such that the excursion occurs along the fixed I(V) characteristic (figure 2.5.1.). Different dynamic resistances affect the amplifier response, because the finite open loop gain of the amplifier introduces a low frequency correction factor $1/(1+R_F/A_{OL}R_{dyn})$ to the amplifier gain. This difference is not expected to be large as the amplifier used in our experiments has an input resistance R_F/A_{OL} of only 200 Ω even at maximum signal frequencies of 300 kHz, still much lower than the device resistance during a pulse.

We can Fourier transform the baseline noise of the dark current measured with the oscilloscope using standard LabVIEW routines. This allows us to measure the spectral noise density immediately after taking x-ray data without changing the setup. We have taken great care to eliminate pickup and interference from external sources. All events we measure are x-ray induced. The electronics, including the magnet power supply, is battery operated and enclosed in a single shield, which includes the dewar and whose only ground

connection is at the oscilloscope through the outer braids of the coax cables carrying the pulse outputs. The responses of the two detector junctions is taken out of different ports from the dewar, with the two amplifier boards enclosed in separate cases to effectively eliminate crosstalk between the channels.

2.6. Time Scales

The performance of imaging tunnel junction detectors depends on the dynamical processes inside the detector. We will address the individual processes briefly and discuss their expected relative time scales as set by the device geometry and the materials choices. All of these processes will be discussed in more detail in chapter 4 with experimental data to quantify them. It turns out that many of the time scales are comparable and of order microseconds.

Diffusion

A rough estimate of the average time a quasiparticle spends in the absorber in a trapping geometry is given by $\tau_{diff}=(L/2)^2/D$, where L is the absorber length and D the quasiparticle diffusion constant in the absorbing film (figure 2.6.1.). Trapping acts like a quasiparticle sink that accelerates the flow of charge out of the absorber. We had initially expected diffusion constants of 500 cm^2/s for our Ta films. Experiments showed a diffusion constant almost two orders of magnitude lower.

Diffusion out of the counterelectrode can be estimated similarly. Since there is no trapping involved, it will take significantly longer for quasiparticles to diffuse out of the counterelectrode volume.

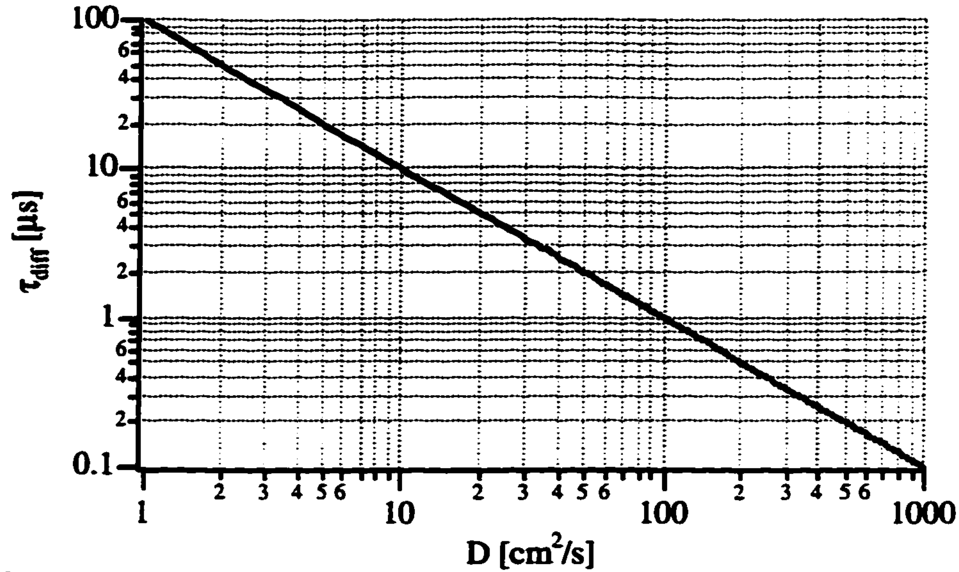

Figure 2.6.1.: Approximate time scales for quasiparticle diffusion over length scales of order 200 µm

Trapping

Inelastic scattering with phonon emission causes the quasiparticles to be trapped. The expression for the scattering rate can be derived from Fermi's Golden Rule. For an electron with energy E in the limit of zero temperature it is given by [Kaplan, 1976]

$$\tau_s^{-1} = \tau_0^{-1}(k_B T_C)^{-3} \cdot \int_0^{E-\Delta} d\Omega\,\Omega^2 n(E-\Omega)\left(1-\frac{\Delta^2}{E(E-\Omega)}\right) \qquad 2.6.1.$$

Here τ_0 is a material dependent characteristic time scale that depends on the strength of the electron-phonon coupling and Ω is the energy of the phonon being emitted. The factor of Ω^2 arises from the phonon density of states, $n(E-\Omega)$ is the density of final electron states and the integral is taken over all possible phonon states. The factor in parentheses is a coherence factor that describes the nature of the electron-electron interaction in the superconducting state. The integral can be solved analytically [Kaplan, 1976] and has a functional form

$$\frac{1}{\tau_s} = \frac{1}{\tau_0}\left(\frac{\Delta}{k_B T_C}\right)^3 \cdot$$

$$\left\{\frac{1}{3}\left(\left(\frac{E}{\Delta}\right)^{1/2} - 1\right)^{3/2} + \frac{5}{2}\left(\left(\frac{E}{\Delta}\right)^2 - 1\right)^{1/2} - \frac{\Delta}{2E}\left(1 + 4\left(\frac{E}{\Delta}\right)^2\right)\ln\left[\frac{E}{\Delta} + \left(\left(\frac{E}{\Delta}\right)^2 - 1\right)^{1/2}\right]\right\} \cdot$$

2.6.2.

This is plotted in figure 2.6.2 for aluminum. For energies well above the gap energy, the scattering rate varies as $(E/\Delta)^3$ because of the total number of phonon states available. For energies near the gap edge, the phase space for phonon emission and the coherence factor decrease and scattering slows down. Scattering occurs preferentially into states close to the gap where the electron density of states diverges.

For quasiparticle injection into the trap at energy Δ_{Ta} (figure 2.6.2.) inelastic scattering in aluminum is expected to be fast (≈10 ns) compared to all other time scales that affect the detector response. It will be slower for quasiparticle injection into aluminum whose gap is increased by the proximity effect. The exact value depends on the particular increase in a given device.

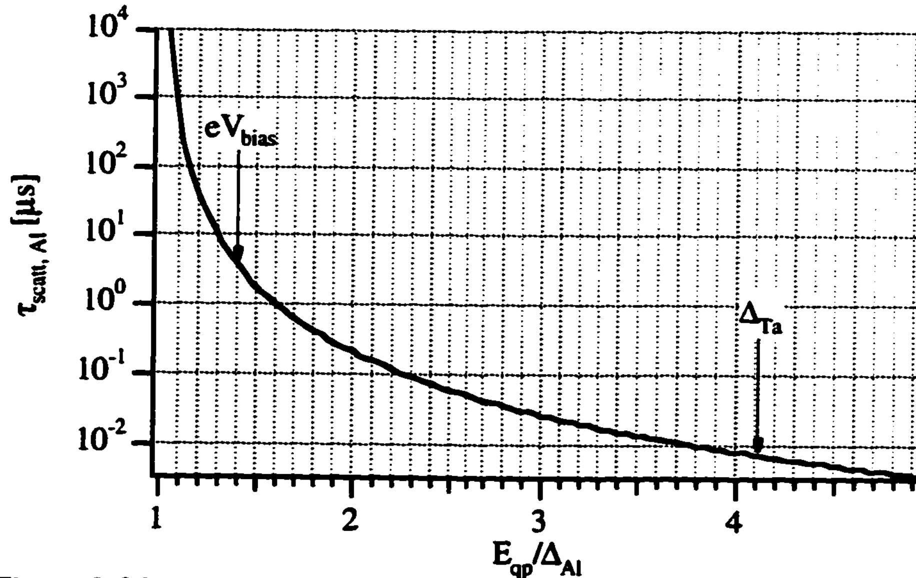

Figure 2.6.2.: Inelastic scattering times in aluminum. Quasiparticles injected into the trap at energy Δ_{Ta} scatter much faster than those injected into the counterelectrode at or slightly above eV_{bias} [Kaplan, 1976].

Inelastic scattering also determines the quasiparticle energy distribution in the junction electrodes. The energy distribution around eV_{bias} determines which tunneling processes can occur and at what rate, as discussed in the next section. At that energy, scattering times are of order microseconds, comparable to characteristic tunneling times and -as it turns out- comparable to time scales for outdiffusion.

Tunneling

The expression for the tunneling current across a barrier can be derived from Fermi's Golden rule. Consider a junction where the energy levels E_l of the left electrode are raised relative to the right electrode E_r by a bias eV. The net current is given by:

$$I = 2e\frac{2\pi}{\hbar}\int_0^\infty dE_l n_l(E_l)\int_0^\infty dE_r n_r(E_r)[f(E_l)-f(E_r)]|T|^2_{lr}\,\delta(E_l+eV-E_r). \qquad 2.6.3.$$

Here f(E) is the Fermi distribution function, n_l and n_r are the densities of states in the two electrodes, T_{lr} is the tunneling matrix element and the delta function ensures energy conservation. For low bias voltages, the tunneling matrix element is constant [Bardeen, 1961] and the densities of states are equal to their value at the Fermi surface. At low temperatures, the Fermi functions can be approximated by stepfunctions. For both metals in the normal state, the tunneling current then varies linearly in voltage with a magnitude

$$I = 2e\frac{2\pi}{\hbar}n(E_F)^2|T_{lr}|^2 eV \equiv \frac{V}{R_{NN}} \qquad 2.6.4.$$

One can now define a tunnel time through the relation $I = eN/\tau_{tun}$, where $N = n(E_F)\cdot eV\cdot dA$ is the total number of quasiparticles that can tunnel. This way, τ_{tun} can be expressed in terms of the measurable quantities R_{NN} and the electrode volume dA. If both electrodes are

in the superconducting state, the only modification arises from the change in the density of states. The tunnel time can thus be expressed as [deKorte, 1992]

$$\tau_{tun} = 2e^2 n(E_F) dAR_{NN} \frac{\sqrt{(\Delta + eV_{bias})^2 - \Delta^2}}{\Delta + eV_{bias}} \qquad 2.6.5.$$

The factor of 2 enters because only quasiparticles from the electron-like branch of the dispersion curve can tunnel. The tunneling time decreases at lower bias voltage with increasing density of states in the opposing electrode. Figure 2.6.3. shows typical values for our junctions with $R_{NN} = 0.5\ \Omega$ and $(Ad)_{trap} = 700\ \mu m^3$ and $(Ad)_{CE} \approx 2800\ \mu m^3$. Tunneling from the counterelectrode is slower by a factor $(Ad)_{CE}/(Ad)_{trap} \approx 4$.

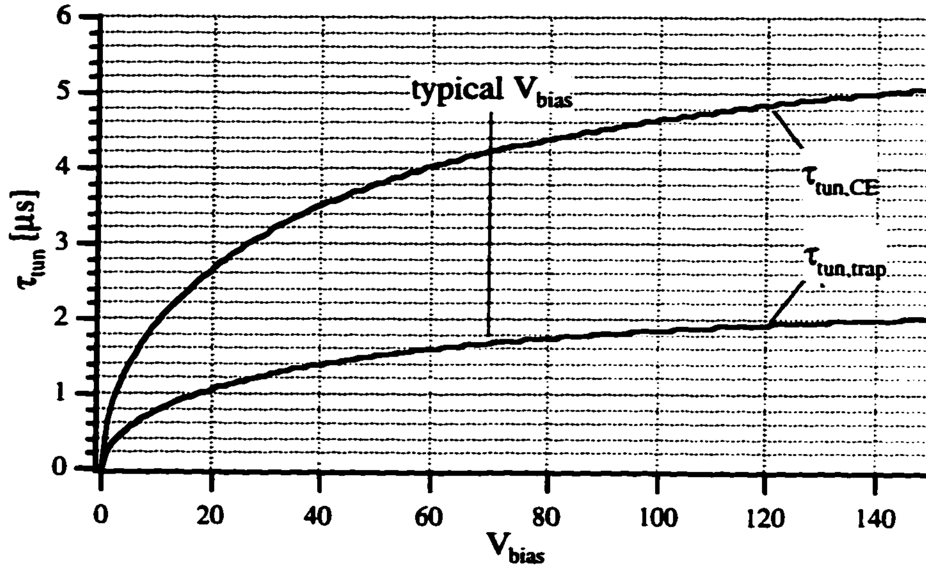

Figure 2.6.3.: Times for tunneling from the trap ($\tau_{tun,trap}$) and from the counterelectrode ($\tau_{tun,CE}$) in our devices

Recombination

Quasiparticle lifetimes must be long on the time scales of all other processes. An upper limit is set by its thermal equilibrium value, as shown in figure 2.6.4. in the case of aluminum according to [Kaplan, 1976]

$$\frac{1}{\tau_{rec}} = \frac{1}{\tau_0}\pi^{1/2}\left(\frac{2\Delta}{k_B T_C}\right)^{5/2}\left(\frac{T}{T_C}\right)^{1/2} e^{-\Delta/k_B T}. \qquad 2.6.6.$$

Here τ_0 is a material dependent characteristic time constant that scales with the strength of electron-phonon coupling. The probability of recombination decreases exponentially with temperature, because the density of thermal quasiparticles $n_{th} = n(E_F)\ \sqrt{(2\pi\Delta k_B T)}\ e^{-\Delta/kT}$, which are excited above the gap and available to recombine, follows an exponential temperature dependence. Lifetime measurements in aluminum agree closely with theory [Gray, 1971].

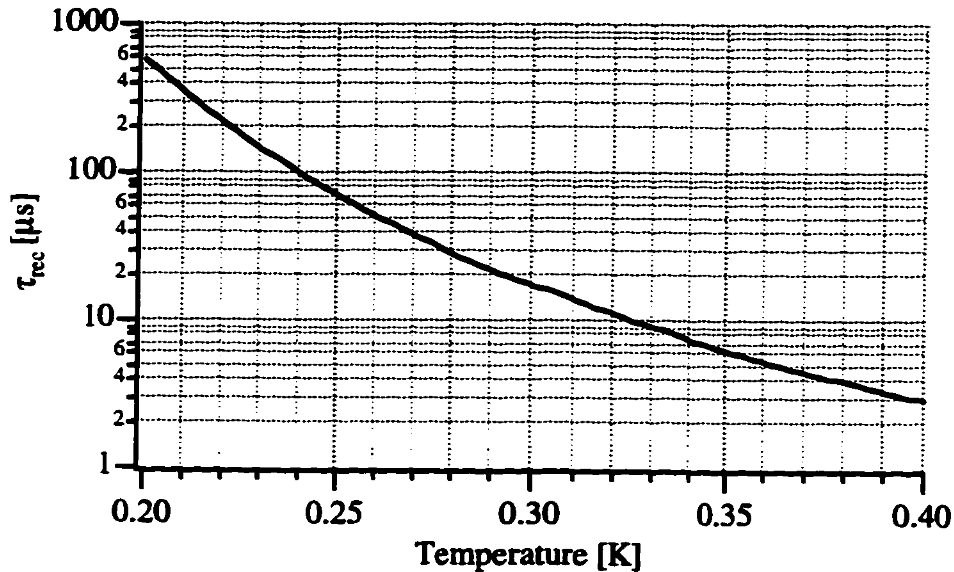

Figure 2.6.4.: Low temperature thermal quasiparticle lifetime in aluminum [Kaplan, 1976]

When the number of excess quasiparticles N_x produced by x-ray absorption exceeds the thermal background, recombination among those excess quasiparticles adds another loss mechanism. One can estimate the strength of this so-called self-recombination by defining a recombination rate per unit density R. Since there are N^2 ways to form a pair

from N quasiparticles, the total rate at which quasiparticles recombine is given by [deKorte. 1992]

$$\frac{N(t)}{\tau_{rec,self}} = \frac{R}{V} \cdot (N_x(t) + Vn_{th})^2 \qquad 2.6.7.$$

The strength of this so called self-recombination depends on the square of the excess quasiparticle density as they spread out diffusively and manifests itself in a non-linear response in the charge output vs. x-ray energy. The numerical value for R can be obtained from the thermal equilibrium relation $1/\tau_{rec}=Rn_{th}$ as

$$R = \left(\frac{2\Delta}{k_B T_c}\right)^3 \frac{1}{2n(E_F)\Delta\tau_0}. \qquad 2.6.8.$$

R has the value of 11.1 $\mu m^3/s$ in aluminum and 300 $\mu m^3/s$ in tantalum. For 6 keV x-rays, at the time the currents peak there are at most 3 million quasiparticles in the trap volume of 700 μm^3. This would correspond to self-recombination times of tens of microseconds if the quasiparticle density remained this high throughout the pulse. However, since the quasiparticle density and consequently self-recombination decreases on a microsecond time scale set by the tunneling time, self-recombination is not expected to affect the performance of our devices.

In many circumstances the low temperature quasiparticle lifetime is reduced significantly below the value predicted by thermal and self-recombination. The most common cause are areas of reduced energy gap that serve as trapping sites inside the absorber. They can arise from magnetic flux trapped inside the film that drives certain areas into the normal state with zero energy gap [Kraus, 1989b]. They can also arise from damage to the film, particularly at the edges, introduced in the fabrication process. They also occur at grain boundaries and in areas of high impurity concentration [Verhoeve,

1996]. Observed quasiparticle lifetimes are sometimes as low as a few microseconds, even at temperatures below 100 mK [Kraus, 1989b; Mears, 1996].

Phonon Trapping

When two quasiparticles recombine, they emit a phonon with energy 2Δ. Unless these phonons escape into the substrate or decay anharmonically, they can be reabsorbed by the Cooper pair condensate thereby re-creating two quasiparticles. This effect is called phonon trapping. It can lead to a significant enhancement of the quasiparticle lifetime, if the characteristic time scales for pair-breaking τ_{pb} is short compared to typical phonon escape times τ_{esc}. In terms of these time scales, the enhancement of the intrinsic quasiparticle lifetime τ_{rec} is given by the phonon trapping factor [Rothwarf, 1967]

$$\frac{\tau_{rec,eff}}{\tau_{rec}} = 1 + \frac{\tau_{esc}}{\tau_{pb}}. \qquad 2.6.9.$$

The pair breaking time in our devices is 23 ps in tantalum and 240 ps in aluminum [Kaplan, 1976]. The escape time into the substrate can be estimated from the phonon velocity c_{ph}, the film thickness d and the phonon transmission coefficient into the substrate α according to $\tau_{esc} = 4d/\alpha c_{ph}$ [Gray, 1971]. The transmission coefficients into the oxidized silicon substrate depend on the acoustic mismatch and are $\alpha_{Ta\text{-}SiO2} = 0.25$ for phonons from a tantalum film and $\alpha_{Al\text{-}SiO2} = 0.7$ for aluminum films [Kaplan, 1979]. The phonon trapping factor in tantalum ($c_{ph,Ta} = 2.5 \cdot 10^5$ cm/s) then has a value of about 170, and in aluminum ($c_{ph,Al} = 4 \cdot 10^5$ cm/s) we expect only an enhancement by a factor 1.9. Phonon trapping enhances the quasiparticle lifetime much more strongly in tantalum, where the stronger electron-phonon coupling leads to faster pair-breaking. In fact, the phonon trapping factor in aluminum is an upper limit, because the above equation is strictly valid only in the limit where the film thickness exceeds the mean free path $c_{ph}\tau_{pb}$ against pair breaking.

Anharmonic decay, which could provide an alternative mechanism for phonon loss, is slow compared to phonon escape and only provides a small correction to the escape time [Gaitskell, 1993]. Some uncertainty in the estimate of the phonon trapping factor arises from the fact that phonons created by recombination in regions of reduced gap will not have enough energy to break a pair once they have traveled to a region where the gap assumes its bulk value. This might reduce the phonon trapping factor in tantalum. It will not substantially affect the quasiparticle lifetime in aluminum where phonon trapping effects are weak.

2.7. Current Pulse Simulations

The difficulty in interpreting the observed current pulse shapes arises from the fact that the time scales of the various processes are comparable and separating the contributions of the individual effects is challenging. To aid our understanding we have written computer simulations based on the processes outlined above that determine the quasiparticle dynamics. These simulations have evolved over time as the experiments either turned out to justify the underlying assumptions or made the inclusion of new effects necessary. They are likely to change in the future as our understanding of the devices improves. All simulations were written by Ken Segall in Turbopascal and will be briefly summarized here.

Current pulses

At any moment, the x-ray induced current pulse is given by the net charge transferred across the tunneling barrier. There are four processes that contribute to the total current (Figure 2.7.1). All quasiparticles in the trap can directly tunnel into the counterelectrode, and all quasiparticles in the counterelectrode can backtunnel via the Gray

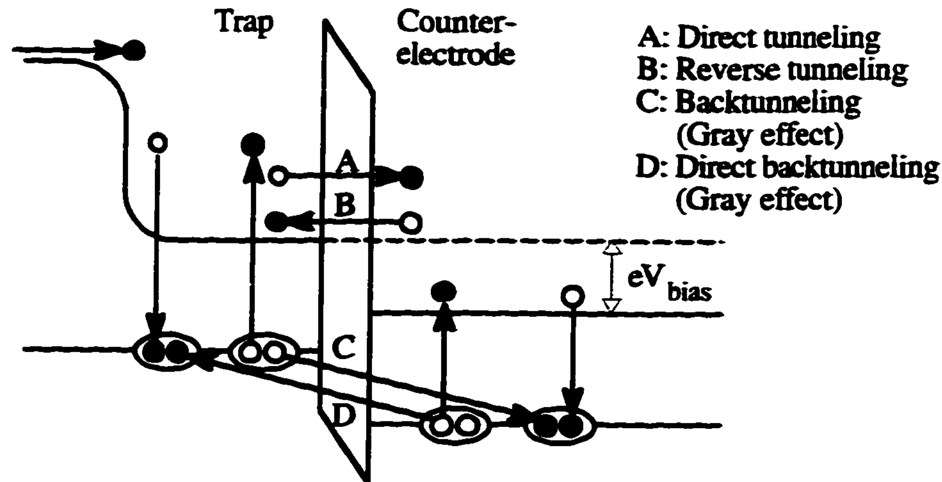

Figure 2.7.1.: Tunneling processes

effect by breaking a pair in the trap. Only for quasiparticles above eV_{bias}, the inverse processes are also possible. Quasiparticles can reverse tunnel from the counterelectrode into the trap and high energy quasiparticle in the trap can "directly backtunnel" into the counterelectrode. Both direct tunneling and backtunneling contribute to the charge flow in forward direction, while reverse tunneling and direct backtunneling cause a current in the opposite direction. The net current therefore depends on the number of quasiparticles N_{trap} in the trap and N_{CE} in the counterelectrode *and* their energy distribution. Tunneling times depend on the thickness of the electrode from which the quasiparticles tunnel, and are different for trap and counterelectrode. They also depend on the density of states at the final quasiparticle energy, which increases towards the gap edge. That makes the tunneling time energy dependent and, for quasiparticles at a given energy, different for direct and backtunneling.

Simulation inside Absorber

For numerical simulation of the charge density profile in the absorber we use the Crank-Nicholson formalism [e.g. Press, 1989]. It represents the diffusion equation as a

difference equation in such a fashion that the iterations are both stable for arbitrary time steps Δt and second order accurate in both time and space. That combines the advantages of large time steps for short computation time and minimal rounding error. For a particle density $n(x_i, t^j) \equiv n_i^j$ the difference equation is given by

$$\frac{n_i^{j+1} - n_i^j}{\Delta t} = \frac{D}{2}\left(\frac{\left(n_{i+1}^{j+1} - n_i^{j+1} + n_{i-1}^{j+1}\right) + \left(n_{i+1}^j - n_i^j + n_{i-1}^j\right)}{(\Delta x)^2}\right). \qquad 2.7.1.$$

Solving for the distribution at time t^{j+1} in terms of the distribution at time t^j leads to a matrix equation

$$\bar{\bar{A}} \cdot n(\bar{x}, t^{j+1}) = \bar{\bar{B}} \cdot n(\bar{x}, t^j) \qquad 2.7.2.$$

where A and B are tridiagonal matrices with elements $(1 \pm \Delta t D / (\Delta x)^2)$ in the diagonals and $\mp \Delta t D / 2(\Delta x)^2$ in the off-diagonals. Quasiparticle loss can be incorporated by subtracting $1/\tau_{loss}$ form the diagonal elements of B. It is also possible to simulate the effects of localized loss centers by adding a loss term only to certain diagonal elements.

The boundary condition $\partial n/\partial x|_{x=\pm L/2} = n/L_{trap}$ translates into a difference equation at the last two grid points x_1 and x_0 in the absorber

$$\frac{n(x_1) - n(x_0)}{\Delta x} = \frac{n(x_0)}{L_{trap}} = \frac{n(x_0)}{\sqrt{D\tau_{trap}}}. \qquad 2.7.3.$$

It is implemented by setting the first elements in the top row of the matrix A to $(\Delta x/L_{trap}-1)$ and +1. The same the boundary condition holds on the other side of the absorber and leads to the same matrix elements in the bottom row. The initial distribution is assumed to be Gaussian, centered at the position of x-ray absorption with a width of 5 μm and normalized to the total number N_0 of initial quasiparticles. The matrix equation 2.7.2. can then be

solved iteratively to obtain the time evolution of the particle density in the absorber. We typically use a spatial grid size $\Delta x = 1\ \mu m$ and time steps $\Delta t = 50$ ns.

Adjustable parameters are the initial charge $Q_0 = eN_0$, the diffusion constant D in the absorber, an effective quasiparticle lifetime to account for uniform non-thermal losses and the trapping time at the absorber-trap interface. Q_0 is initially kept variable because of the uncertainty in the number of initial charges due to phonon escape into the substrate and in the uncertainty in quasiparticle multiplication upon trapping. We will constrain Q_0 later through numerical simulations of both processes (chapter 4.1. and 4.2.). We obtain an expression for the diffusion current $D\partial n/\partial x|_{x=\pm L/2}$ across the two interfaces that is used as an input to the rate equations in the junction area.

Simulation in Junction Electrodes

Quasiparticles enter the trap initially by diffusion from the absorber at Δ_{Ta}, but later on also through tunneling from the counterelectrode. They leave the trap either by tunneling or by recombination. Quasiparticles enter the counterelectrode by tunneling from the trap and then continue the tunneling processes until they either diffuse out into the leads or recombine. Inelastic phonon scattering determines the quasiparticle energy distribution. Tunneling times depend on the thickness of the film from which the quasiparticles tunnel, and are therefore different for trap and counterelectrode. We neglect spatial effects in the trap and the counterelectrode, as their small volume ensures that the quasiparticles are distributed uniformly on a time scale set by the tunneling time (cf. chapter 4.2.).

There are two versions of the simulations: A simpler, faster simulation neglects the quasiparticle energy distribution in the electrode. All quasiparticles are assumed to have scattered close to the gap edge such that reverse tunneling and direct backtunneling can be neglected. Tunneling times are given by their value at the gap voltage. This simulation is valid only for high bias voltages, because it assumes fast scattering in the counterelectrode

$(\tau_s(eV_{bias})<\tau_{tun}(eV_{bias}))$. The rate equations to determine the quasiparticle populations in the trap and the counterelectrode are then given by:

$$\frac{\partial N_{trap}}{\partial t} = +D\frac{\partial n}{\partial x}\bigg|_{x=\pm L/2} - N_{trap}\left(\frac{1}{\tau_{rec,eff}} + \frac{1}{\tau_{tun,trap}}\right) + \frac{N_{CE}}{\tau_{tun,CE}}$$

$$\frac{\partial N_{CE}}{\partial t} = +\frac{N_{trap}}{\tau_{tun,trap}} - N_{CE}\left(\frac{1}{\tau_{rec,eff}} + \frac{1}{\tau_{tun,CE}} + \frac{1}{\tau_{out}}\right) \qquad 2.7.4.$$

$$I(t) = \frac{eN_{trap}}{\tau_{tun,trap}} + \frac{eN_{CE}}{\tau_{tun,CE}}$$

The effective quasiparticle lifetime includes both thermal and self-recombination. The tunneling times ($\tau_{tun,trap} = 1.7$ µs and $\tau_{tun,CE} = 6.8$ µs for $V_{bias} = 70$ µV) are set by the normal state resistance of the junction and the volume of the junction electrodes. The only adjustable parameter is the outdiffusion time τ_{out} that describes how long the quasiparticle linger in the junction area before diffusing into the leads. One expects τ_{out} to be of order $(L_{jct}/2)^2/D_{Al} \approx 1$ µs. It allows us to neglect the spatial distribution of the charge in the junction area and to describe the detector with a one-dimensional model, simplifying the simulation significantly. Future modeling of the current pulse will involve two-dimensional simulations of the charge distribution.

The second program version of the quasiparticle dynamics in the junction area is used to examine current pulses at low bias voltage and retains the explicit energy dependence of the quasiparticle distribution in the trap and the counterelectrode. The energy is divided into bins of width $\Delta_{Al}/10$ and the rate equations for quasiparticles in the i-th bin now includes energy dependent rates for inelastic scattering and tunneling:

$$\frac{\partial N^i_{trap}}{\partial t} = +\sum_{j>i}\frac{N^j_{trap}}{\tau_s^{j\to i}} - \sum_{k<i}\frac{N^i_{trap}}{\tau_s^{i\to k}} - \frac{N^i_{trap}}{\tau^{i\to i+eV}_{tun,trap}} - \frac{N^i_{trap}}{\tau^{i\to i-eV}_{tun,trap}} + \frac{N^{i+eV}_{CE}}{\tau^{i+eV\to i}_{tun,CE}} + \frac{N^{i-eV}_{CE}}{\tau^{i-eV\to i}_{tun,CE}}$$

$$\frac{\partial N^i_{CE}}{\partial t} = +\sum_{j>i}\frac{N^j_{CE}}{\tau_s^{j\to i}} - \sum_{k<i}\frac{N^i_{CE}}{\tau_s^{i\to k}} - \frac{N^i_{CE}}{\tau^{i\to i-eV}_{tun,CE}} - \frac{N^i_{CE}}{\tau^{i\to i+eV}_{tun,CE}} + \frac{N^{i+eV}_{trap}}{\tau^{i+eV\to i}_{tun,CE}} + \frac{N^{i-eV}_{trap}}{\tau^{i-eV\to i}_{tun,CE}}$$

2.7.5.

Here $1/\tau_{tun}{}^{i\to j}$ is the tunneling rate for quasiparticles from the trap with initial energy E_i into final energies E_j. Energies are measured relative to the gap in the respective electrode and all tunneling processes conserve energy. Final energies are different for direct tunneling and pair mediated tunneling via the Gray effect (figure 2.7.1.). The last four terms of equation 2.7.5. correspond to processes A, D, B and C in figure 2.7.1., respectively. The terms for quasiparticle loss and outdiffusion remain unchanged and are omitted for clarity. There are two contributions to the current in positive direction (direct tunneling and backtunneling) and the two contributions in opposite direction (reverse tunneling and direct backtunneling). The net current (to the right in figure 2.7.1.) is given by the difference between them:

$$I(t) = \sum_i \frac{eN^i_{trap}}{\tau^{i\to i+eV}_{tun,trap}} + \frac{eN^i_{CE}}{\tau^{i\to i+eV}_{tun,CE}} - \frac{eN^i_{trap}}{\tau^{i\to i-eV}_{tun,trap}} - \frac{eN^i_{CE}}{\tau^{i\to i-eV}_{tun,CE}} \qquad 2.5.3.$$

Figure 2.5.5. shows a typical set of current pulses in response to an x-ray photon and their fits from the simulation. Except for a small discrepancy at the falling end of the current, where outdiffusion dominates and the one-dimensional simulation may no longer appropriately approximate the detector geometry, the simulation matches the observed waveforms well.

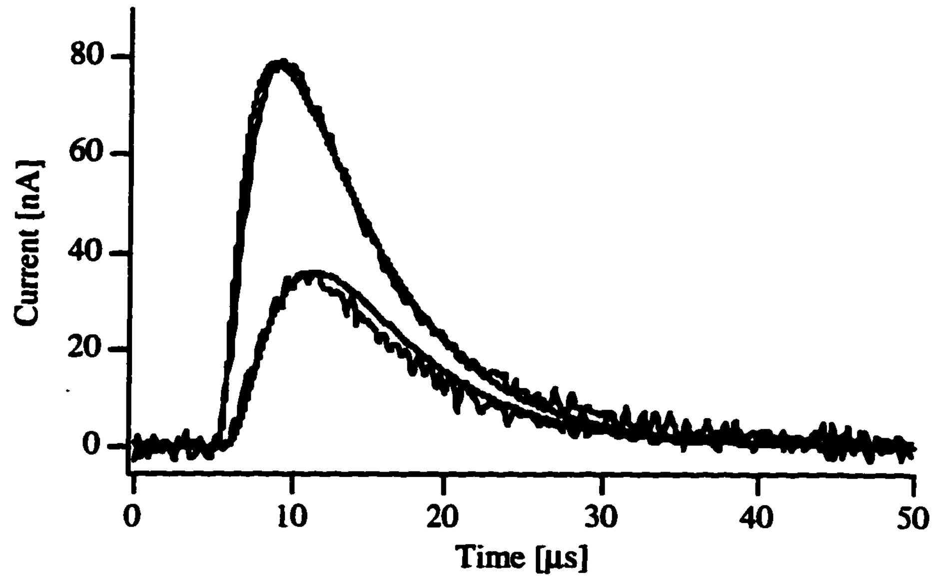

Figure 2.7.2.: Set of coincident pulses and their model fits

Of course, since we capture waveforms for uniform illumination of the device, we have to ensure that we can fit both peak currents and total charge and rise and fall times for events over the entire absorber with a few adjustable parameters. Each of these parameters (D, Q_0, τ_{loss}, τ_{trap}, τ_{out}) is determined from a different measurement. This severely constrains the range of acceptable fitting parameters and makes these simulations a powerful tool to investigate non-equilibrium quasiparticle dynamics in superconducting double junction detectors.

Chapter 3: Electronics

Any detector requires an electronic readout whose noise contribution does not exceed the intrinsic fluctuations of the device response. Noise considerations alone do not dictate whether to use a voltage, current, or charge sensitive preamplifier. The charge output of a detector gives the most direct measure of the energy of the incident radiation. However, since the signal current is proportional to the number of quasiparticles in the junction electrodes, current measurements are more closely related to the time-dependent processes inside a detector and therefore provide additional information for the analysis of their performance. A current sensitive preamplifier with large signal bandwidth for minimum pulse distortion is therefore our amplifier of choice. The signal charge can still be obtained in a later integration step. In this chapter, we will discuss the design and performance of a low noise, large bandwidth current preamplifier used for our experiments.

3.1. DC Voltage Bias vs. DC Current Bias

One additional issue in superconducting tunnel junction detectors arises from their highly non-linear I(V) characteristics and its sensitive dependence on temperature and magnetic field. Whenever the junction is embedded in a circuit whose load line intersects the I(V) characteristics at more than one point, the bias is unstable and can switch between intersections. These instabilities manifest themselves as small randomly spaced pulses at the preamplifier output whose magnitude and frequency depends sensitively on bias voltage and magnetic field. They add uncertainty to the measurement of an x-ray induced pulse if they overlap in time. In a single junction device, the magnetic field can always be chosen such that the zero voltage current is well suppressed below the thermal

dark current. However, small dissimilarities between the two junctions is a double junction device geometry render complete suppression of the zero voltage current in both junctions at the same magnetic field difficult.

Figure 3.1.1. shows the I(V) characteristics of one detector junction at a magnetic field that completely suppresses the dc Josephson current in the other junction. One can see two Fiske modes at 115 and 145 μV and indications of a small residual DC Josephson current at low voltage. The DC Josephson current peaks around V = 10 μV, rather than V = 0, because of noise fluctuations. They cause the current to temporarily exceed the critical value I_C and thus cause the bias to switch to a finite voltage even if the average current is less than I_C. Switching occurs more often as the average current approaches I_C and makes the dc Josephson current appear as a peak at finite voltage. At higher temperatures, a dc current bias is acceptable because even a 1 MΩ load line intersects the I(V) characteristics only once. However, if the temperature is lowered for lower noise, dc current biasing leads to several intersections and thus bias instabilities.

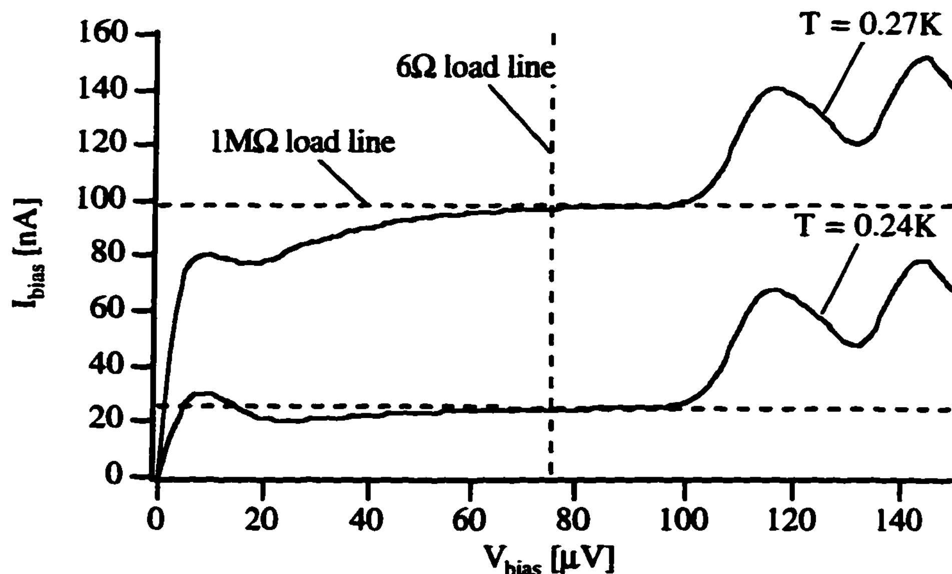

Figure 3.1.1.: Device I(V) characteristics at 0.27K and 0.24K showing Fiske modes at 110 μV and 140 μV and incomplete suppression of I_C. Noise fluctuations cause the "zero voltage current" I_C to appear as a peak at 10 μV (10/23/96).

We have solved the problem of switching of the voltage bias point by designing a current preamplifier with a dc voltage bias [Friedrich, 1997]. The detector is biased relative to an amplifier's inverting terminal which is held at virtual ground (figure 3.1.2.a). The slope of the dc load line is set by the sum of bias resistance, lead resistance and R_F/A_{OL}, where A_{OL} is the amplifier's dc open loop gain.

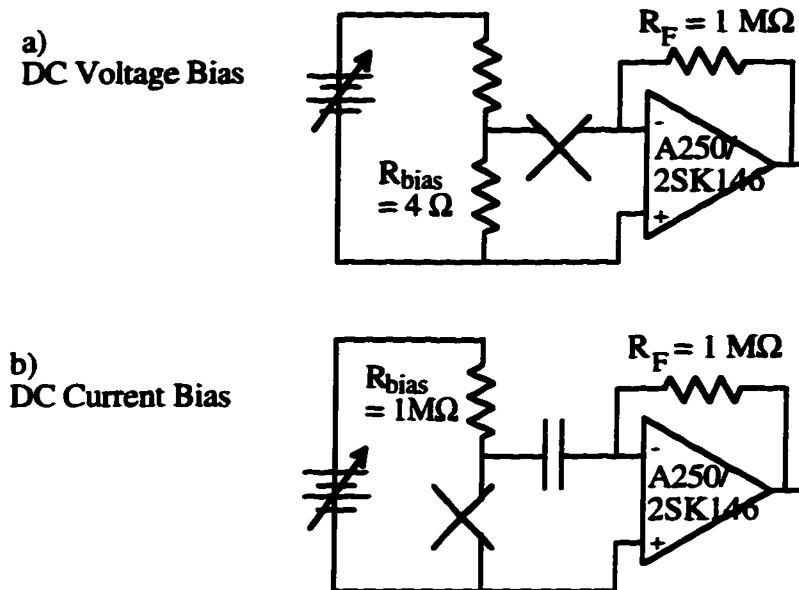

Figure 3.1.2.: Schematics of the dc voltage and current bias circuits. The x represents the tunnel junction detector. We employ the voltage bias circuit.

A dc voltage bias also helps to keep the bias point constant, as compared to a dc current bias whose supply has the same fractional stability. Earlier experiments had been performed with a dc current bias circuit (figure 3.1.2.b). They had shown a slow 1% drift in the magnitude of the charge output from x-ray absorptions during a half hour run. The drift was a result of the bias dependence of the collected charge, the cause of which will be discussed in chapter 4.4. A 1% drift is unacceptable for high resolution detectors.

When using this voltage bias circuit with a double junction device, it is important to electrically separate the two virtual grounds. For this reason, we bias both junctions

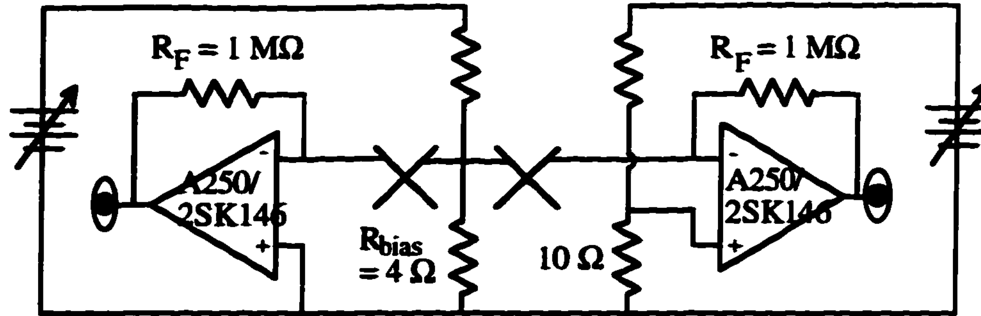

Figure 3.1.3.: Schematic of the double junction bias circuit

from a single variable voltage source relative to their respective op-amp's inverting terminal. To independently adjust bias points, the reference voltage of one of the op-amps can be varied with a second voltage source as shown in figure 3.1.3.

3.2. Circuit Design

The Amptek A250 transresistance amplifier is a modern low-noise, large-bandwidth preamplifier. An external FET input stage can be selected to match the device capacitance for optimum performance. We use a Toshiba 2SK146 JFET, the dual version of the 2SK147, at room temperature with $e_n = 0.5\ nV/\sqrt{Hz}$ and negligible current noise [Richards, 1994]. We obtain a gain-bandwidth product of 1.6 GHz with a dominant pole at 65 kHz. At low frequencies, the open-loop gain drops to 5000 because of a reduced performance of the A250 (Figure 3.2.1.).

To keep the feedback loop stable for arbitrary input impedances the open loop phase shift must be less that 180° for all frequencies where the loop gain satisfies

$$A_{OL}\beta \equiv A_{OL}\frac{Z_{in}}{Z_F + Z_{in}} \geq 1. \qquad 3.2.1.$$

This ensures that closing the loop does not result in positive feedback, since negative feedback is equivalent to adding another 180° phase shift. The open loop gain of the A250 introduces 90° phase shift well above its dominant pole at 65 kHz, and for a typical dynamical resistance of order 10 kΩ the input capacitance of 250 pF introduces another pole in the same frequency range. The associated phase shift can be compensated by adding a small capacitor C_F to the feedback resistor. Since C_F limits the signal bandwidth to $1/2\pi R_F C_F$, it must be chosen to be as small as possible. In earlier experiments we have chosen a value of 0.5 pF such that the resulting pole lies close to the frequency where $A_{OL}=1/\beta$ in the uncompensated case (figure 3.2.1.) [Graeme, 1995]. This limits the signal bandwidth to 300 kHz, which is still acceptable, but ensures amplifier stability for all input impedances. Later it turned out that under typical bias conditions the parasitic capacitance of the feedback resistor of order 0.1 pF is sufficient to keep the loop stable.

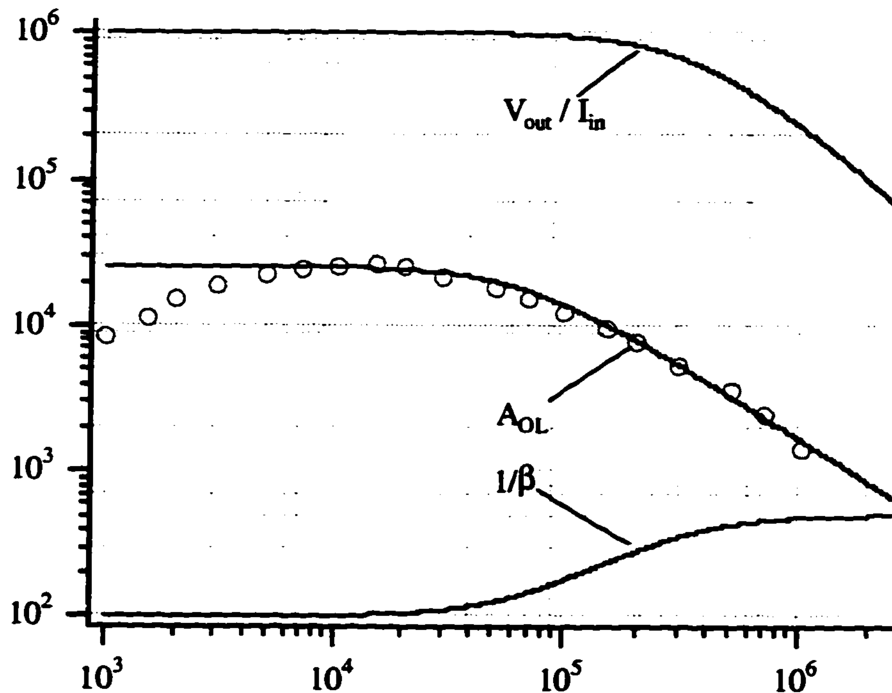

Figure 3.2.1.: Open-loop voltage gain A_{OL}, inverse feedback reduction factor $1/\beta$ and resulting signal gain V_{out}/I_{in} of the phase compensated current amplifier. The measured open-loop gain of the A250 (circles) approaches a low frequency limit of 5000.

This greatly increases the signal bandwidth. Marginal stability will result in suppressed oscillations in the frequency range where he total phase shift approaches 360° that manifest themselves in a wide peak of the noise spectrum [Graeme, 1995].

A complication in our biasing scheme arises from the fact that the internal circuitry of the A250 holds its input at constant +3 V. This constrains the source-drain voltage and the bias current of the FET, which may not be compatible with a gate voltage close to ground. We have solved this problem by adding a nulling loop to the drain of the FET. Its purpose is to sense the gate voltage and increase the bias current of the FET until the feedback required from the A250 to keep the gate voltage at ground is effectively zero (Figure 3.2.2.). More precisely, the nulling loop matches the gate voltage to the reference voltage at the non-inverting terminal of the OP97 integrator. In figure 3.2.2. the non-inverting terminal of the right-hand OP97 is shown to be grounded. However, in one of the boards we have this terminal at a small non-zero voltage, and adjust this voltage to independently set the bias of the second junction (cf. figure 3.1.3.).

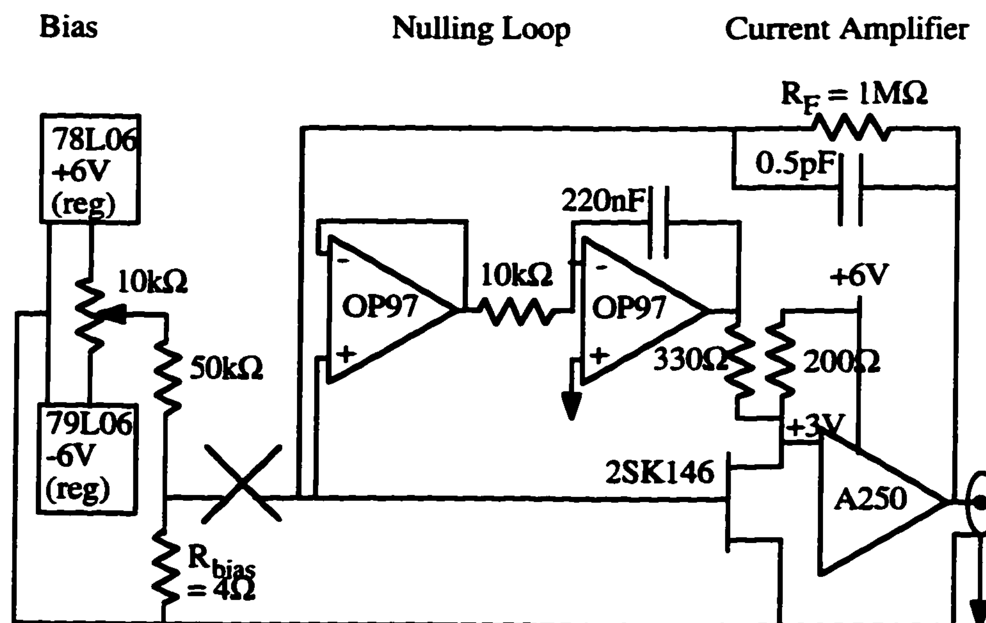

Figure 3.2.2..: Circuit diagram for a single junction readout. The RC filters at the ±6 V regulator outputs and the INA 110 instrumentation amplifier for the dc voltage readout have been omitted for clarity.

This feedback scheme will be saturated whenever the A250 output cannot feed enough voltage back to FET gate to compensate for voltages from the bias circuit. This is a concern when the device resistance is low and a large fraction of the bias voltage appears at the FET gate while the dc feedback factor $(R_{bias}+R_{dyn})/R_F$ is low. It is therefore important to keep the bias voltage very close to ground when biasing a device on the zero voltage current where its resistance is zero. Alternatively, we can switch the feedback resistor to $R_F = 10\ k\Omega$ to guarantee the maximum feedback exceeds the total bias voltage range. This 10 kΩ feedback resistor is used to trace the full I(V) curve, but has too much Johnson noise at room temperature to provide low-noise signal amplification.

The requirements of the input stage of this nulling loop are low input offset voltage and low current noise. The OP97E with $V_{offset} < 25\ \mu V$ and $i_n = 20\ fA/\sqrt{Hz}$ is our present choice. Its voltage noise at frequencies above 70 Hz is filtered out with the follower and the integrator as shown. Placing the integrating capacitor into the feedback loop guarantees stability of the nulling circuit for arbitrary input impedances.

The circuit components are selected for low electronic noise keeping in mind the need for large signal bandwidth for undistorted signal measurements. At present, the electronic noise is well below the device noise, but not below the Fano limit. We outline a procedure to select component values and optimize noise performance in the future.

The amplifier's total input current noise density is given by

$$i_{n,total} = \sqrt{i_n^2 + e_n^2 / Z_{in}^2}$$

$$\text{with } i_n^2 = 2eI_{bias} + 4k_BT / R_F$$

$$e_n^2 = 4k_BTR_{bias} + 4k_BT(2/3g_{m,FET}) \qquad 3.2.2.$$

$$Z_{in} = R_{dyn} // (C_{FET} + C_{jct} + C_{leads}).$$

The current noise i_n is set by the shot noise of the bias current I_{bias} and the Johnson noise of the feedback resistor R_F. The FET contributes negligibly to i_n [Richards, 1994]. During injection experiments, there is an additional contribution of $\sqrt{(4k_BT/R_F)}$ from the 1 MΩ injection resistor. We have neglected the input current noise of the nulling loop and the 2SK146 FET, which are much smaller in magnitude. The voltage noise e_n is set by the Johnson noise of the bias resistor R_{bias} and the input voltage noise of the FET [Horowitz, 1989]. For typical devices, the FET voltage noise e_n is usually somewhat above the ideal value predicted from the measured transconductance $g_{m,FET}$. The input impedance is determined by the junction's dynamic resistance at the bias point R_{dyn}, in parallel with the impedance of the input capacitance, which has contributions from the FET, the junction and the leads.

The noise spectrum at signal frequencies (tens of kHz) approaches the value $\sqrt{i_n^2 + e_n^2 / R_{dyn}^2}$. It is therefore important to operate the devices at low temperature where their dynamic resistance exceeds 10 kΩ to suppress the voltage noise contribution. At higher frequencies, when the input impedance is dominated by its capacitance, the total noise approaches a limit $e_n \cdot 2\pi f C_{in}$. The voltage noise depends on the FET's transconductance (eqn. 3.2.2.), which in turn is proportional to its capacitance. The high frequency voltage noise is therefore proportional to

$$\frac{e_n}{Z_{in}} \propto \frac{(C_{FET} + C_{jct} + C_{leads})}{\sqrt{C_{FET}}}. \qquad 3.2.3.$$

This expression is minimized for $C_{FET} = C_{jct} + C_{leads}$. For a given junction and lead capacitance, one therefore chooses a FET with maximum transconductance (i.e. minimum noise) per unit capacitance and adds them in parallel until their capacitances are matched. For our detectors with 50 pF junction capacitance and comparable lead capacitance, we choose two 2SK147 JFETs with a total capacitance of 170 pF, a

transconductance of 100 mS and a voltage noise of 0.5 nV/√Hz. The FET capacitance is somewhat higher than suggested by the matching condition. This is not a concern at present, as the electronic noise does not limit the device resolution. It is more important to utilize the large transconductance and consequently large open loop gain of the composite amplifier, so that the waveform distortion of the current pulses by the amplifier is minimized.

The bias resistor $R_{bias} = 4\ \Omega$ is at room temperature and chosen small so that its Johnson noise is negligible compared to the FET voltage noise, while still allowing an acceptable range of bias voltages.

The feedback resistor R_F is chosen to be large for high signal gain and low current noise, keeping in mind the constraints imposed by its parasitic capacitance and the op-amp's finite open loop gain. Its maximum value is set by the requirements that its parasitic capacitance of order 0.1 pF not limit the signal bandwidth and that the voltage feedback to the FET input be sufficiently large to keep the nulling circuit functional. A 1 MΩ resistor with $\sqrt{(4k_BT/R_F)} = 0.13$ pA/√Hz is a good compromise. Its current noise is of the same order as the shot noise of typical bias currents at 0.25 K. Its parasitic capacitance does not limit the signal gain even for maximum signal frequencies around 300 kHz. And even for zero device resistance, bias voltages below ±15 μV will not lead to saturation of the A250 output.

The output of the A250 is split and amplified by two INA110 instrumentation amplifiers configured for a gain of 10 each. One is used for the pulse output and is fed directly into the HP scope. The other is used to read out the dc bias current, passed through a unity gain ISO100 optical isolation amplifier and displayed on an XY recorder. The dc voltage is measured directly across the device with an INA110 with a gain of 500, whose output is also passed through an ISO100 isolation amplifier to keep any signal from the XY recorder from feeding back to the input side of the circuit.

The readout circuits for the two junctions are enclosed in separate shielded boxes to eliminate crosstalk. They are battery powered, with separate supplies for each of the two current amplifier gain stages, the bias circuit and the dc instrumentation amplifiers.

3.3. Circuit Performance

For the component values discussed above we obtain an amplifier with a voltage noise of 0.5 nV/√Hz for a FET input capacitance of 170 pF and a current noise of 0.16 pA/√Hz, dominated by the Johnson noise of the room temperature feedback resistor. Figure 3.3.1. shows the noise added when the junction is connected to the amplifier input. A fit to the spectrum (solid line) gives a total current noise of 0.26 pA/√Hz and a total input capacitance of 280 pF during operation at 0.24K (I_{bias} = 30 nA, $R_{dyn} \geq$ 10 kΩ).

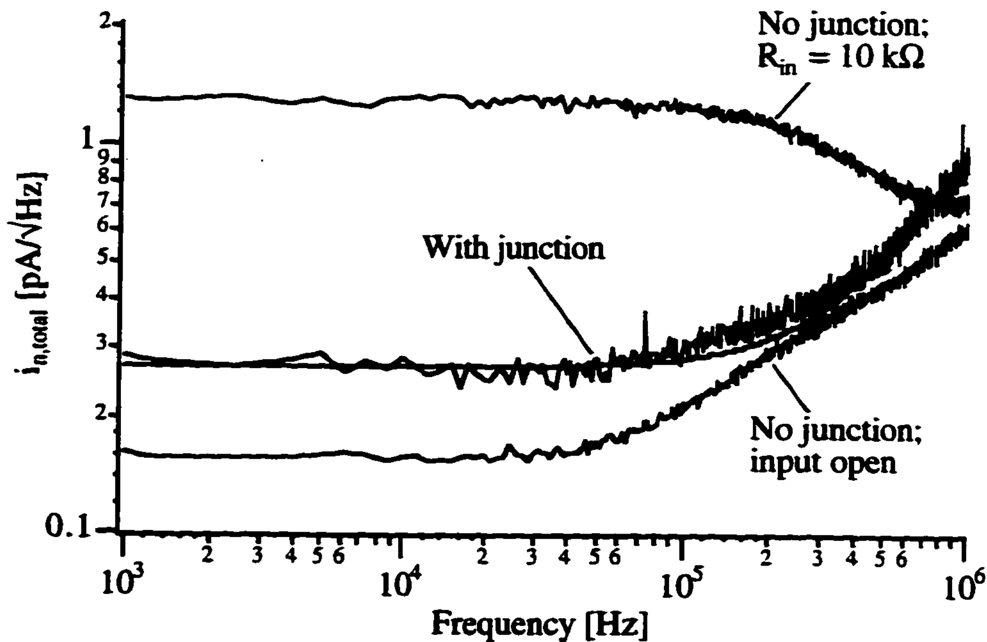

Figure 3.3.1.: Amplifier noise characteristics

The increase in capacitance agrees well with a junction capacitance of 50 pF and a lead capacitance of the same order. The white low frequency noise is now comprised of 0.13 pA/√Hz from the feedback resistor, 0.13 pA/√Hz from the injection resistor and a residual 0.18 pA/√Hz from the shot noise of the bias current. The FET contribution is reduced to negligible 0.05 pA/√Hz due to the high dynamic resistance above 10 kΩ. The noise increase at higher frequencies reflects the increased input capacitance due to the leads and the junction.

The noise contribution of 0.18 pA/√Hz for the 30 nA bias current is somewhat above the expected value of $\sqrt{2eI_{bias}} = 0.1 \mathrm{pA} / \sqrt{\mathrm{Hz}}$. That is partially due to the fact that in SIS tunnel junctions both quasiparticles and pairs contribute to the noise according to [Rogovin, 1974]

$$i_n^2(f) = 2e\left[I_{qp} + 2I_{pair}\right]\coth\left(\frac{eV}{2k_BT}\right). \qquad 3.3.1.$$

The physical origin of the hyperbolic cotangent terms lies in the fact that the noise contributions from forward and reverse tunneling do not cancel each other. Pairs add twice as much noise as quasiparticles, as they carry twice the charge. We can estimate the quasiparticle contribution to the bias current from [van Duzer, 1981]

$$I_{qp}(V) = \frac{2(V + \Delta / e)}{R_{nn}}\sqrt{\frac{2\Delta}{eV + 2\Delta}}\exp\left(\frac{-\Delta}{k_BT}\right)\sinh\left(\frac{eV}{2k_BT}\right)K_0\left(\frac{eV}{2k_BT}\right). \qquad 3.3.2.$$

Under typical bias conditions, at least 80% of the current is carried by quasiparticles, and we therefore do not expect the total shot noise to exceed the value of $2eI_{bias}$ by more than 25%.

The observed excess noise of the device may be related to downconversion of RF noise due to the strong non-linearity of the I(V) characteristics. At a bias voltage V, the ac Josephson effect produces an ac signal at frequency 2eV/h. The junction's non-

linearity then downconverts noise fluctuations from the shot noise or the FET around that frequency into the amplifier's pass band. There is evidence for this effect in the fact that close to the non-linearity in the I(V) characteristics the low frequency noise increases more strongly than expected from the decrease in dynamic resistance by itself. The noise data in figure 3.3.2. display the total current noise density averaged over the frequency range from 5 to 50 kHz. The increase at low and high bias is more than twice as much as expected for a total voltage noise of $e_n = 0.5$ nV/√Hz, dominated by the FET.

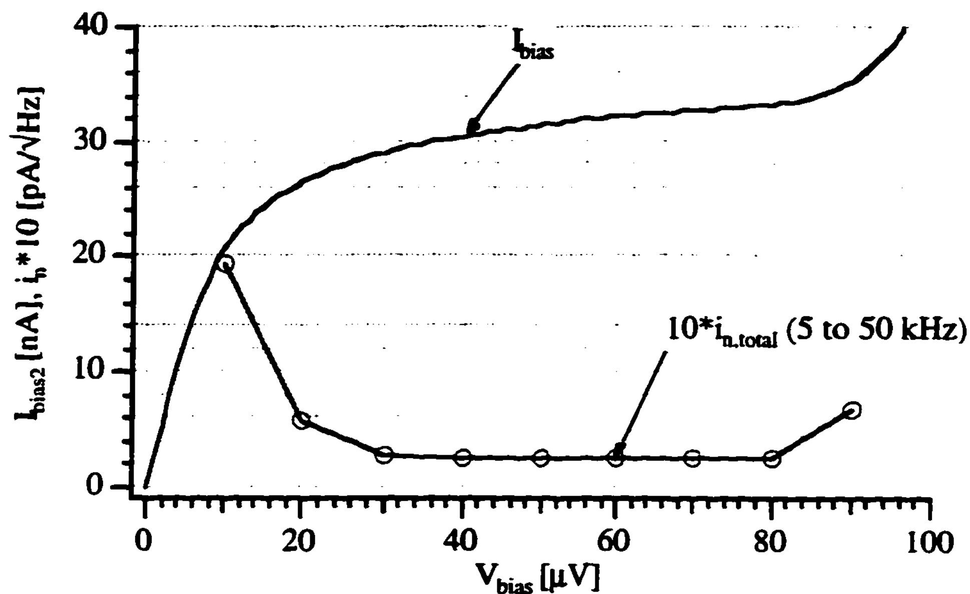

Figure 3.3.2.: Bias dependence of average low frequency current noise

Electronic pulses injected into the junction have been measured with an electronic noise of 13 eV FWHM. The pulse shapes are taken from our model simulation to ensure they have the same spectral composition as the x-ray induced pulses. The optimum resolution of the injected pulses is identical for current and charge measurements. In the charge sensitive mode after numerical integration, it corresponds to an uncertainty of the charge measurement of $\sigma_Q = 3400\ e^-$. In the current sensitive mode, the width measured for the injected pulses is 92 pA rms. This agrees with a total standard deviation of

$$\sigma = \sqrt{\int (i_n^2 + e_n^2 / Z_{in}^2) F(f) df} \qquad 3.3.3.$$

using the appropriate filter function F(f) to determine the effective bandwidth and the measured baseline noise shown in figure 3.3.1.. For best noise performance, we typically use digital Butterworth filters. Their spectral response for an n-th order bandpass filter from $f_{c,low}$ to $f_{c,high}$ follows the analytic expression [Horowitz, 1989]

$$F(f) = \frac{1}{\sqrt{1+(f_{c,low}/f)^{2n}}} \cdot \frac{1}{\sqrt{1+(f/f_{c,high})^{2n}}}. \qquad 3.3.4.$$

In the current sensitive mode, the optimum resolution is obtained for a fifth order 65 kHz Butterworth low pass filter. In the charge sensitive mode, we use a 4 to 65 kHz band pass filter. The electronic resolution is presently limited by the shot noise of the junction current. The excess noise does not cause any problems, because the total electronic noise is at present still well below the measured device noise. Also, the measured noise, including the excess noise, decreases with decreasing thermal current.

In the future, the electronic noise can be further reduced with the following modifications. Cooling the feedback resistor R_F, the pulse injection resistor R_{inj} and the bias resistor R_{bias} will reduce their Johnson noise. Then, using smaller junctions will diminish the junction capacitance and the shot noise and increase the dynamic resistance at the bias point. The input capacitance will be further reduced by using a capacitance matched FET ($\Rightarrow C_{FET} = 8$ pF for the 2SK 152) and placing the FET onto the cold stage ($\Rightarrow C_{leads} = 1$ pF). Ultimately, operating the device at even lower temperatures will further diminish the shot noise and increase the dynamic resistance.

The projected performance of the circuit assuming the same efficiency of charge collection is summarized in the table below. The electronic noise is calculated from equation 3.3.3. assuming an unchanged fraction of excess shot noise of the bias current.

Bias currents, junction capacitance and dynamic resistances are assumed to scale with device area, and leakage currents are not expected to add more than 0.1 nA to the BCS value of the subgap current. Table 3.3.1. shows how electronic noise below the Fano limit can be achieved.

Design modification	i_n [pA/√Hz]	e_n [nV/√Hz]	C_{in} [pF]	El. Noise [eV]
Present Setup	0.26	0.56	280	13
Cold resistors R_F, R_{inj}, R_{bias}	0.18	0.5	280	9.2
10 x smaller junction	0.056	0.5	230	3.2
Cold 2SK152	0.056	1.2	15	2.7
T = 0.1K	0.01	1.2	15	0.6

Table 3.3.1.: Projected circuit performance. Design modifications are incremental. Each row includes all changes indicated in the preceding rows

The amplifier's signal bandwidth can be inferred from the roll-off of the noise spectrum of a 10 kΩ resistor at room temperature in place of the tunnel junction (Figure 3.3.1.). With a feedback impedance of 1 MΩ // 0.5 pF, the current gain rolls off at 300 kHz as expected. Without any feedback capacitance except for the parasitic capacitance of the feedback resistance R_F, the current gain is constant up to 1 MHz. Current rise times and peak heights are amplified with less than 5% distortion for the entire range of absorption locations with minimum current rise times of 1 μs. This allows us to extract physical information from the shape of the current pulses.

The slope of the dc load line is set by the sum of the bias resistance, lead resistance and R_F/A_{OL}, where A_{OL} is the dc open loop gain of the composite amplifier. We have measured a dc load line resistance of 6 Ω by tracing the bias voltage of a device during warm-up. It is dominated by the 4 Ω bias resistor, indicating that the input impedance into the feedback loop is reduced to about 1Ω. The open loop gain of the A250/2SK146 amplifier is only about 5000 at dc (figure 3.2.1.), and the low input

impedance is due to the large dc open-loop gain of 120 dB for the OP-97 in the nulling loop. It is low enough for our applications given that typical device resistances are around 10 kΩ.

In summary, we have built a low noise current amplifier with a 6Ω dc load line. Its bandwidth exceeds 300 kHz and is sufficient to amplify x-ray induced current pulses from our devices with less than 5% distortion. The electronic noise is 13 eV at 6 keV, limited by the shot noise of the thermal dark current. There is some excess noise in the detectors which decreases with decreasing temperature, possibly related to the ac Josephson effect. Further reduction of the electronic noise below the Fano limit is possible by reducing the junction area, operating temperature and input capacitance.

Chapter 4: Non-Equilibrium Quasiparticle Dynamics

The quasiparticles generated after the absorption of an x-ray photon diffuse through the absorber until they are trapped and produce current pulses in both tunnel junctions. In this chapter, we will examine how to determine the relative time scales for the various processes from the analysis of the current pulses and computer simulations. The double junction device geometry provides a powerful tool to study quasiparticle dynamics, because spatial resolution allows separating the contributions of the individual processes.

4.1. Quasiparticle Generation

The absorption of an x-ray photon initially creates a single photoelectron which will ionize atoms along its trajectory and share its energy with other electrons on a femtosecond time scale through Coulomb interactions [Chi, 1981]. Once the average electron energy is comparable to the Debye energy, phonon emission provides an alternative relaxation mechanism. Phonons with energy $E_{ph}>2\Delta_{Ta}$ can break Cooper pairs, thereby creating quasiparticles. The relaxation process is then governed by the exchange of energy between quasiparticles and phonons through pair breaking and phonon emission. At the end of this cascade, a certain fraction of the x-ray energy in the absorber film is converted into quasiparticles and the remainder resides in subgap phonons whose energy is no longer sufficient to break pairs.

We have simulated this process to estimate the efficiency of energy conversion and its average time and length scales. We neglect the very first part of the relaxation, dominated by electron-electron interactions, as it is very fast on a time scale of all other processes. We divide the energy up to the maximum phonon energy E_{Debye} into energy

bins E_i of equal width 0.2Δ and assume that all quasiparticles initially are uniformly distributed between Δ and E_{Debye} such that their total energy is equal to the initial x-ray energy. Quasiparticles leave energy bin E_i by phonon emission in a characteristic energy dependent inelastic scattering time $\tau_s(E_i)$ (cf. figure 2.6.2.). They scatter into bin E_i either by phonon emission from a higher energy state or when a phonon breaks a pair. Phonons are generated by inelastic scattering and, if the phonon energy exceeds 2Δ, it can break a Cooper pair with a characteristic pair-breaking time τ_{pb}. Phonon absorption is neglected for simplicity. Quasiparticle recombination is neglected, because characteristic time scales are much longer and recombination phonons would most likely break Cooper pairs again. The rate equations for the quasiparticle population N_{qp} at energy E_i and the phonon population N_{ph} at energy bin E_k are then given by

$$\begin{aligned} \frac{\partial N_{qp}^i}{\partial t} &= -\frac{N_{qp}^i}{\tau_s^i} + \sum_{j>i} \frac{N_{qp}^j}{\tau_s^{j\to i}} + \sum_{k>2\Delta} \frac{N_{ph}^k}{\tau_{pb}^{k\to i}} \\ \frac{\partial N_{ph}^k}{\partial t} &= -\frac{N_{ph}^k}{\tau_{pb}^k} + \sum_{j>\Delta+k} \frac{N_{qp}^j}{\tau_s^{j\to j-k}} - \frac{N_{ph}^k}{\tau_{esc}} \end{aligned} \quad . \qquad 4.1.1.$$

Pair breaking rates go to zero for phonon energies below $2\Delta_{Ta}$. Initial calculations have neglected phonon escape into the substrate ($1/\tau_{esc} = 0$). This term was added later to estimate the magnitude of the effect. We iterate the above rate equations using a fourth order Runge-Kutta method until no pair breaking phonons are left and the number of quasiparticles no longer changes. At each iteration we confirmed that the total energy adds up to 100%. Figure 4.1.1. shows the energy distribution during the initial relaxation in tantalum. The quasiparticles transfer most of their energy into the phonon system within one picosecond. Assuming an effective diffusion constant of $D = 180$ cm^2/s (cf. chapter 4.2.), approximately 90% of the excitations will have spread over a distance of order $3\sqrt{D\tau}$ ≈ 4000 Å by that time.

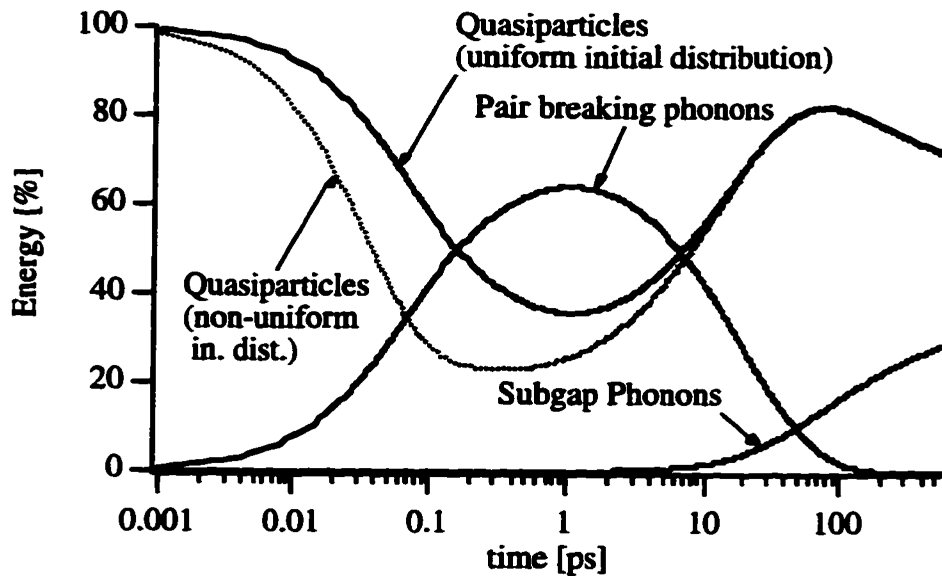

Figure 4.1.1. Energy distribution during the energy relaxation process in Ta for uniform (solid line) and non-uniform (dotted line) initial energy distribution

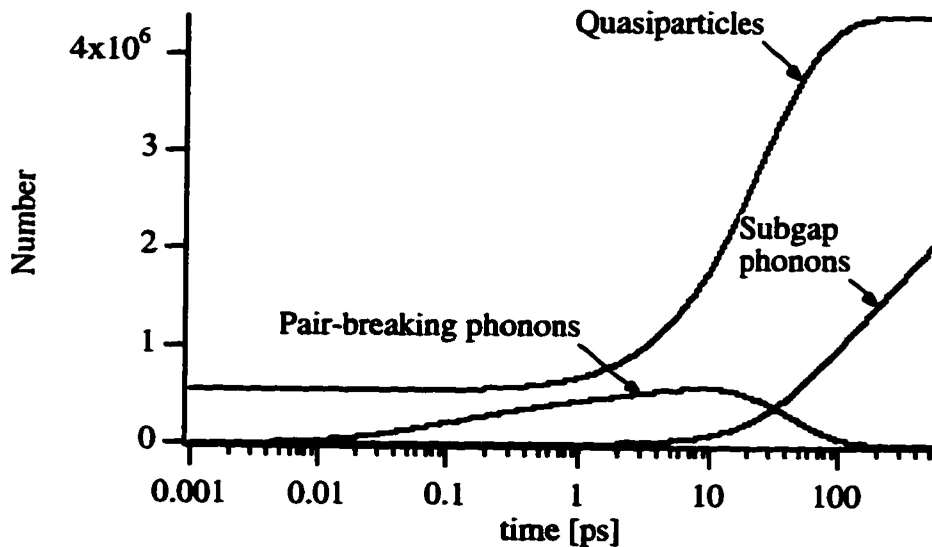

Figure 4.1.2.: Number distribution during the initial relaxation process

Most phonons still have an energy above $2\Delta_{Ta}$ and transfer energy back into the quasiparticle system by pair breaking. After about 150 ps most pair breaking phonons will have been absorbed and most quasiparticles will have scattered to energies below 3Δ, where the phonons they subsequently emit have energies below 2Δ. After 150 ps, the

energy in the quasiparticle system still decreases by emission of subgap phonons, but the number of quasiparticles number remains almost constant (figures 4.1.1. and 4.1.2.). For an x-ray energy of 5.89 keV, we obtain a total number of $4.3 \cdot 10^6$ quasiparticles, corresponding to an average ionizing energy $\varepsilon = 1.37$ meV $= 1.96\Delta_{Ta}$. This can be compared to the value of 1.7Δ that has been calculated for Sn [Kurakado, 1982].

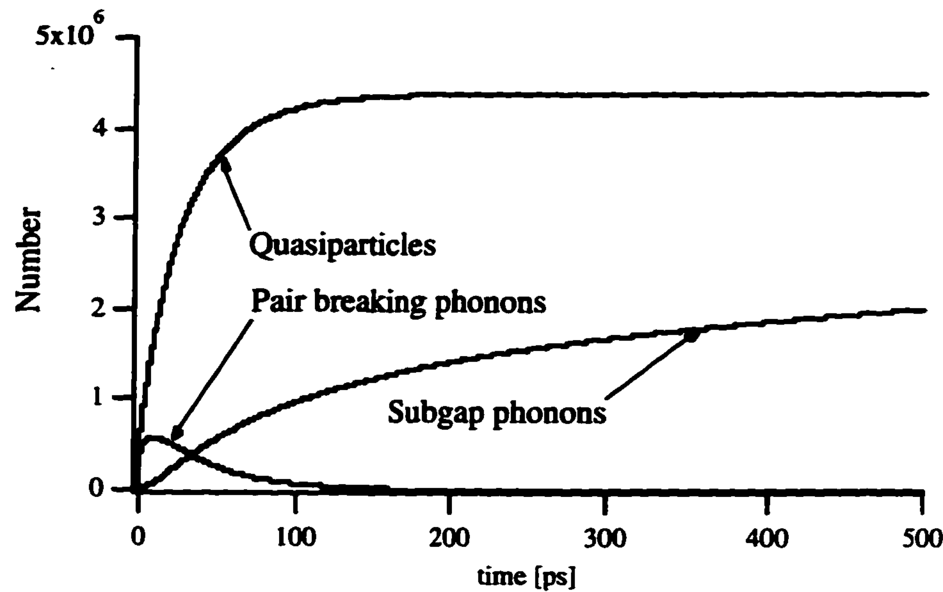

Figure 4.1.3.: Number distribution during the initial relaxation process

To ensure that these numbers do not depend on the somewhat arbitrarily chosen initial conditions, we have repeated the simulation with all initial quasiparticles at the Debye energy, the number chosen such that the total energy is the same (figure 4.1.2., dotted line). The final number of quasiparticles is different by less than 0.1%, reflecting the fact that information about the initial distribution is washed out by the correlated nature of the relaxation. These correlations are responsible for a Fano factor $F<1$ that reduces the fluctuations in the number of initial quasiparticles and consequently the resolution limit of superconducting x-ray detectors below the Poisson limit.

It takes about 150 ps until 99% of the final number of quasiparticles have been generated. By that time, the hotspot will have spread over a distance of $3\sqrt{D\tau_{hotspot}} \approx 5$ µm.

This imposes lower limits on the absorber dimension, because the average superconducting energy gap should be constant over the region of energy relaxation.

Phonon Escape into Substrate

So far we have neglected phonon transmission into the substrate. We have added this effect to the rate equations through an energy independent time scale τ_{esc}. In the limit where the film thickness d = 6000Å exceeds the phonon mean free path against pair breaking $c_{ph}\tau_{pb}$, the phonon escape time is given by $\tau_{esc}=4d/\alpha c_{ph}$ [Gray, 1971]. The average phonon transmission coefficient into the substrate α has a measured value of 0.3 in our devices (cf. chapter 5.1.), in good agreement with the literature [Kaplan, 1979]. For an average phonon velocity in tantalum of $c_{ph,Ta} = 2.8 \cdot 10^5$ cm/s and a pair-breaking time $\tau_{pb} = 23$ ps, the predicted escape time is 2.8 ns.

When including phonon escape into the substrate, we find a total number of initial quasiparticles of $4.26 \cdot 10^6$, a reduction by about 1%. The 1% loss is calculated as if the energy were to relax uniformly throughout the absorber thickness. However, there is a concern that the fraction of energy lost into the substrate depends on the distance of the photoelectric absorption from the absorber-substrate interface. An absorption event near the interface might cause more than 1% loss into the substrate if, when the hotspot hits the bottom of the film, most of its energy rests in the phonon system. An absorption event near the top of the film will suffer a reduced loss because the hotspot will have to expand to the interface before phonons can get lost. With the present simulation, we cannot make a quantitative statement about the magnitude of the loss variations. A 1% variation of the initial charge due to different degrees of phonon escape appears possible.

To simulate the effects of phonon loss correctly one would have to include the spatial propagation of the hotspot in the simulation. Experimentally, one can also test the resolution broadening due to the height dependence with a thin absorber, where the hotspot spreads throughout the absorber faster. Ultimately, the absorber may have to be put on a

thin membrane to reduce the loss of pairbreaking phonons into the substrate completely in order to combine high absorption efficiency with high energy resolution.

The energy relaxation process in aluminum is shown in figure 4.1.4. It is qualitatively similar to tantalum, but since the electron phonon coupling is weaker, the characteristic time scales are much longer. It takes about 3 ns until the energy of the pair breaking phonons drops below 1%. This is an upper limit of the relaxation time in the devices with the aluminum trap over the entire tantalum absorber, where the hotspot will spread out evenly in vertical direction in the two films.

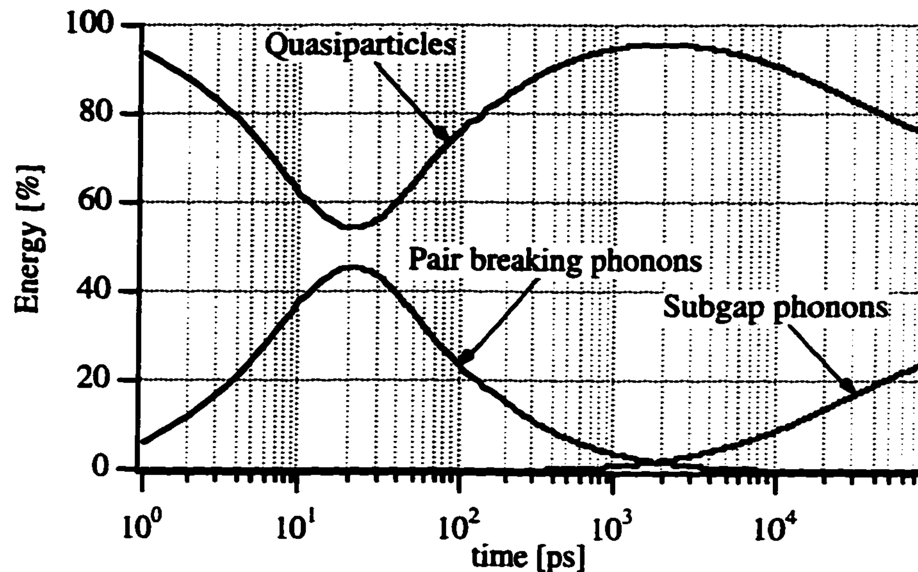

Figure 4.1.4.: Energy relaxation in aluminum

The results of the simulations are summarized in the table below. The x-ray energy eventually divides almost equally into quasiparticles and subgap phonons for both materials. Time scales for energy conversion are faster in tantalum than in aluminum, resulting in a smaller hotspot size in tantalum. The z-dependent loss of pairbreaking phonons into the substrate could potentially cause of order 1% excess fluctuations at 6 keV in our devices. That problem can be addressed by depositing the device on a thin membrane.

	Tantalum	Aluminum
Average ionizing energy ε	1.97 Δ_{Ta}	1.95 Δ_{Al}
Fraction of x-ray energy converted into qp	51 %	51 %
Initial number of qp N_0 (E_x = 5.89 keV)	$4.3\cdot10^6$ e$^-$	$17.7\cdot10^6$ e$^-$
Hotspot size ($\approx 3\sqrt{D\tau_{hotspot}}$)	5 µm (D=180cm^2/s)	60 µm (D=1250cm^2/s)

Table 4.1.1.: Summary of quasiparticle generation in tantalum and aluminum

Gap Suppression

These result present an upper limit for the number of initial quasiparticles. A more detailed model would take into account quasiparticle recombination, phonon reabsorption and the temporary gap suppression caused by the localized deposition of energy. Quasiparticles that have scattered into energy levels below the bulk value of the gap will condense into Cooper pairs once the gap regains its bulk value. Also, phonons with energy below the bulk gap will no longer be able to break Cooper pairs if they diffuse out of the region of depressed gap or if the gap regains its equilibrium value. The expansion of the hotspot volume depends on the diffusion of quasiparticles and phonons and the relaxation process will vary with the absorber's mean free path. These effects have been simulated for a variety of superconductors of different purity [Zehnder, 1995]. In clean Ta films gap suppression reduces the quasiparticle conversion efficiency by about 10%.

Fano Factor

The correlated nature of the relaxation process accounts for a Fano factor $F<1$. If a quasiparticle scatters inelastically and emits a phonon with energy $E>2\Delta$, the phonon will create two additional quasiparticles, because phonon escape into the substrate is small. If a quasiparticle emits a subgap phonon with $E<2\Delta$, no additional quasiparticles will be generated. The probability of each process is not constant throughout the relaxation process, as required for a random-walk type distribution. Initially, emission of phonons

with $E>2\Delta$ is much more likely, while phonon emission with $E<2\Delta$ dominates at the end of the relaxation. The exact ratio depends on the energy of the quasiparticle and consequently on the result of the previous scattering event. That renders the quasiparticle generation more predictable than a random walk process and reduces the fluctuations in the initial quasiparticle number below the $\sqrt{N_0}$ value expected for a Poisson distribution. The Fano factor reflects the degree of reduction. It can be calculated in Monte-Carlo simulations. In Sn and Nb it has a value $F = 0.2$ [Kurakado, 1982; Rando, 1992], and in other superconductors it is expected to be similar. Fluctuations in the energy stored in the quasiparticle system are then given by $\varepsilon\sqrt{(FN_0)} = \sqrt{(F\varepsilon E_x)}$.

4.2. Quasiparticle Diffusion

Quasiparticles propagate through the absorber film by diffusion. The double junction device geometry allows measurement of the effective diffusion constant from the time delay between the two signals. The *difference* in arrival time will depend on the different average distance over which the quasiparticles have diffused, as all other processes inside the junction area will affect both signals equally. Delay time measurements allow studying just the effects of diffusion, as opposed to analyzing Q_1 vs. Q_2 scatter plots, which yield information on the relative time scales of diffusion and loss.

We define a delay time between two pulses as the time difference at which they cross a specified threshold level (inset figure 4.2.1.). Typically, we choose a threshold just above the noise level to avoid possible influence of waveform distortion by the amplifier electronics. Since the absorption location can be determined from the ratio of the two signal charges, we plot delay time vs. absorption location, as shown in figure 4.2.1. for the tantalum device.

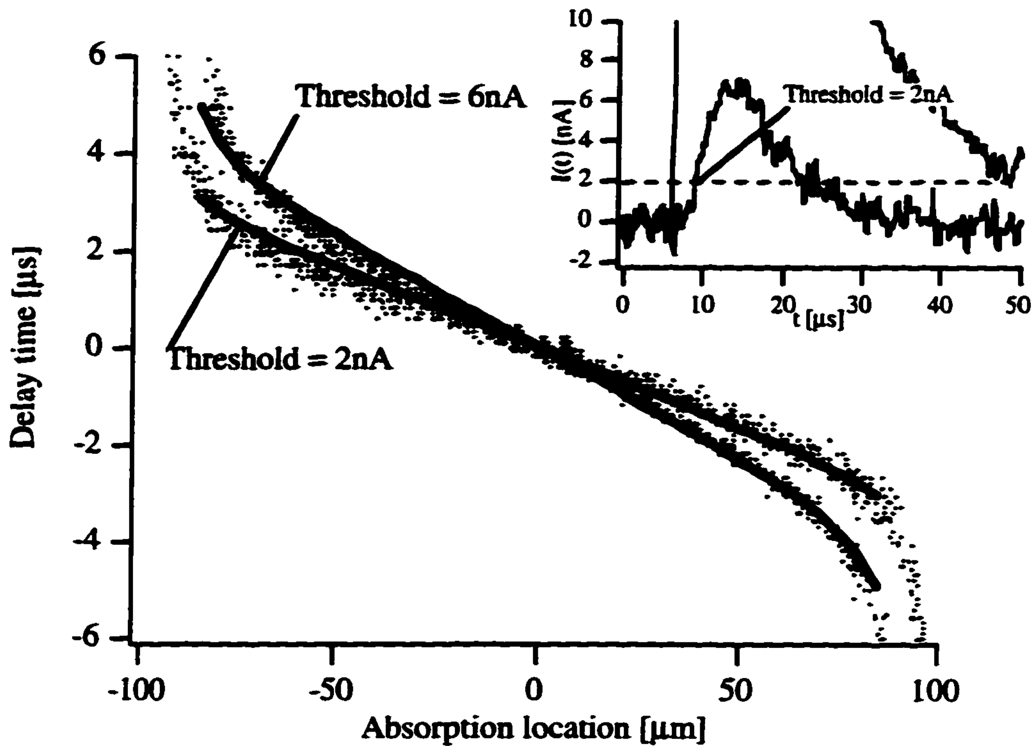

Figure 4.2.1.: Delay time measurements in tantalum device. The inset shows a typical set of current pulses from the edge of the absorber (08/07/96, T = 0.24K).

These data are compared to the delay times predicted from the simulations. All parameters in the simulation are constrained by the requirement that peak currents and charges of the simulated pulses must match the observations over the entire absorber. As expected, the delay times are a sensitive function of the diffusion constant in the absorber, assumed to be a single number, but do not depend strongly on other input parameters (such as τ_{trap}) to the simulation. They depend to some extent on the initial charge and the tunneling time, which directly affect the magnitude of the current, but which are constrained by the x-ray energy and the junction's normal state resistance.

The best fit to the data is obtained for D_{Ta} = 8 ± 2 cm^2/s (solid lines). The uncertainty in this number indicates that a simultaneous fit of delay times, peak currents and charges is no longer possible even if we remove all constraints on all other parameters. To ensure that the diffusion constant we extract does not depend on the somewhat arbitrarily chosen threshold level, we have analyzed the data for two different levels, 2 nA and 6 nA.

Both sets of delay time data in figure 4.2.1. can be fit with the same choice of diffusion constant. The measured value of the diffusion constant does not change with temperature between 0.24K and 0.34K.

We have performed the same time-of-flight measurement in the device in which the aluminum trap overlaps the entire tantalum absorber and the quasiparticles propagate in the lower gap aluminum (figure 4.2.2.). Quasiparticle diffusion is much faster in these devices, with best fit values $D_{Al} = 60 \pm 20$ cm^2/s (solid line). To show the resolution of this technique to quantify D, we have added predicted delay times for diffusion constants of 30 and 90 cm^2/s (dashed lines).

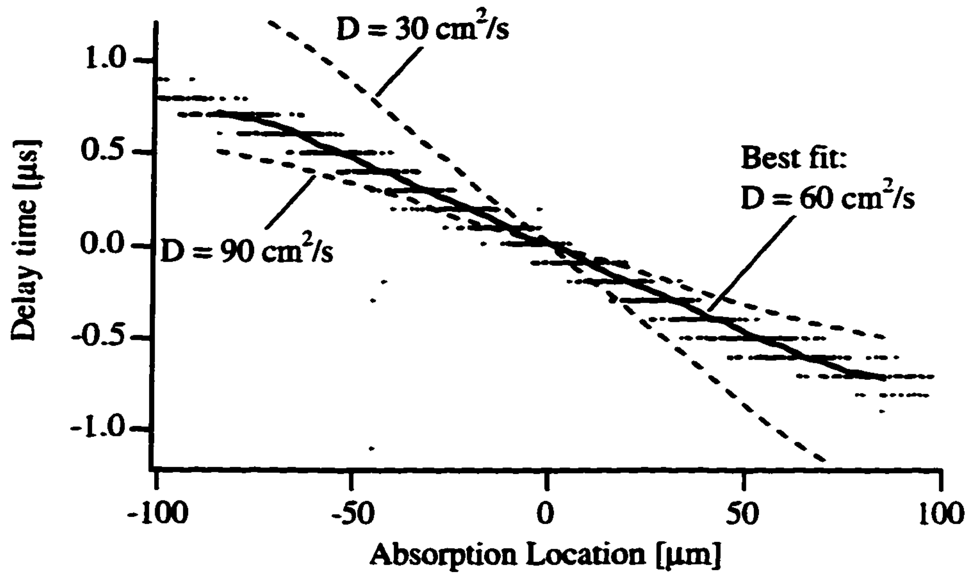

Figure 4.2.2.: Delay time measurements in aluminum (10/17/96, T = 0.24K)

We estimate the low temperature normal state diffusion constant from the Einstein equation

$$D_N = \frac{1}{\rho_N e^2 n(E_F)}, \qquad 4.2.1.$$

because it does not involve any free electron approximations, the normal state resistivity ρ_N can be measured directly, and the density of states at the Fermi surface $n(E_F)$ enters as the

only band-structure-dependent quantity. For a resistivity $\rho_N = 0.478 \pm 0.05$ μΩcm at 5 K and $n(E_F) = 7.1 \pm 0.32 \cdot 10^{22}$ $eV^{-1}cm^{-3}$ (see appendix A), we expect a normal state diffusion constant of $D_{N,Ta} = 180 \pm 20$ cm^2/s.

In the superconducting state, the diffusion constant D_{SC} is reduced because the quasiparticle dispersion relation exhibits a minimum at the Fermi energy where the density of states diverges - or equivalently, where the group velocity approaches zero. In thermal equilibrium, the reduction is given by [Narayanamurti, 1978]

$$D_{SC} = D_N \sqrt{\frac{2k_B T}{\pi \Delta}}. \qquad 4.2.2.$$

Under non-equilibrium conditions after x-ray absorption the degree of reduction depends on how close to the gap edge the quasiparticles are distributed as they diffuse through the absorber. This determines the instantaneous value of D for non-equilibrium conditions. We have simulated this relaxation by dividing the energy range between Δ and 3Δ into energy bins and iterating the quasiparticle density in the i-th energy bin N_{qp}^i according to the rate equations for phonon emission [Kaplan, 1976]. At each iteration we calculate an energy distribution and an average diffusion constant. Characteristic time scales for electron-phonon scattering from bin i to j are denoted by $\tau_{i \to j}$ and the net change in quasiparticle occupation number is determined by the difference between quasiparticles scattering out of bin i into lower energy bins and into bin i from higher energies.

$$\frac{\partial N_{qp}^i}{\partial t} = -\sum_{j<i} \frac{N_{qp}^i}{\tau_s^{i \to j}} + \sum_{j>i} \frac{N_{qp}^j}{\tau_s^{j \to i}}. \qquad 4.2.3.$$

Phonon reabsorption is neglected and thus the calculated value of D is a lower limit. We do not expect the result to change significantly if phonon reabsorption were included, because most phonons will escape into the substrate ($\tau_{esc} \approx 2$ ns) before being reabsorbed.

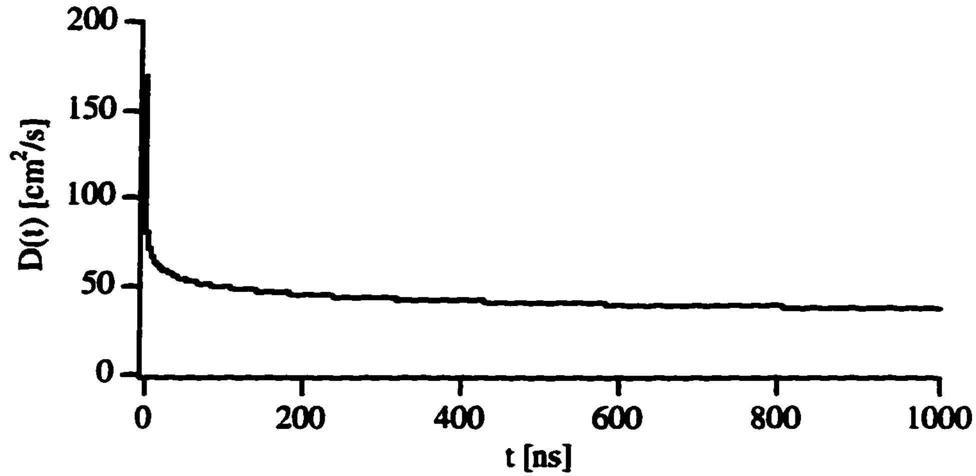

Figure 4.2.3.: Average non-equilibrium diffusion constant in tantalum

Figure 4.2.3. shows how the average diffusion constant changes over time for quasiparticles diffusing through the tantalum absorber. Phonon emission is initially very fast, causing the initial drop in D during the first 100 ns. But as quasiparticles scatter closer to the gap edge where the phase space for phonon emission decreases, the energy relaxation slows down and D does not decrease much below 40 cm^2/s. It is then appropriate to approximate D with a single constant despite the non-equilibrium nature of the process. The average quasiparticle energy after 1μs is about 1.02 Δ_{Ta}. The degree of reduction in D is insensitive to the particular choice of initial distribution in the simulation.

The relaxation in aluminum is slower because weaker electron-phonon coupling leads to longer scattering times. Even so, after 1μs the diffusion constant is reduced, in theory, to 42% of its normal state value and only changes slowly thereafter. The average quasiparticle energy at that time is about 27 μeV above the aluminum gap. The results of the simulation and the delay time measurements for tantalum and aluminum are summarized in the table below.

The low measured diffusion constant for aluminum and tantalum in our devices is surprising, particularly considering that the high residual resistance ratio and the normal state resistivity close to the bulk value indicate high quality films. This high quality makes

it unlikely that the slow diffusion can be explained with the normal state properties of the film. The low value of D cannot be explained with a sub-thermal quasiparticle distribution under non-equilibrium conditions, either, because our time dependent simulation shows that the quasiparticles achieve a distribution more energetic than thermal.

	Tantalum	Aluminum
Resistivity ρ_N at $T = 5$ K [$\mu\Omega$cm]	0.478 (RRR=30)	0.23 (RRR=13)
Density of states $n(E_F)$ [1/eVcm^2]	$7.1 \cdot 10^{22}$	$2.2 \cdot 10^{22}$
Normal state diffusivity D_N [cm^2/s]	180 ± 25	1250 ± 170
Non-equilibrium D_{SC} (simulation) [cm^2/s]	38 ± 4	530 ± 70
Thermal equilibrium D_{SC} at 0.25 K [cm^2/s]	25 ± 3	350 ± 50
Average quasiparticle energy after 1 μs	1.02 Δ_{Ta}	1.16 Δ_{Al}
Experiment D_{SC} [cm^2/s]	8 ± 2	60 ± 20

Table 4.2.1.: Diffusion in tantalum and aluminum

We believe the slow diffusion is related to small gap variations inside the absorber films, either at grain boundaries, absorber edges or intrinsic gap variations. Intrinsic gap anisotropies are related to the Fermi surface, the electron wave functions, the phonon spectrum and the electron-phonon matrix element, all of which are anisotropic. A few percent gap variations would be enough to restrict the charges to the valleys of the gap and confine them to the absorber for longer times, similar to the process of percolation. Tunneling experiments in high quality tantalum junctions indicate a gap anisotropy of 3% [Face, 1987]. Critical magnetic field measurements even suggest 12% anisotropy [Bostock, 1977]. For aluminum, gap anisotropy measurements with different techniques are scattered over a similar range [Bostock, 1977].

Slow diffusion limits the maximum absorber size in cases where the quasiparticle lifetime is finite. The limit on the maximum count rate is less important, because the x-ray flux from celestial sources is low. An empirical requirement for high resolution is $\alpha = L/\sqrt{(D\tau_{loss})} \leq 2$ [Kraus, 1993]. For quasiparticle lifetimes of order 30 μs presently observed in our devices (see chapter 4.5), this limits the maximum absorber length to $L \leq$ 300 μm. However, since neither the origin of the loss or slow diffusion is understood at this time, and theoretical predictions for both are significantly more favorable, future research with different quality absorber films may well achieve better parameters and consequently allow larger absorber sizes.

An elegant solution to speed up the diffusion would be to use a very thin aluminum trap over the tantalum absorber, such that the proximity effect would raise its gap about half way between the tantalum gap and the gap of bulk aluminum. One could then exploit the high absorption efficiency of tantalum, fast diffusion in aluminum while still trapping effectively from the proximity enhanced aluminum into the bulk aluminum to the side of the absorber.

4.3. Quasiparticle Trapping

Trapping occurs when charges in the lower gap region scatter inelastically below the gap energy of the higher gap region. It determines how effectively charges are separately collected into the two detector junctions. The faster the trapping, the more effective the charge separation.

Short Trap Device

We infer characteristic time scales for trapping from the relative signal heights for absorption events close to the aluminum trap. We neglect the 10 μm region where the trap

overlaps the absorber, because the model assumption that the areas of quasiparticle generation and trapping are separate is no longer valid. Figure 4.3.1. shows the charge fraction collected from x-ray events at a 1 μm distance from the traps for different degrees of trapping. It only depends on the trapping time and -to a much weaker extent- on the diffusivity in the absorber, which is constrained by the delay time measurements ($D_{Ta} = 8\ cm^2/s$).

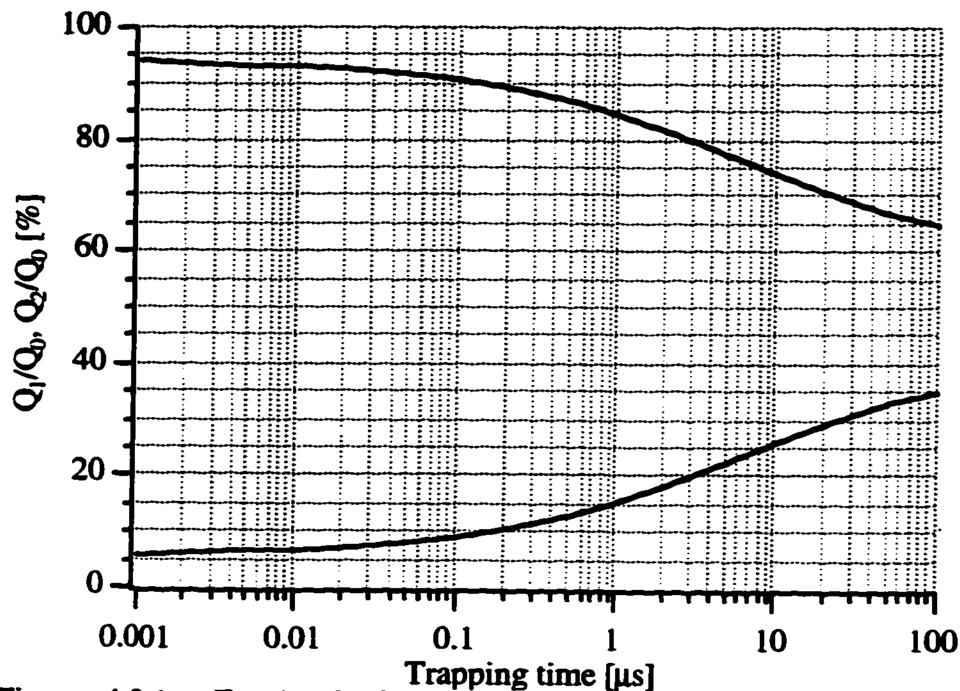

Figure 4.3.1.: Fractional charge collection in the two junctions for absorption events 11 μm from the edge of the absorber without qp loss.

As the trapping time increases on the time scales for diffusion, either because of a dirty interface or slow inelastic scattering, the charge separation becomes less effective and the fraction collected in the more distant junction increases. For infinitely fast trapping, the charge collected in that junction approaches an ideal value of 11μm/200μm = 5.5%.

These events correspond to the ends of the main sequence in the scatter plot in figure 4.3.2., just before the total charge discontinuously increases for x-rays absorbed in the overlap region. Here 6 ± 1% of the total charge is collected in the more distant junction. This sets an upper limit of 10 ns on the trapping time. It also indicates a high quasiparticle transmissivity of the tantalum-aluminum interface. Ion beam cleaning the

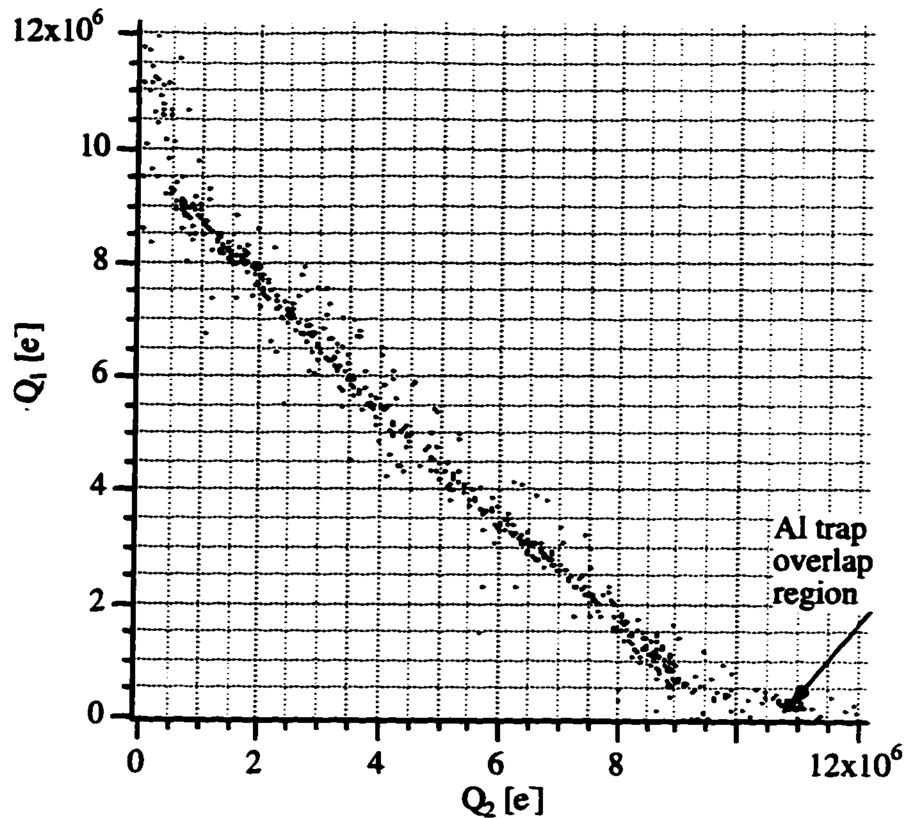

Figure 4.3.2.: Charge output of the tantalum device (12/07/95, T =0.30K)

tantalum surface prior to deposition of the aluminum trilayer is thus seen to successfully remove impurities or oxides that may have been introduced when patterning the absorber.

Long Trap Device

Trapping in the aluminum device is significantly slower, because the gap difference between the proximity enhanced aluminum on top of the absorber and the bulk aluminum to the side is small. This results in a less effective separation of charges and consequently a finite minimum charge from both detectors even for events on the opposite side of the absorber (figure 4.3.3.).

A quantitative measure of the trapping time is somewhat more difficult for this device, because the charge ratio Q_1/Q_2 is affected by the relative time scales for diffusion,

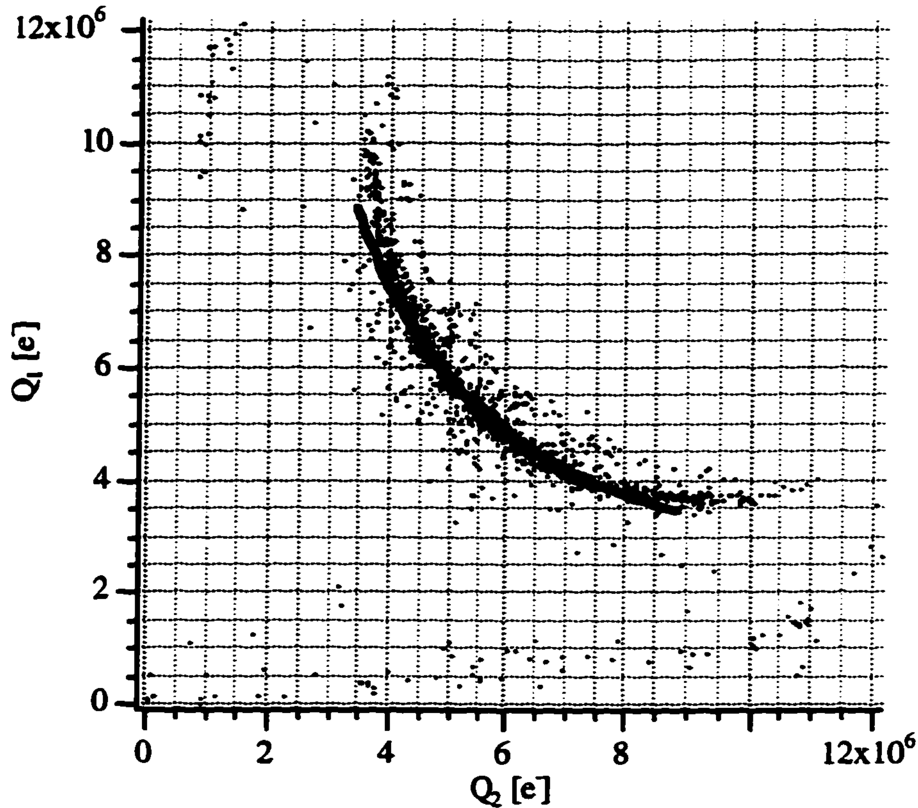

Figure 4.3.3.: Charge output of the aluminum device (11/20/95, T = 0.3K)

trapping and loss. However, all fits yield trapping times of the same magnitude as $\tau_{diff} = L^2/D_{Al} = 6.6\ \mu s$, to first order independent of the quasiparticle lifetime. This allows an estimate of the minimum gap energy in the overlap region, because the scattering time in the bulk aluminum at that energy must be of order microseconds. The best fit is obtained for a trapping time of 8 μs (solid line). There is a small discrepancy between fit and data at the end of the main sequence corresponding to events close to the edge of the absorber. This may be due to the hotspot extending into the trap region during relaxation and producing disproportionately more charge in that junction.

Proximity Effect

An exact solution of the gap profile involves self-consistent solution of the Usadel equations [Usadel, 1970] in the vicinity of the tantalum-aluminum interface. It has been

calculated for two dissimilar superconductors, but only in the limit of a thin lower gap film ($d \ll \xi$), such that the gap in this film can be assumed constant [Golubov, 1995]. For our devices, these calculations would predict a strong enhancement of the aluminum gap and consequently fast trapping even for the long trap device. This is not observed, indicating a coherence length ξ shorter or at most comparable to the film thickness d. The McMillan model [McMillan, 1968] only holds for an interface with low transmissivity and is not applicable to our devices.

We describe the gap structure within the de Gennes model [de Gennes, 1964], although it is strictly valid only close to the critical temperature of the layered system, such that the energy gap is small and can be treated in perturbation theory. Its use at lower temperature appears justified, as it predicts trapping times consistent with our experimental observations. In the dirty limit the energy gap far away from the interface decays exponentially over a characteristic coherence length

$$\xi \approx \sqrt{\frac{\hbar D_N}{2\pi k_B T}}, \qquad 4.3.1.$$

where D_N is the normal state diffusivity of the respective layer. We assume a transition temperature T_C of the layered system close to the bulk critical temperature of the thick tantalum film. Using the measured values $D_{Ta} = 8$ cm^2/s and $D_{Al} = 60$ cm^2/s and removing the 80% and 60% reduction in D in the superconducting state for tantalum and aluminum, respectively, the coherence lengths are $\xi_{Ta} = 330$ Å and $\xi_{Al} = 640$ Å. Figure 4.3.4. shows the predicted gap structure in vertical direction across the bilayer. The low diffusion constant and consequently short coherence lengths cause the aluminum gap to almost relax to its bulk value of 170 μeV over the 1500Å thickness of the film.

The average gap in the overlap region of 570 μeV is about 20% below the bulk value of Δ in tantalum. The average increase in detected charge is only 10% for events

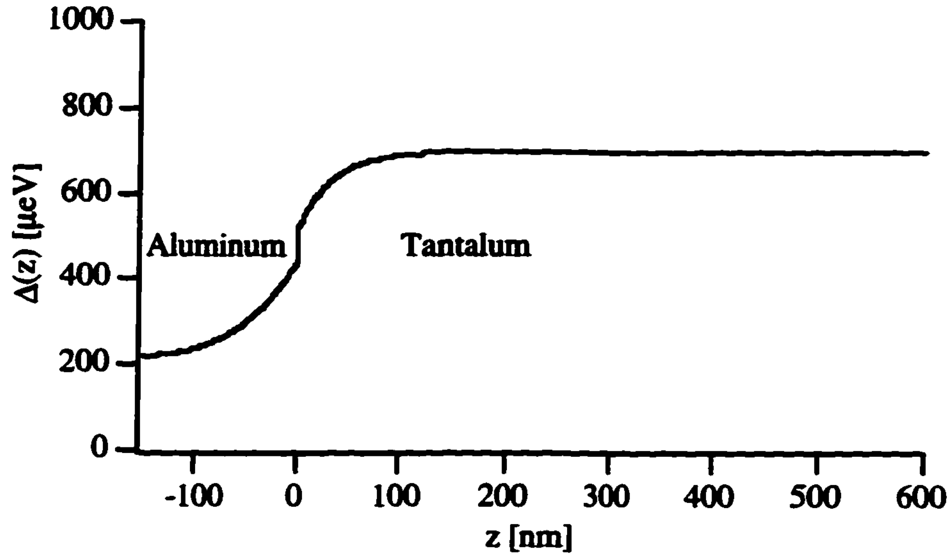

Figure 4.3.4.: Gap profile in the tantalum-aluminum bilayer according to the de Gennes model

from the overlap region (figure 4.3.2.). Thus, the hotspot most likely relaxes its energy preferentially in the large gap tantalum film, where the scattering times are faster.

We now address the question where the trapping takes place. After 1ns, the quasiparticles in the overlap region are homogeneously distributed in z direction and only those that have diffused to the lower gap Al region can be trapped by inelastic scattering. The total trapping rate can be calculated as the sum over the contribution of the various locations according to [Golubov, 1994]

$$\frac{1}{\tau_{trap}} = \frac{1}{d}\int_0^d \frac{dz}{\tau_{trap}(\Delta_{Ta} / \Delta(z))}. \qquad 4.3.2.$$

Here $\tau_{trap}(\Delta_{Ta}/\Delta(z))$ is the inelastic scattering time for quasiparticles injected at energy Δ_{Ta} = 700 μeV into a region with local gap value $\Delta(z)$ and the integral is evaluated over the entire thickness d of the bilayer. Assuming that the proximity effect does not change the electron-phonon coupling, the total trapping time in the overlap region is 0.15 μs for the gap structure shown above. This is longer than the upper limit of 10 ns imposed by the

data, thus indicating that most of the trapping takes place in the bulk aluminum film to the side of the absorber. The inelastic scattering time of 6 ns for quasiparticles in bulk aluminum at energy Δ_{Ta} agrees much better with the observations.

One can also infer the location of the trapping in the tantalum device directly from the Q_1 vs. Q_2 plot (figure 4.3.2.). If fast trapping occurred inside the overlap region, the main sequence of events would extend all the way to the axes, because quasiparticles generated close to the overlap region would be trapped immediately and not be able to produce a finite signal in the opposite detector.

A trapping time of 0.15 μs in the Ta-Al bilayer is long enough to ensure that quasiparticles scatter into the proximity enhanced aluminum in the devices where the trap overlaps the entire absorber. Quasiparticles at the gap edge are trapped into the bulk aluminum after 30 μs for the gap structure shown in figure 4.3.4. However, most quasiparticles will not relax completely to the gap edge end the average trapping time will be shorter. Since the scattering time is a very sensitive function of energy, the uncertainties involved in using the de Gennes model prevent reliable quantitative predictions for the trapping time. Nevertheless, a minimum gap not much above the gap of bulk aluminum is required to explain the observed trapping times of order microseconds in the long trap device. The gap structure shown in figure 4.3.4. is consistent with observed trapping times in both types of devices we have examined.

Quasiparticle Multiplication upon Trapping

In the short trap device, most quasiparticles are trapped in a region where the energy gap is less than one third of the quasiparticle energy. They scatter preferentially into low energy states where the final electron and phonon densities of state are large. The relaxation phonons can then either break additional Cooper pairs or escape into the substrate. The characteristic time for escape is given by $\tau_{esc} = 4d_{trap}/\alpha c_{ph}$ [Gray, 1971], where $c_{ph} = 4.10^3$ m/s , d_{trap} is the thickness of the trap and $\alpha_{Al\text{-}SiO2} = 0.7$ is the phonon

transmission coefficient into the substrate [Kaplan, 1979]. We have simulated multiplication upon trapping using the same programs written to simulate the hotspot relaxation, except that now all quasiparticles are injected into the aluminum trap at the gap energy of tantalum. For an escape time of 0.2 ± 0.1 ns in our devices (d_{trap} = 1500 Å), we find and increase in charge by a factor 1.6 ± 0.2 (figure 4.3.5.).

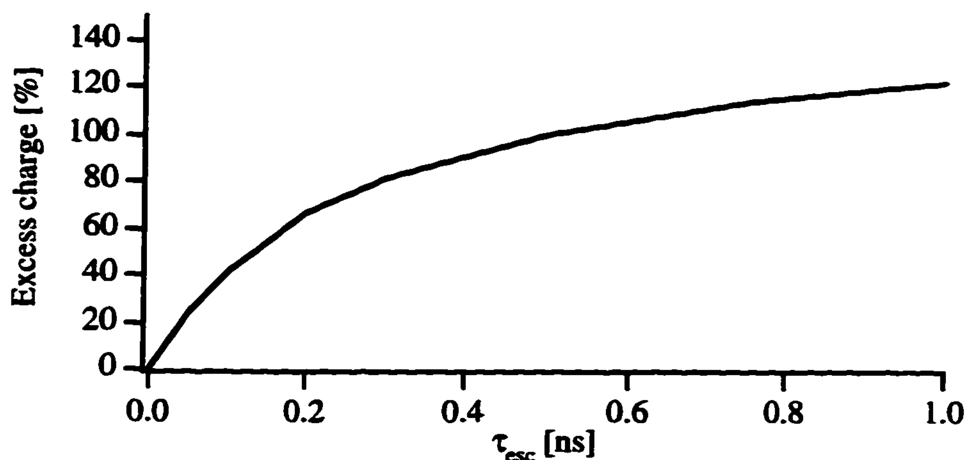

Figure 4.3.5.: Quasiparticle multiplication upon trapping. For long escape times, the multiplication factor approaches 155%.

Fluctuations in this excess charge add statistical noise. Correlations in this multiplication process will be comparable to the correlations in the initial hotspot and result in a Fano factor F ≈ 0.2. For our present devices we expect about 2 eV excess noise at 6 keV due to trapping. If this ever becomes a concern, one can accelerate the phonon escape into the substrate by using a thinner film.

Summary

In summary, trapping in the technologically more relevant short trap device is fast (≈ 10 ns), indicating highly transmissive tantalum-aluminum interfaces. It occurs in the bulk aluminum layer to the side of the absorber and results in a 60% increase in charge due to pair breaking by relaxation phonons.

4.4. Quasiparticle Tunneling

Tunneling is the process through which excess quasiparticles are detected. As discussed in chapter 2, there are four different contributions to the total tunneling current (figure 4.4.1). Quasiparticles in the trap can tunnel directly into the counterelectrode (process A). Quasiparticles in the counterelectrode can break Cooper pairs in the trap to form another pair in the counterelectrode (process B). This transfers a charge in the same direction as the direct process and produces another quasiparticle at an energy above eV_{bias} in the trap [Gray, 1978]. The inverse processes (C and D) are only possible for those quasiparticles that have not scattered below eV_{bias} above the gap in their respective electrodes [cf. Gutsche, 1996]. Energy conservation forbids these processes for lower energy quasiparticles, as there are no final single particle states available below the gap.

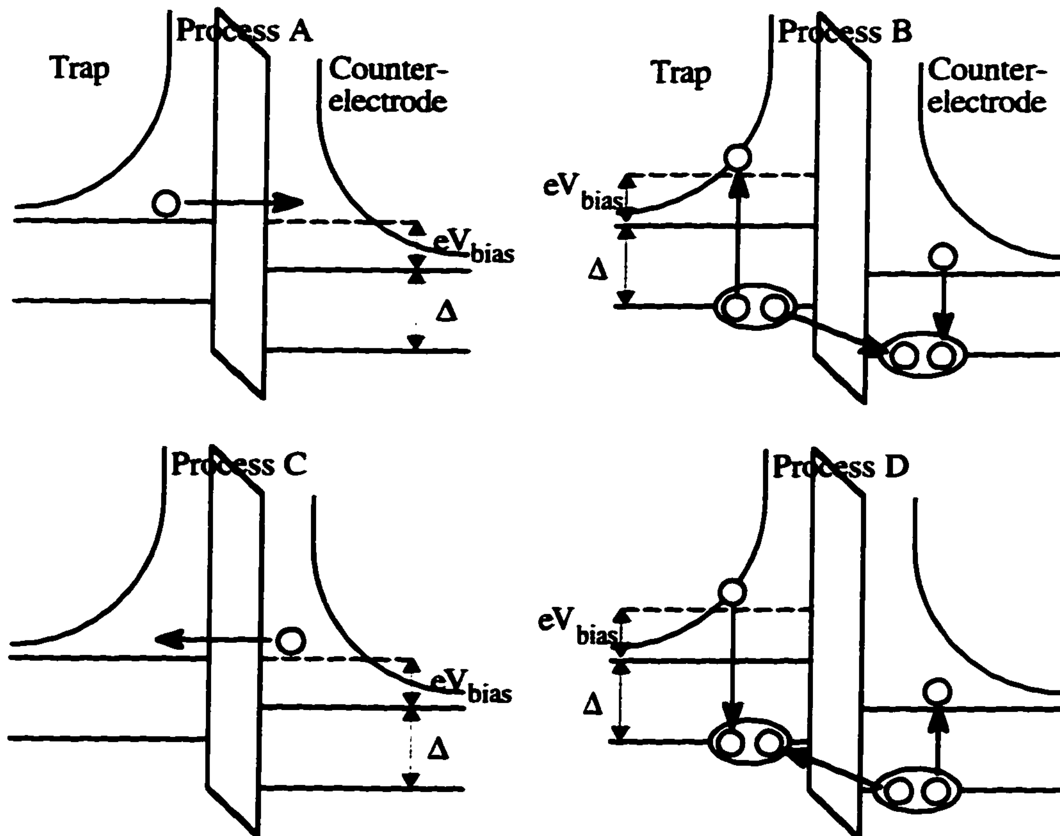

Figure 4.4.1: Energy diagram for the various tunneling processes.

The total current and charge thus depend on the relative magnitude of the contributions from the four processes. If the quasiparticles remain above eV_{bias} and do not diffuse away from the barrier, the currents in positive direction (processes A and B) are to first order canceled by process currents in the negative direction (processes C and D). The negative current contributions are, in fact, even somewhat more likely, because the density of states for the final quasiparticle is larger in these processes. On the other hand, quasiparticles below eV_{bias} can only contribute to the current in positive direction. The peak currents and the total charge thus depend on whether the quasiparticles scatter below eV_{bias} before they tunnel or diffuse out of the counterelectrode. Characteristic time scales for tunneling are of order 1 μs, as are characteristic scattering times for typical bias voltages.

For an estimate of the quasiparticle distribution in the junction electrodes we have simulated the relaxation of quasiparticles injected into an aluminum electrode at an energy $4\Delta_{Al}$, which corresponds to the gap energy of tantalum (figure 4.4.2.). Within a half a microsecond, quasiparticles relax within 100 μV of the gap energy, at which point inelastic scattering slows down significantly. In particular, not all quasiparticles relax below typical bias voltages (typically ≈ 70 μV) before tunneling. These quasiparticles transfer charge in

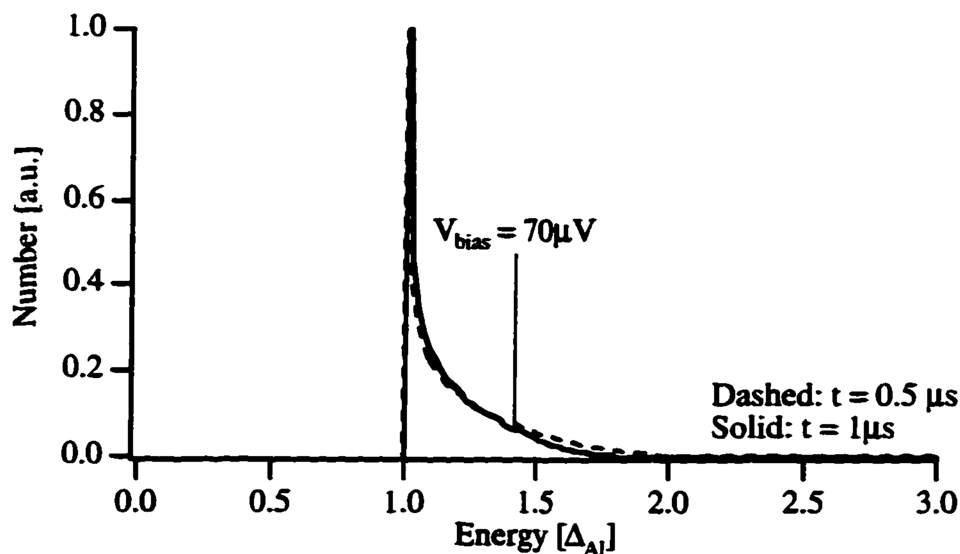

Figure 4.4.2.: Non-equilibrium quasiparticle distribution in aluminum.

the opposite direction to the bias and reduce peak currents and total detected charge. This effect will be more pronounced for lower bias voltages, when a larger fraction of the quasiparticles resides at an energy above eV_{bias}.

The bias dependence of the observed signals and the corresponding fits from the model simulation are displayed in figure 4.4.3. Both peak currents and total collected charge can be explained well over the entire length of the absorber for the same set of parameters, many of which are constrained through independent measurements (D_{Ta} = 8.5 cm^2/s, constrained by delay time data; $Q_0 = 8 \cdot 10^6$ e^-, constrained by relaxation simulation and multiplication upon trapping; $\tau_{loss,Ta}$ = 18 μs; τ_{out} = 5 μs).

The quantitative description of the bias dependence allows us to estimate the charge output as a function of bias voltage (figure 4.4.4). At higher bias, the charge output increases because a larger fraction of the quasiparticles scatter below eV_{bias} such that only forward tunneling processes are allowed. The charge output eventually levels off at voltages where the scattering times are sufficiently fast such that almost all quasiparticles scatter below eV_{bias} before they tunnel.

More importantly, the variations of the charge with bias decrease at higher voltage. Under present operating conditions, a 1 μV bias voltage would correspond to 40 eV excess noise. Observed bias voltage fluctuations during typical halh hour runs are of that order and constitute one of the dominant noise sources in our system at present.

For large collected charge and reduced fluctuations, the highest possible bias voltage is desirable. However, in the present devices Fiske modes at 100 μV and 140 μV create excess noise for bias voltages above 80 μV and prohibit biasing in that region. Furthermore, since the subgap current increases and the dynamic resistance of the device decreases at higher bias, electronic noise will dominate the device resolution in that region. We will address these issues in future devices with tunnel junctions that will be smaller by about a factor of 4 in direction perpendicular to the applied magnetic field. This increases

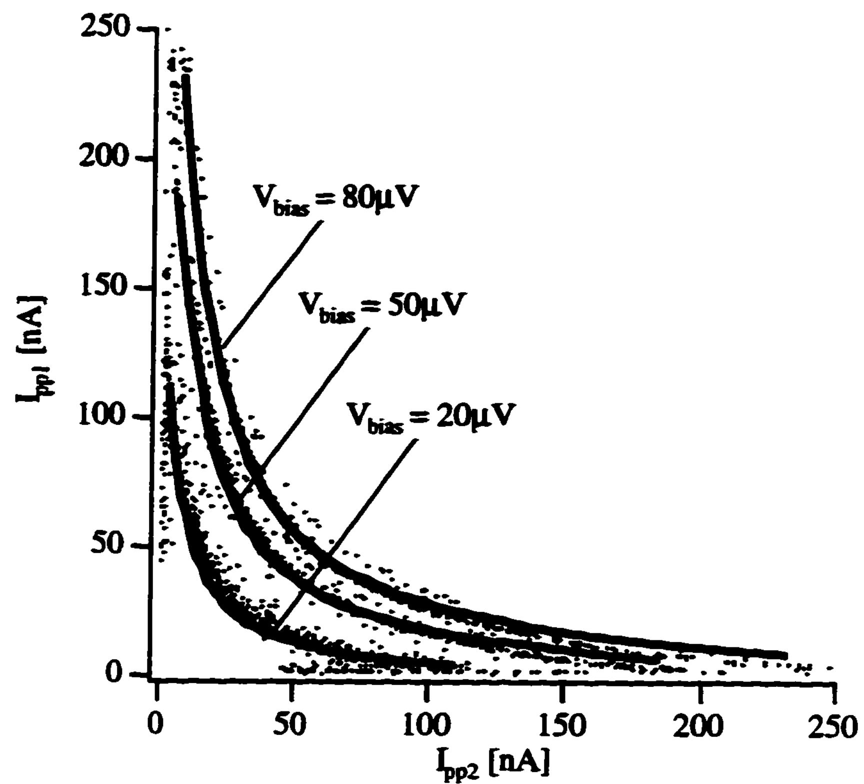

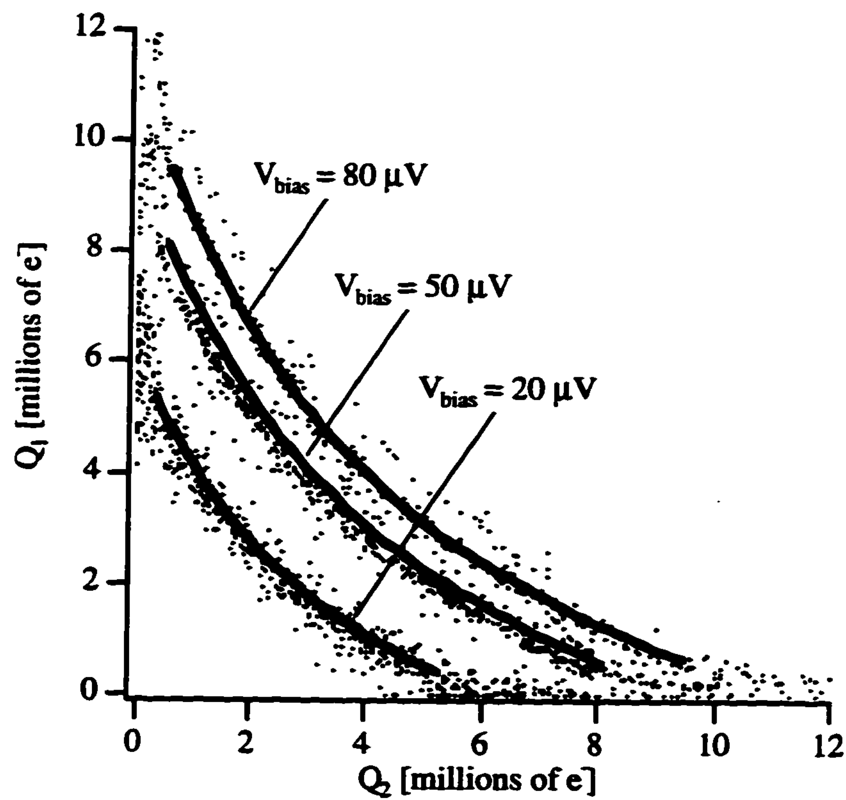

Figure 4.4.3.: Bias dependence of peak current and total charge (01/20/97, T = 0.24K

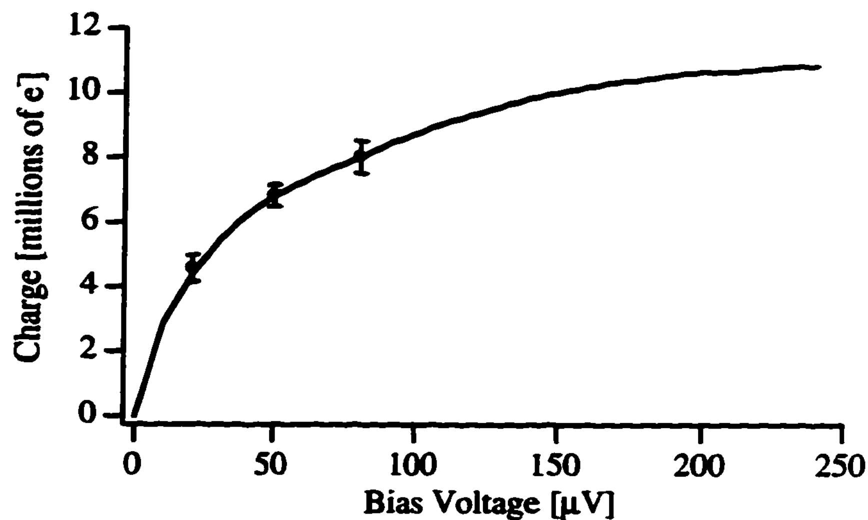

Figure 4.4.4.: Charge output from the center of the absorber

the voltage of the lowest Fiske mode and allows stable low noise biasing at higher voltages. It will also decrease the thermal subgap current and increase the dynamic resistance for tunneling barriers with the same transmissivity.

To summarize, the charge output of our devices displays a strong bias dependence because high energy quasiparticles can transfer charge in the opposite direction to the applied bias. Bias voltage fluctuations of 1 μV result in excess noise of order 40 eV under typical operating conditions. Future devices will address this issue either with higher resistance barriers or with smaller junctions to allow biasing at a higher voltage.

4.5. Quasiparticle Recombination

Efficient charge collection and potential scaling of device sizes to larger absorber areas require quasiparticle lifetimes to be long compared to all other processes. Also, local variations in the quasiparticle lifetime produce variations in the total detected charge for uniform illumination of the device, thereby degrading the device resolution. The spatial

resolution of the double junction detectors enables us to study quasiparticle loss processes and identify their location within the detector.

Quasiparticle Loss in the Absorber

As quasiparticles diffuse through the tantalum absorber, there is a finite probability for them to recombine, thereby reducing the total detected charge. This effect will be more pronounced for quasiparticles generated in the center of the absorber, because they have to diffuse over a longer average distance before being detected in one of the junctions. Quasiparticle loss in the absorber therefore manifests itself as curvature in the Q_1 vs. Q_2 scatter plot. The degree of curvature depends on the relative time scales for diffusion and loss. Quasiparticle loss can either be uniform throughout the absorber, in which case equation 2.2.4 provides an analytic expression for the expected charge output, or there can be localized quasiparticle loss sites that would cause a deviation from that expression. Of course, our detectors only provide one-dimensional resolution along the long direction of the absorber, and the curvature of the scatter plot is not directly sensitive to variations in quasiparticle loss in the other directions. Quasiparticle loss in the junction electrodes can be distinguished from losses in the absorber, as it will only affect the magnitude of the collected charge, but it will not change the curvature of the scatter plot.

Figure 4.5.1. displays the charge output of the detectors at three different operating temperatures between 0.24 K and 0.34 K and a magnetic field of 13 Gauss. One can fit the data well assuming a uniform effective quasiparticle lifetime of $\tau_{loss} = 31\ \mu s$ in the absorber and an effective time for outdiffusion $\tau_{out} = 7\mu s$. One should keep in mind that the curvature of the scatter plot actually depends on the *ratio* of the time scales for diffusion $\tau_{diff} = L^2/D_{Ta}$ and loss. A finite lifetime only matters if the time it takes the quasiparticles to diffuse into the traps is of comparable magnitude. However, since the value of the diffusion constant is constrained independently through delay time measurements as D_{Ta} =

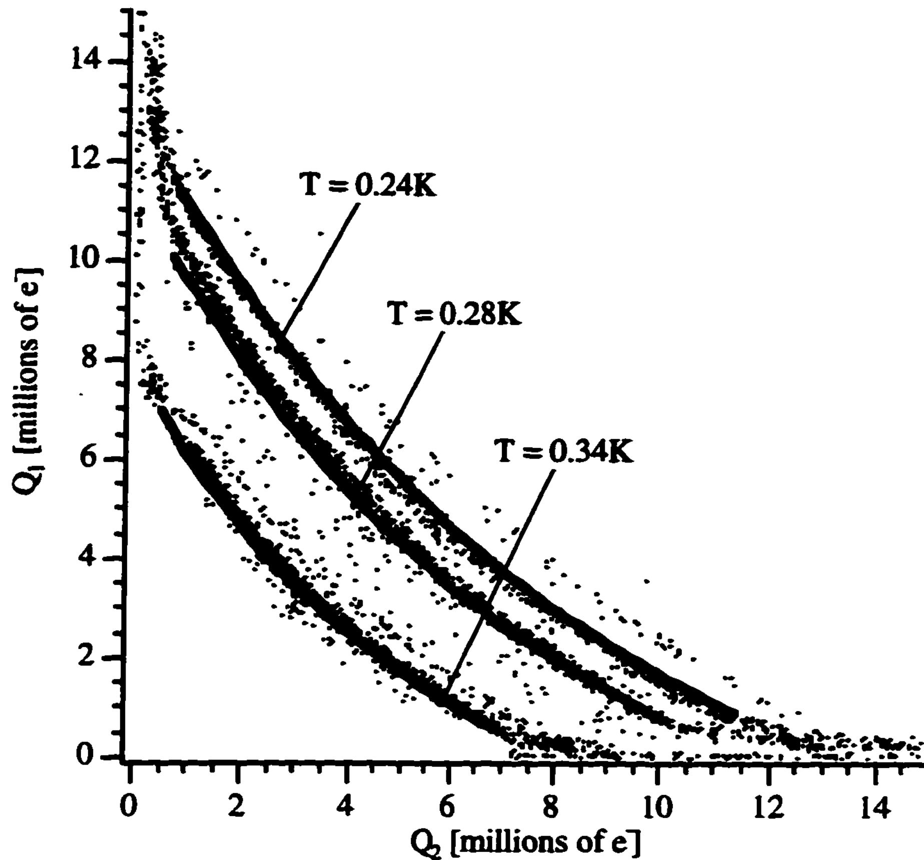

Figure 4.5.1.: Charge output at different operating temperatures. Model fits (solid lines) assume $\tau_{loss} = 31\mu s$ and $\tau_{out} = 7\mu s$. (08/07/96)

8 cm^2/s, the quasiparticle lifetime is the only parameter adjusted to model the degree of curvature in the figure 4.5.1.

The initial charge in the above model fits is $8 \cdot 10^6$ electrons. It is experimentally determined by matching the observed peak currents (figure 4.5.2). This number corresponds to $4.3 \cdot 10^6$ electrons created in the initial energy relaxation process (cf. chapter 4.1.), and includes a charge multiplication factor of 1.86 upon trapping. This factor of 1.86 compares favorably to the expected value of 1.6 predicted in section 4.3.

The curvature in the scatter plots of Q_1 vs. Q_2 is constant for all three sets of data, confirming that thermal recombination is negligible in the absorber in the range of typical operating temperatures between 0.24 K and 0.34 K. This is expected, since there are effectively no thermal quasiparticles excited in the tantalum film at these temperatures. The

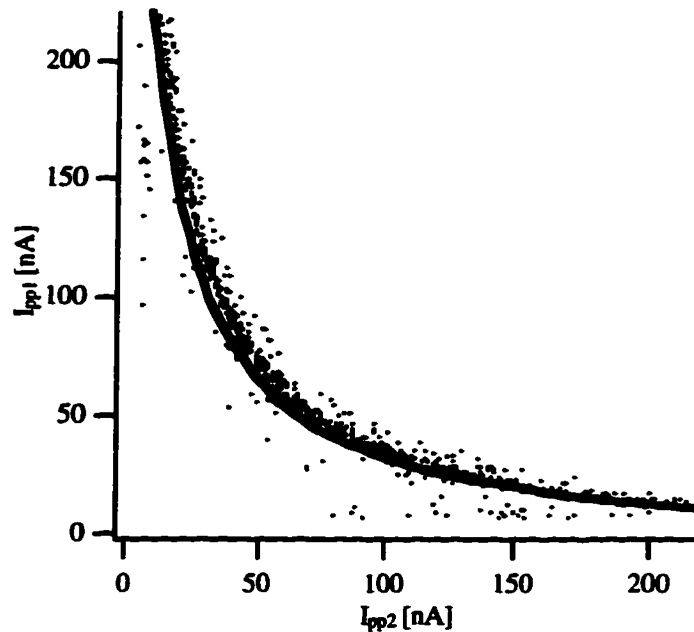

Figure 4.5.2.: Peak currents at T = 0.24K. Model fit is identical with the one used to explain the charge collection in figure 4.5.2.

quasiparticle lifetime does not change, either, when the magnetic field is increased up to a maximum value of 40 Gauss. Trapped magnetic flux due to the applied magnetic field that drives certain regions of the absorber film normal is therefore unlikely to explain the finite quasiparticle lifetime. If self-recombination among the excess quasiparticles were responsible for the observed quasiparticle loss, the effective lifetime for the higher energy K_β line would be reduced. To first order, this reduction would be about 10% because of the 10% higher quasiparticle density and would result in a 1.5% non-linearity between the K_α and the K_β line. This is not observed, despite a 1% energy resolution of our devices (cf. chapter 5). Furthermore, the effective lifetime due to self recombination in our films should be several microseconds if the enhancement due to phonon trapping is taken into account [Gaidis, 1994], much above the values measured in the experiment.

There are several possible explanations for the observed quasiparticle loss. Magnetic flux could be frozen in during cooldown when the tantalum film goes through the superconducting transition, in particular since we do not use any magnetic shielding. This

effect might be present, but not dominant, because the effective lifetime is found to lie consistently between 20 μs and 35 μs in different runs over a one year time scale. This variation is within the experimental accuracy with which we can infer the quasiparticle lifetime. A slow degradation of the tantalum film appears unlikely, because there is no uniform trend in the observed life time variations. This issue will be tested with a new set of devices in the near future. Another potential loss mechanism is trapping at reduced energy gap regions along the edges of the film. This loss mechanism has been observed in Nb/Al and Ta/Al devices [Gijsbertsen, 1995; Martin, 1996; Verhoeve, 1997] and may be due to mechanical damage and a consequently reduced order parameter. The losses in our films might also have been induced by magnetic impurities from the $FeCl_3$ wet etch of the tantalum film. We might therefore replace our wet etch by a reactive ion etch or use non-magnetic etchant solutions.

In figure 4.5.2. we again plot the unfiltered 0.24K data, this time as total collected charge vs. absorption location. One can see that the overall magnitude of the charge is decreased for absorption events in the center due to the finite quasiparticle lifetime as discussed above. In addition, the charge *fluctuations* increase in the center of the absorber.

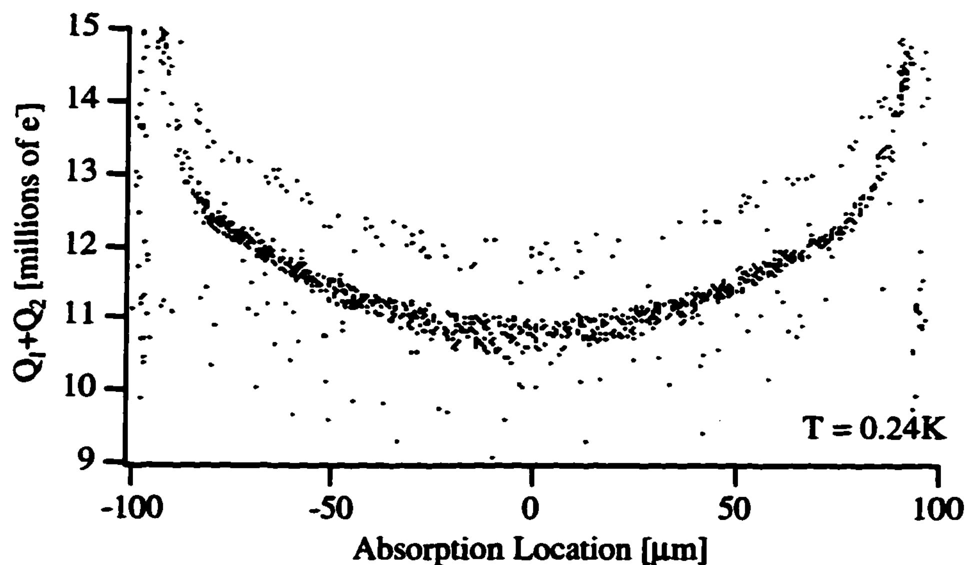

Figure 4.5.3.: Total collected charge (08/07/96)

This is evidence for another source of quasiparticle loss. In the center of the absorber the niobium strip contacts the absorber. It makes electrical contact to the absorber to bias the junctions, and niobium with the large energy gap is used to keep quasiparticles from diffusing out into the leads. However, niobium forms metallic suboxides that serve as unwanted trapping sites [Halbritter, 1987]. We believe that the excess broadening in the center of the absorber is due to different degrees of quasiparticle loss at the niobium contact depending on how far from the contact the x-ray has been absorbed.

Quasiparticle Loss in the Detector Junctions

The change of detected charge with temperature is due to recombination with the thermal quasiparticle background in the aluminum junction (Note $k_BT<<\Delta_{Al}<<\Delta_{Ta}$). We determine an effective quasiparticle lifetime of 31 μs in the absorber and an effective outdiffusion time to explain the total detected charge at 0.24K. Then the observed temperature variations can be accounted for in the model simulation as being due to the temperature. This allows us to estimate of the charge if the operating temperature were further reduced and allows an estimate of the resolution broadening due to temperature fluctuations in the course of a run.

Figure 4.5.4. displays the temperature dependence of the charge output from the center of the device. The charge levels off below 0.25K where $\tau_{rec}>>\tau_{out}$ and $\tau_{rec}>>\tau_{tun}$. It approaches a limiting low temperature value of 11.1 million electrons for this device with an effective quasiparticle lifetime of 31 μs in the absorber. If recombination in the absorber were negligible, the total charge would increase to 13.6 million electrons.) Despite the finite quasiparticle lifetime and the slow quasiparticle diffusion, the charge collection is still quite efficient. If the device length were scaled up to 1mm, the total charge would still exceed 0.9 million electrons over the entire absorber length at the 0.24K base temperature of our dewar.

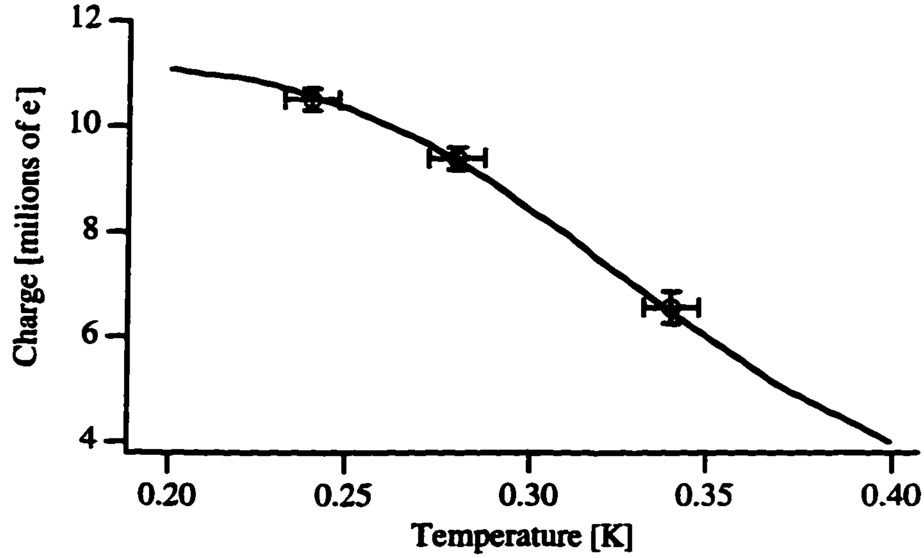

Figure 4.5.4.: Charge output Q_1+Q_2 from the center of the device. The data are taken from figure 4.5.1. and the solid line represents the model prediction.

Between 0.24 K and 0.3 K, the charge variations increase from 0.2 % to 0.6 % per mK. This corresponds to a resolution broadening of 12 eV to 36 eV per millikelvin degree of temperature fluctuation. From the variations of the thermal subgap current, we can infer a temperature stability of 0.1 mK in the course of a half hour run. Temperature fluctuations are therefore not expected to contribute to the resolution broadening.

Chapter 5: Device Performance

In this chapter we will outline under which conditions we have obtained optimum device performance with our present setup. X-ray spectra are presented and the limiting factors to the resolution are discussed.

5.1. Substrate Events

When illuminating the sample uniformly, the vast majority of x-rays are absorbed in the substrate. We would like to get a qualitative understanding how these events affect the detector performance.

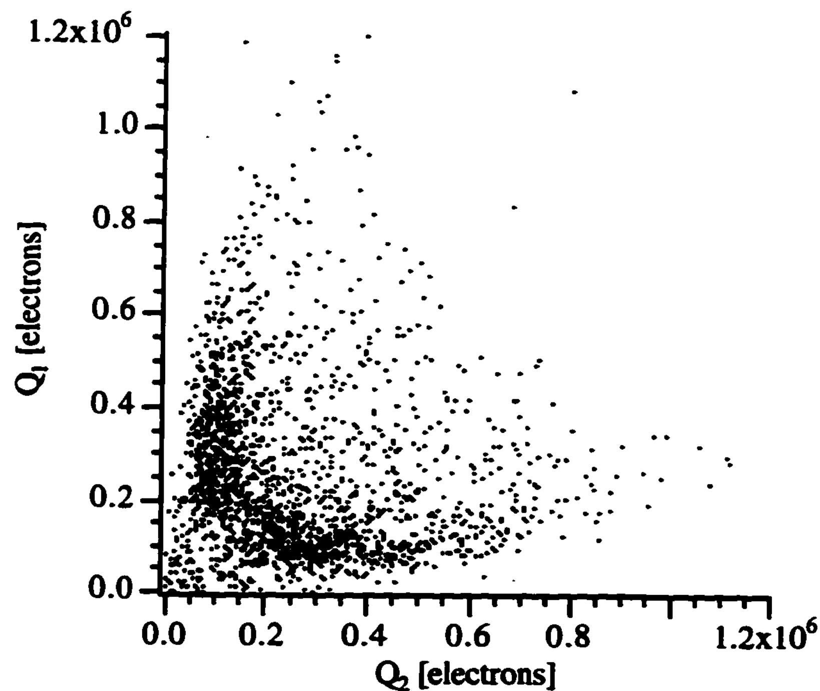

Figure 5.1.1.: Charge collection from substrate events (11/20/97, T = 0.3K)

After the initial relaxation process in the silicon substrate, the x-ray energy is converted into phonons. They can propagate towards the device and cause a signal by breaking Cooper pairs in the detector, since the Debye energy in silicon (54 meV) exceeds the gap energy of tantalum (1.4 meV) and aluminum (0.34 meV). Anharmonic phonon decay is slow in the single crystal silicon substrate, and the presence of substrate events shows that the amorphous oxide layer on the surface does not efficiently downconvert phonons below the superconducting gap energy of tantalum and aluminum.

Figure 5.1.1. shows the magnitude of such signals from substrate events. We will outline how to estimate the absorption location of substrate events in order to quantify how much charge is collected from substrate events at a certain distance from one of the detector junctions. For illustration consider figure 5.1.2.:

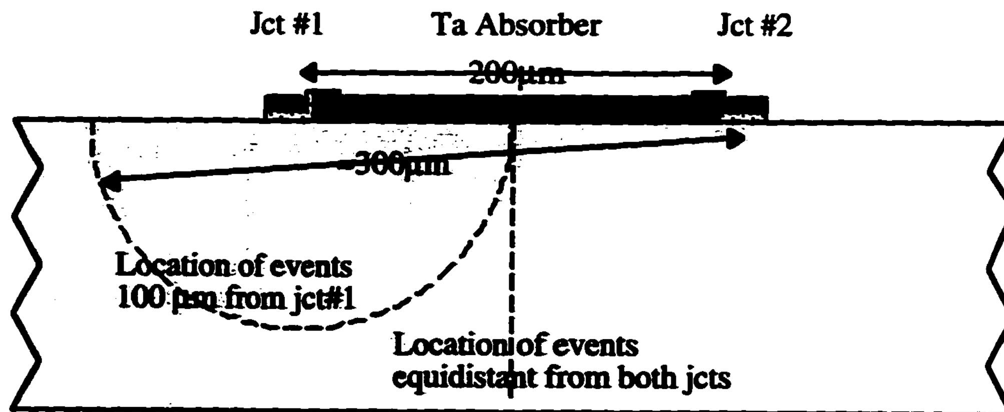

Figure 5.1.2.: Device cross section (incl. substrate) to visualize distances from the detector junctions.

The maximum signals from the substrate produce around $1.2 \cdot 10^6$ e^- in one and $0.3 \cdot 10^6$ e^- in the other junction. They correspond to an absorption location directly underneath one junction, i.e. next to that and 200 µm away from the other junction. Signals for which $Q_1 = Q_2$ indicate an absorption event equally far from both junctions. Events for which the charges are equal and maximum originate right under the center of the absorber. That corresponds to a distance of 100 µm and a collected charge of about

$0.6 \cdot 10^6 e^-$ When an event is 100 μm away from one junction, it can be at most 300 μm away from the other junction (figure 5.1.2.). With one junction recording $0.6 \cdot 10^6$ e⁻, the minimum signal in the other junction is about $0.1 \cdot 10^6$ e⁻. The values for the intermediate distances are estimated similarly.

It is thus possible to determine the impact of a substrate event at a certain distance from a junction (figure 5.1.3.). All numbers should be taken as rough qualitative estimates, as indicated by the large estimated errors. We can extrapolate that curve and find that substrate events as far as 700 μm away from a junction still generate enough charge to add more than 10^4 electrons to an absorber event, if both events overlap in time.

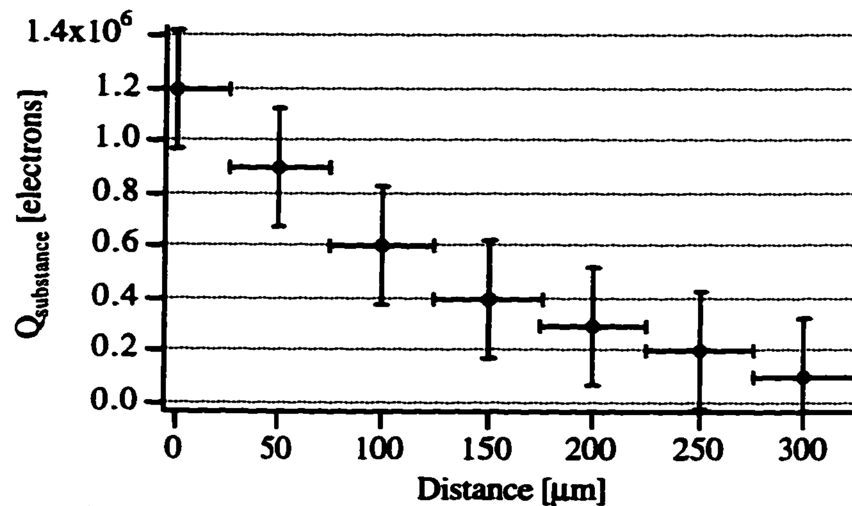

Figure 5.1.3.: Charge collected in one junction for substrate events at a certain distance

This imposes constraints on the maximum possible count rate. For example, a 30 mCi x-ray source at a distance of 1" will give rise to a substrate event generating more than 10^4 electrons on average every 3 μs. This is clearly unacceptable if typical decay times of pulses are 20 μs and a resolution of 0.1% is desired. One can either reduce the count rate or mask the substrate appropriately. For the experiments discussed in this thesis a 100 μCi source was found to be sufficiently weak. Future devices may be deposited on thin membranes, thereby greatly reducing the number of substrate events. This will be

essential for experiments with x-rays covering a wide energy range, such that substrate events from high energy x-rays do not obscure low energy x-ray peaks.

Comparing the total collected charge for a signal from the center of the absorber ($8 \cdot 10^6$ e^-) and from the substrate just underneath the center ($1.2 \cdot 10^6$ e^-) allows an estimate of the phonon transmission coefficient through the Ta-SiO_2 interface. If we assume that at most half the phonons from a substrate event propagate towards the absorber, we obtain an average phonon transmission coefficient of 0.3. This agrees roughly with an average of the literature values of 0.38 for the longitudinal and 0.13 for the transverse phonon modes [Kaplan, 1979].

5.2. Digital Filtering

For best resolution we integrate the unfiltered current waveforms numerically and apply digital filters. The best filter is determined by optimizing the resolution of electronic pulses which are injected into the junction during x-ray measurements. Their pulse shapes are taken from the model simulation and match the x-ray induced pulses from the center of the absorber. That ensures that the same filters optimize the resolution of electronic and x-ray induced pulses.

We typically use Butterworth filters and determine the optimum cutoff frequencies and filter order empirically. Results with Bessel and Chebychev filters are comparable. Figure 5.2.1. shows the resolution of electronic pulses injected into the junction as a function of filter bandwidth and order.

In the current sensitive mode (no integration), the best resolution of 13 eV is obtained for a 5th order 65 kHz low pass filter. This resolution is not a sensitive function of filter order and bandwidth. In the charge sensitive mode, the best resolution is also 13 eV, but is obtained for a 4 to 65 kHz bandpass.

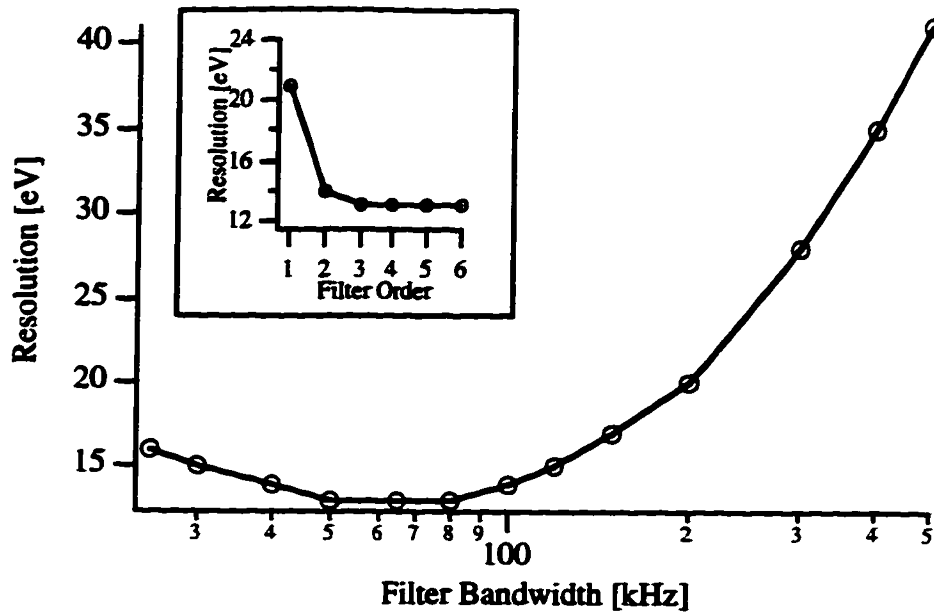

Figure 5.2.1.: Resolution of electronic pulses for different digital filters. The optimum bandwidth was determined using a fifth order filter. (8/2/96, T = 0.24K, $R_{dyn} \approx 10k\Omega$)

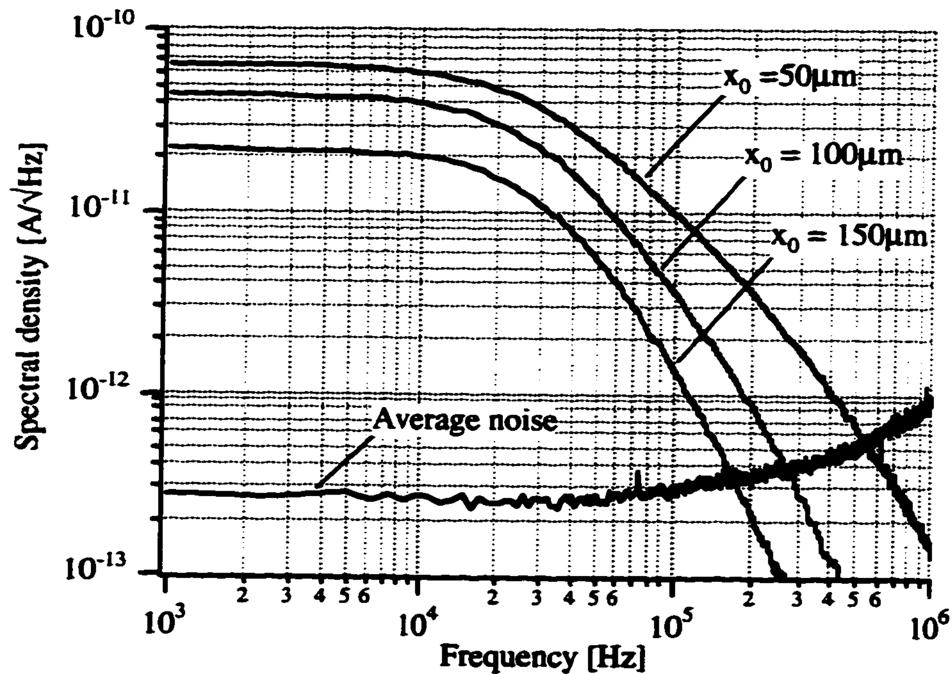

Figure 5.2.2.: Noise spectrum and signal spectrum for pulses absorbed at various distances x_0 from the detector junction. Pulses closer to the junction are faster and thus contain higher frequency components.

The upper cutoff frequency of 65 kHz corresponds to the frequency at which the noise spectrum starts to increase (figure 5.2.2). We find that the best resolution is obtained roughly by integration over the frequencies of maximum signal-to-noise density, as expected [Jochum, 1994].

There are several procedures outlined in the literature for optimum filtering of waveforms [Press, 1989; Szymkowiak, 1993; Irwin, 1995]. They are not straightforward to implement in our case, because they require an ideal pulse shape template with which to compare the noisy data. However, in our devices pulse shapes change significantly for different absorption locations. Work has started in our group to implement a position dependent optimum filter. The various templates can be obtained either by averaging groups of x-ray pulses from different locations or from the computer simulations.

5.3. Device Resolution

The filtered charge measurements from the two junctions are displayed in the scatter plot below (figure 5.3.1.). The main sequence of events corresponds to the stronger K_α line at 5.89 keV, the weaker sequence with larger charge is due to the K_β line at 6.49 keV. These events originate in the absorber.

Absorption events in the aluminum tunnel junctions and in the leads cause the two sequences of events along the axes. They are less frequent than the absorber events, because the characteristic x-ray absorption length is much longer in aluminum (35 μm at 6 keV) compared to tantalum (2 μm) [Brennan, 1992]. They produce signals in only one detector, because the large energy gap in tantalum prevents quasiparticles in the trap from traversing the absorber.

There exists a group of scattered events with smaller collected charge. They are partially due to absorption events in the SiO layer on top of the tantalum absorber. They

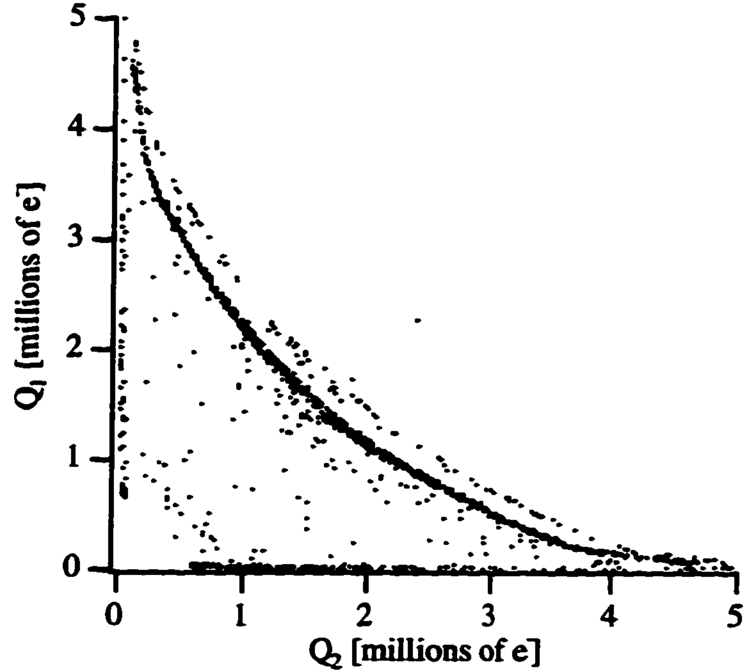

Figure 5.3.1.: Scatter plot of filtered charge pulses (8/2/96, T = 0.24K)

can also be caused by incomplete conversion of x-ray energy into quasiparticles in the initial energy relaxation process. The photoelectron produced by the absorption of an x-ray ionizes atoms along its path in the absorber. The holes are filled by outer shell electrons and energy is conserved either through emission of an Auger electron or an x-ray photon. Most of the secondary transitions are reabsorbed in the film and the relaxation process continues. However, if they escape, their energy is lost for the detection process and the observed total charge is reduced.

To analyze the performance of the devices we focus on the main sequence of events that are not affected by electron or photon escape. There remains a spatially varying total collected in this sequence due to the finite quasiparticle life time, as discussed in section 4.5. Quasiparticles generated in the center of the absorber are more likely to recombine before diffusing into the trap regions and being detected in one of the junctions. The charge output from the center of the absorber is therefore reduced resulting in a curvature of the scatter plot. To use these devices as spectrometers we must

be able to normalize out losses. We account for the finite quasiparticle lifetime using the analytic expression that relates the initial charge to the measured signals Q_1 and Q_2 and the absorption location (cf. chapter 2). For uniform quasiparticle loss, the initial charge Q_0 and absorption location x_0 can be calculated as [Kraus, 1989]

$$Q_0 = \sqrt{Q_1^2 + Q_2^2 + 2Q_1Q_2\cosh(\alpha)}$$
$$x_0 = \frac{L}{2\alpha}\ln\left(\frac{Q_1e^{-\alpha/2} + Q_2e^{\alpha/2}}{Q_1e^{\alpha/2} + Q_2e^{-\alpha/2}}\right) \quad 5.3.1.$$

The parameter $\alpha \equiv L/\sqrt{(D\tau_{loss})}$ is a measure for the magnitude of quasiparticle loss on a time scale of diffusion through the absorber. It is chosen to straighten out the curvature of the Q_1 vs. Q_2 scatter plot and has a value of 1.6 for this set of data. Equation 5.3.1. then allows us to project the charge measurements onto a plot of total charge vs. absorption location. The result is shown below. Events from the K_α line can be mapped onto a straight line, confirming the model assumption that uniform quasiparticle loss in the absorber accounts for the overall curvature of the Q_1 vs. Q_2 scatter plot.

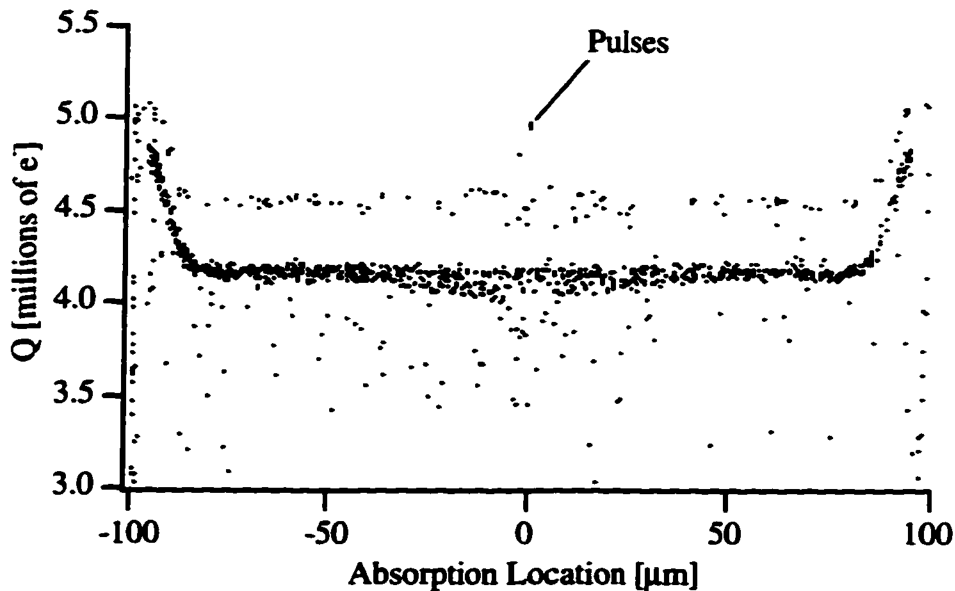

Figure 5.3.2.: Total charge vs. absorption location (filtered). (08/02/96) The width of the electronic pulses is 13 eV (T = 0.24K).

The collected charge increases at the edges where the aluminum trap overlaps the absorber, because the average gap is reduced and the initial charge increases accordingly. The charge increase does not occur discontinuously, but over a 5 μm length scale. This corresponds to the spatial extent of the hotspot during the initial relaxation.

Neglecting events from the overlap region, the device resolution is 87 eV full width at half maximum (FWHM) over a total length of 160 μm (figure 5.3.3.). It is limited by some excess broadening in the central region of the absorber. This is most likely caused by different degrees of quasiparticle loss at the niobium contact, as discussed in chapter 4. The resolution can be improved to 54 eV if only absorption events over a 30 μm range to the side of absorber are considered (figure 5.3.4).

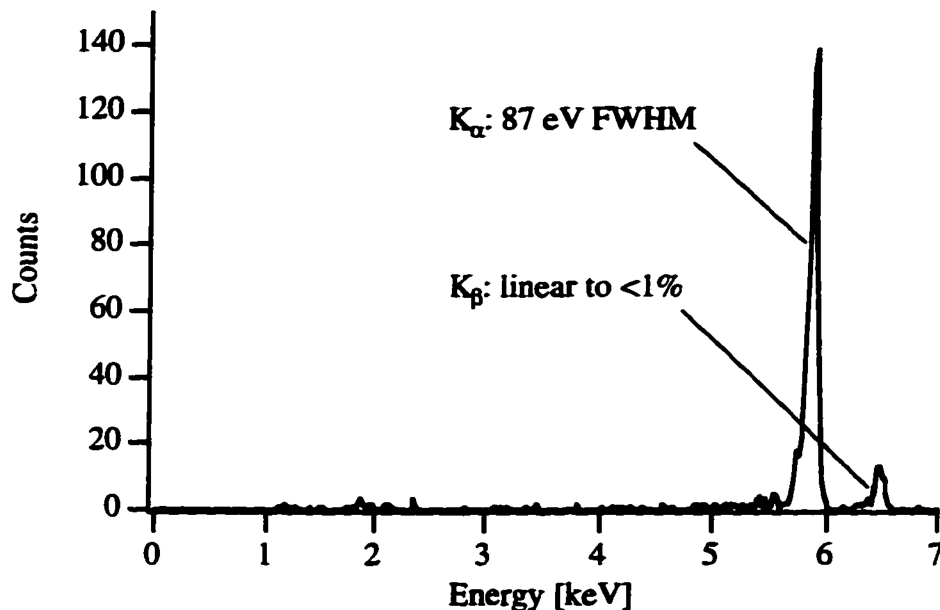

Figure 5.3.3.: Spectrum for events over entire length of absorber (08/02/96)

The linearity of the detector response can be tested from the ratio of collected charges for the two x-ray lines. For linear response, the charge ratio would scale like the x-ray energies $E(K_\beta)/E(K_\alpha) = 6490 \text{ eV}/5890 \text{ eV} \approx 1.102$. This agrees with the observed value of 1.099 ± 0.005 to better than 1%. The uncertainty in this measurement is due to

the small number of events in the K_β line, particularly when only events from a subsection of the absorber are considered. Within the present resolution of the device, the charge output is linear. Self-recombination of among excess quasiparticles does not affect the charge collection significantly.

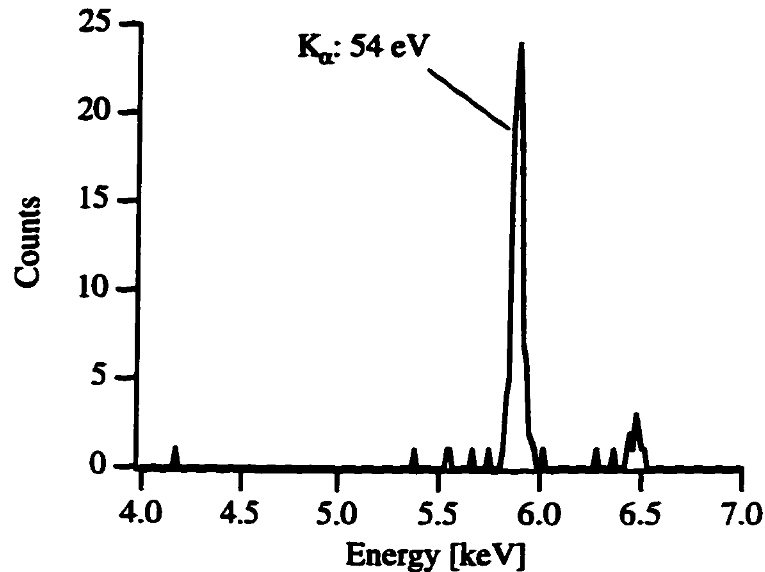

Figure 5.3.4.: Device resolution for the range $+50\ \mu m \leq x_0 \leq +80\ \mu m$ (08/02/96)

5.4. Spatial Resolution

The essential feature of our detectors is combined high spectral and spatial resolution. The spatial resolution of the device is expected to be of the same order as the energy resolution, i.e. around 1%. We will discuss these issues in more detail.

For a quantitative analysis the spatial resolution $\delta x_0/L$ can be calculated in terms of the measured energy resolution $\delta E_x/E_x$ by propagation of errors. It depends both on the absorption location x_0 and the loss parameter α. Assuming that both charge measurements are affected by the same error δQ, the expressions for spectral and spatial resolution are related through [Kraus, 1989]

$$\frac{\delta E_x}{E_x} = \frac{\delta Q}{Q}\sqrt{2 + \sinh^2(\alpha(1/2 + x_0/L)) + \sinh^2(\alpha(1/2 - x_0/L))}$$

$$\frac{\delta x_0}{L} = \frac{\delta Q}{Q}\sqrt{\left(\frac{\sinh(\alpha(1/2 + x_0/L))}{\alpha}\right)^2 + \left(\frac{\sinh(\alpha(1/2 - x_0/L))}{\alpha}\right)^2} \qquad 5.4.1.$$

We use the experimental energy resolution to determine the uncertainty in the charge measurement. A resolution of 87 eV centered around $x_0=0$ with $\alpha=1.6$ corresponds to an uncertainty $\delta Q/Q = 0.8\%$. The spatial resolution is then calculated to be 2 μm over an effective length of 160 μm, giving effectively 80 resolution with just two channels of readout. If only events over a 30 μm range centered around $x_0 = 65$ μm are considered, the energy resolution improves to 54 eV with a corresponding spatial resolution of 1 μm.

One might object that the spatial resolution cannot be better than the size of the initial hotspot. This is only true if the hotspot spreads out asymmetrically about the location of x-ray absorption. Given the numerous fast interactions in the initial energy relaxation and a range of 0.1 μm for the initial photoelectron [Zehnder, 1995], we do not expect the asymmetry to be more than 0.5 μm.

To illustrate the imaging capabilities of the device directly, we have irradiated the absorber through a mask with two 10 μm diameter pinholes spaced 50 μm apart. The histogram of absorption locations shows two peaks for events at the holes (figure 5.4.1.). The sharpness of the peak edges could, in principle, be used as a measure of the spatial resolution. Unfortunately, the finite distance between the mask and the absorber results in a half shadow whose width exceeds the intrinsic spatial resolution of the device.

To measure the spatial resolution directly, one would have to confine the absorption locations to a 1 μm spot. This is not possible by masking with our present experimental setup. Alternatively, one can photolithographically fabricate an absorber with spatially varying thickness such that the region of increased absorption is only 1 μm wide (figure 5.4.2.).

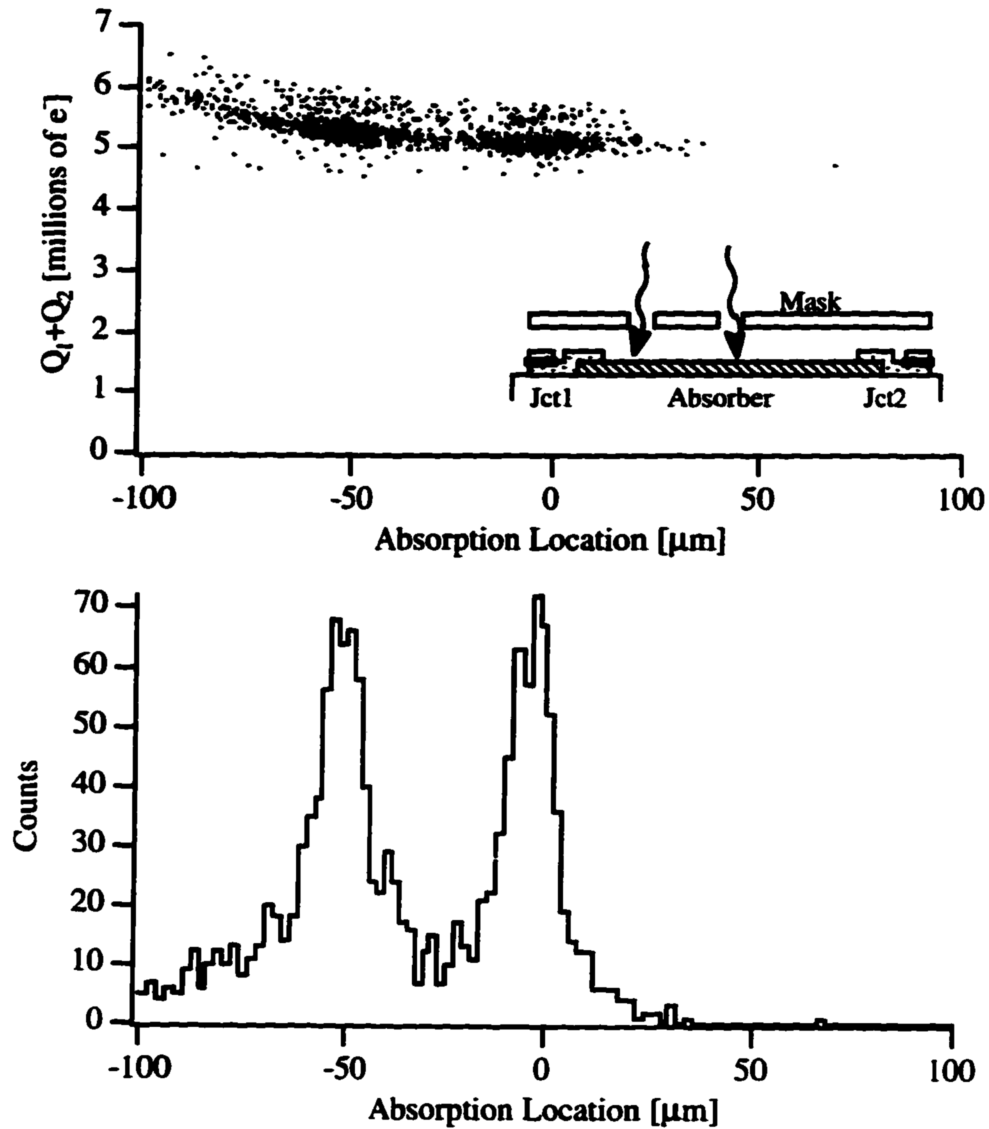

Figure 5.4.1.: Localized device irradiation, T = 0.3K (11/30/95, T = 0.30K)

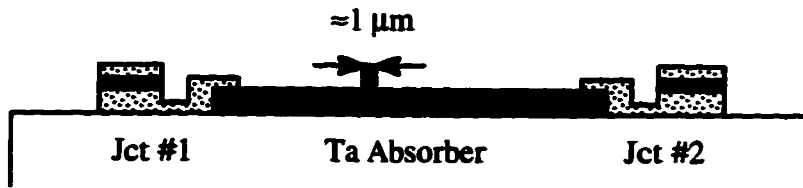

Figure 5.4.2.: Proposed detector design to measure spatial resolution directly

5.5. Discussion

The contributions to the device noise fall in roughly three categories: Electronic noise sources and other external disturbances, position dependent device responses and, ultimately, statistical fluctuations. We will summarize their relative contribution at present and suggest future experiments to reduce them.

Electronics

The electronic noise of injected pulses is 13 eV at T = 0.24 K, well below the device noise. It increases to 40 eV at 0.3 K, where the dynamic resistance of the device is only 1 kΩ and the voltage noise of the FET starts to dominate. In addition, bias voltage fluctuations of order 1 μV over a half hour run are observed. These fluctuations do not affect the width of the injected pulses, because device impedance is constant over at least ±5 μV around the bias point. However, the signal charge changes with bias, and a 1 μV fluctuation corresponds to a resolution broadening of 40 eV (chapter 4.4). This is possibly one of the limiting noise sources in our present setup [cf. Porter, 1996]. The origin of these fluctuations is not well understood at present and will be the focus of our work in the near future.

There are two possible ways to address the signal variations due to bias voltage fluctuations. One can either identify the sources of the fluctuations and reduce using more stable electronic components. Alternatively, one can use smaller junctions that can be biased at higher voltages, where the signal output depends less sensitively on bias and fluctuations therefore do not affect the resolution as much. Reducing the junction size would have the additional advantage of a reduced thermal dark current and an increased dynamic resistance for lower electronic noise.

Substrate events constitute another external source of noise if they overlap in time with an event from the absorber. Their influence on the resolution has been eliminated

by reducing the count rate (chapter 5.1.). It can also be made negligible by proper substrate masking. Switching events between different points on the I(V) curve have also been eliminated with the help of a dc voltage bias circuit (chapter 3).

Position Dependence

Charge output varying as a function of absorption position is commonly seen as a limiting factor in the device resolution [Gaidis, 1996; Luiten, 1996; Martin, 1996]. We will discuss position dependent charge collection for all three dimensions.

Charge variations in x-direction can be visualized directly with the detector's imaging capabilities. We observe an increase in device noise in the center of the absorber (figure 5.3.2). It can be attributed to quasiparticle loss at the niobium contact, most likely because of metallic NbO regions that serve as unwanted trapping sites. This appears to be the limiting factor in the device resolution at present.

There is a straightforward way to replace the niobium contact with a tantalum contact to one of the aluminum traps (figure 5.5.1.). There is no voltage drop between the two traps and both junctions can be biased as before. Since the two tantalum films are unconnected, quasiparticles from the absorber will scatter inelastically in the aluminum traps before being able to diffuse out the contact. In addition, this change in the device layout will simplify the fabrication process by removing one mask layer.

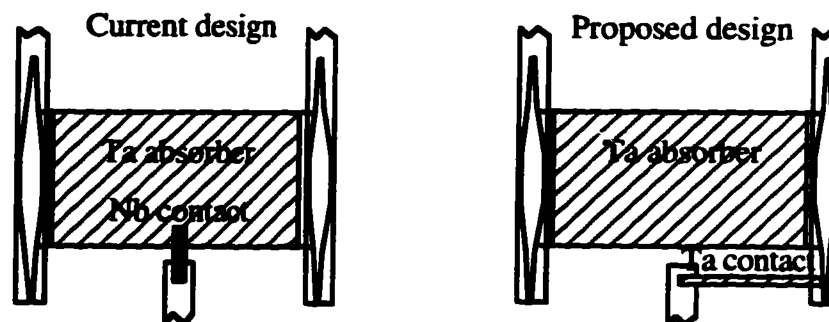

Figure 5.5.1.: Proposed detector design to remove quasiparticle losses at Nb contact. The Ta film is deposited first such that it contacts the bottom Al electrode.

There is some concern that some of the residual noise is due to different charge collection for absorption events with different y-coordinate. The wiring layer is asymmetric in y-direction about the center of the absorber and the quasiparticles can only diffuse out the leads on one side. Therefore, if the charge does not spread out evenly in y-direction in the junction area before the quasiparticles diffuse out the leads, one might expect different degrees of charge multiplication due to backtunneling. Simulations of the charge profile in y-direction for an absorption event 10 μm from the edge of the absorber show that the charge is spread out uniformly on a time scale much faster than typical current pulse time scales (figure 5.5.2.). After 1 μs, any non-uniformity in the charge distribution is already reduced below 1% in the junction region. This should reduce differences in backtunneling below detectable levels. Nonetheless, future devices will have a wiring layer symmetric about the center of the absorber.

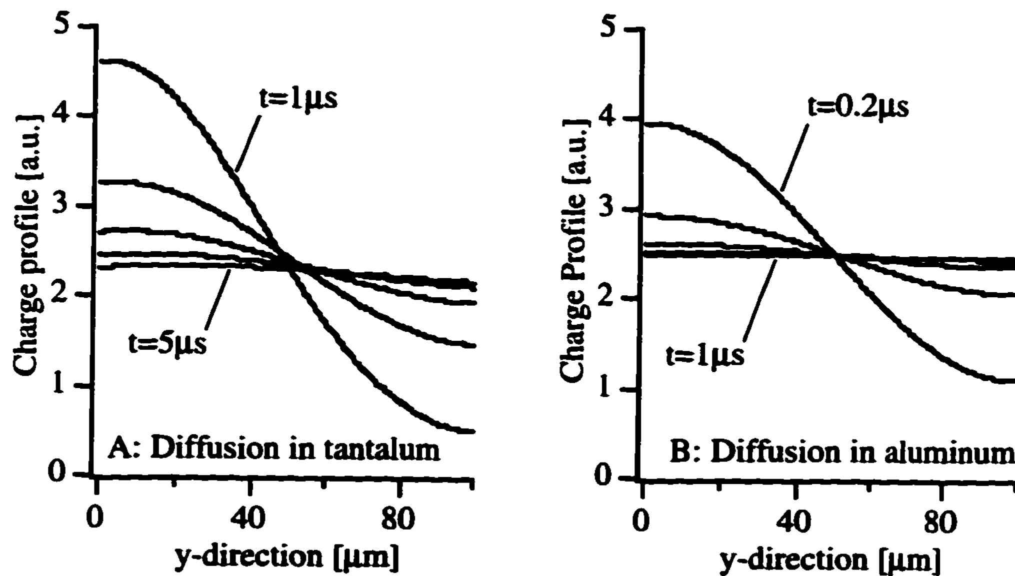

Figure 5.5.2.: Charge profiles in y-direction for an absorption event at y_0 = 10 μm. Note different equilibration times in tantalum (D_{Ta} = 8 cm^2/s) and aluminum (D_{Al} = 60 cm^2/s)

Finally, there could be variations in the initial charge with z-direction. Different absorption heights can result in different degrees of high energy phonon loss into the

substrate. This affects the energy-to-charge conversion efficiency. The magnitude of this effect is difficult to assess with present computer simulations. However, 1 ps after the x-ray absorption 60% of the x-ray energy resides in the phonon system and the hotspot is not yet evenly spread out through the absorber. A 1% fluctuation in energy-to-charge conversion certainly appears possible. This effect can be experimentally tested with different absorber thicknesses, as thinner absorber should show less z-dependence. If necessary, this problem can be eliminated by depositing the devices on a SiN membrane.

Statistics

With the changes outlines above, it appears possible to greatly improve the device performance. Ultimately, the resolution will be limited by statistical noise. There are three processes in our devices that produce statistical fluctuation: There are Fano limited fluctuations in the number of initially created charges of order 3 eV (chapter 2.1.). In addition, fluctuations associated with multiplication upon trapping are of the same order (chapter 4.2.). Finally, since we observe some increase in charge due to multiple tunneling (chapter 4.5.), there are additional fluctuations because the individual tunneling events are statistically independent. Their magnitude is given by [Goldie, 1994]

$$\delta E_{FWHM} = 2.355\sqrt{\varepsilon E_x G} \quad \text{with} \quad G = \frac{P_1 - P_1^2 + 3P_1P_2 + P_1^2P_2}{(P_1 + P_1P_2)^2}. \qquad 5.5.1.$$

For tunneling a probability from the trap $P_1 \approx 0.9$ and a probability $P_2 \approx 0.2$ for tunneling from the counterelectrode the noise contribution due to multiple tunneling is less than 6 eV. Therefore, none of the above statistical noise sources contribute significantly to the resolution at present. Once all other noise sources are suppressed sufficiently, the noise contribution caused by multiple tunneling can be eliminated with a wide aluminum wiring layer for fast quasiparticle diffusion away from the junction area such that backtunneling is eliminated ($P_2 = 0$).

Summary

In summary, we have identified quasiparticle loss at the niobium contact to the absorber, z-dependent energy-to-charge conversion and $1\mu V$ bias voltage fluctuations as the most likely limitations to the device resolution. Loss at the niobium contact can be eliminated by replacing it with a tantalum contact. Z-dependence can be addressed by depositing the devices on a SiN membrane. Fluctuation noise can be reduced with smaller junction areas that allow biasing at higher voltage where the charge varies less sensitively with bias.

Chapter 6: Summary

We have developed superconducting single photon x-ray detectors for x-ray astrophysics applications. A single tantalum absorber film is used in conjunction with two aluminum detector junctions, one on either side. X-ray photons generate excess charge in the absorber, which diffuse to the lower gap detector junctions, are trapped by inelastic scattering, and produce a tunneling current in both junctions. The sum of the signal charges is related to the x-ray energy, and their ratio provides information about the absorption location. One dimensional imaging is achieved with just two channels of readout. The devices have an absorber area of 200 μm by 100 μm and an absorption efficiency of 25% for 6 keV x-rays.

To read out the x-ray induced pulses we have designed a low noise current preamplifier with a dc voltage bias. The circuit's dc load line resistance of 6Ω is low compared to typical dynamical resistances of order 10 kΩ and allows stable biasing in the subgap region of the tunnel junction even if the dc Josephson current is not completely suppressed. With the device at temperature of 0.24K, the circuit has an electronic noise of 13 eV, dominated by the shot noise of the bias current. The amplifier has a 300 kHz signal bandwidth and amplifies x-ray induced current pulses with minimum waveform distortion.

The current pulses are analyzed to study quasiparticle dynamics inside the detector structures (Appendix B). The detector response over the entire absorber length can be described with a few parameters that are related to the time scales of the individual processes.

Quasiparticle diffusion constants are inferred from time-of-arrival measurements and diffusion is found to be unexpectedly slow in both tantalum (D_{Ta} = 8 cm^2/s) and aluminum (D_{Al} = 60 cm^2/s). This slow diffusion is possibly caused by intrinsic gap variations inside the tantalum absorber film. Trapping from the tantalum absorber into the

aluminum junctions is fast and effectively separates charges into the two detector junctions. Trapping occurs in the bulk aluminum region to the side of the absorber. It increases the charge by a factor of ≈1.6 when relaxation phonons break additional pairs in the lower gap aluminum.

Tunneling times are comparable to characteristic times for relaxation in the aluminum electrodes such that quasiparticles do not relax all the way to the gap edge before tunneling. There are competing bias dependent tunneling processes, some of which transfer charge in direction opposite to the applied bias. This causes the collected charge to vary sensitively with bias voltage. The slow quasiparticle diffusion in aluminum causes quasiparticles in the counterelectrode to tunnel back into the trap before diffusing out the leads. Backtunneling results in charge multiplication by a maximum factor of about 1.5.

Long quasiparticle lifetimes allow efficient charge collection. In the aluminum junction, the lifetimes are determined by recombination with the thermal quasiparticle background. In tantalum, the observed loss times of order 30 μs are temperature independent. They are possibly related to regions of reduced gap, either in regions of high impurity concentration or damage to the film or because of trapped flux.

The device resolution is 87 eV FWHM with an effective area of 160 μm by 100 μm. The corresponding spatial resolution is 2 μm over this effective length of 160 μm. At present, the resolution is limited by a varying number of quasiparticles lost at the niobium contact to the tantalum absorber. It can be improved to 54 eV spectral and 1 μm spatial resolution if the range of absorption locations is restricted and only events further away from the niobium contact are considered. The residual broadening of 54 eV is most likely caused by two effects. First, variations in the bias voltage cause fluctuations in the tunneling charge. Fluctuations of only 1 μV would produce excess noise of 40 eV. Second, the number of initial quasiparticles varies as a function of x-ray absorption height in the tantalum film, as different number of pair breaking phonons are lost to the substrate during the initial energy relaxation. Electronic noise, substrate events, temperature

fluctuations and switching between bias points no longer contribute to the device noise because of improvements in the experiments made in the course of this thesis.

The next detector design will address the present device limitations: The niobium contact to the absorber will be replaced by a tantalum contact to one of the traps. The junction size will be decreased to allow biasing at higher voltage where the charge varies less sensitively with bias. Different degrees of phonon loss to the substrate will be eliminated by placing the device on a thin membrane. With these changes, further improvements in the resolution below 10 eV seem possible.

Appendix A: Materials Parameters in Tantalum and Aluminum

For the quantitative analysis of device performance based on measured film properties, it is important to use materials parameters that go beyond free electron approximations. We will outline the procedures we have used to estimate the density of states and the Fermi velocity in tantalum and aluminum.

The density of states at the Fermi surface can be experimentally determined from low temperature measurements of the electronic specific heat according to

$$c_V = \gamma_0 T \text{ with } \gamma_0 = \frac{1}{3}\pi^2 k_B^2 n(E_F). \qquad \text{A.1.}$$

Here $n(E_F)$ is the band-structure density of states for both spin directions, i.e. it differs from the free electron density of states only through static electron-ion interactions. However, the measured value of γ is affected by electron-electron interactions (screening) and also dynamical electron-phonon interactions (phonon screening). Both effects increase γ and lead to an overestimate of $n(E_F)$. This happens physically, because some of the energy applied to the system heats the screening phonons and results in a lower measured temperature increase ΔT. Similarly, electron-electron interactions increase the electron's effective mass and enhance their specific heat. Both effects can be accounted for by renormalizing the measured values of γ by a material specific factor $(1 + \lambda_{e\text{-}ph} + \lambda_{e\text{-}e})$.

We use an average over published literature values for γ [Gschneidner, 1964] and the electron-phonon renormalization factor $\lambda_{e\text{-}ph}$ [McMillan, 1967; Kaplan, 1976]. Corrections $\lambda_{e\text{-}e}$ due to electron-electron interactions are comparably small [Gell-Mann, 1957]. The results are summarized in the table below.

The Fermi velocity in a metal can be either experimentally determined from measurements of the anomalous skin effect, or it can be theoretically predicted from band structure calculations.

For aluminum, we follow the literature [VanDuzer, 1981] and obtain the total Fermi surface area S_F from surface impedance measurements in the anomalous skin effect, keeping in mind that the data used fluctuate by about ±10% [Faber, 1954]. However, when extracting the average Fermi velocity from the Fermi surface area according to

$$n(E_F) = \frac{1}{4\pi^3\hbar}\int\frac{dS_F}{v_F} = \frac{S_F}{4\pi^3\hbar}\overline{\left\langle\frac{1}{v_F}\right\rangle}, \qquad \text{A.2.}$$

we use a value of the density of states that has been corrected for screening effects as discussed above and obtain a value of $v_{F,Al} = 2.2 \pm 0.6 \cdot 10^6$ m/s.

To our knowledge, no measurements of the anomalous skin effect in tantalum have been published. Band structure calculations [Mattheis, 1970] in good agreement with experimental data [Halloran, 1970] are available, which do, however, only list values of the band structure effective mass $m^*|_{bs}$ and extremal cross sectional areas of the Fermi surface A_F. We approximate the Fermi velocity through

$$v_F = \frac{\hbar k_F}{m^*} \text{ with } m^*|_{total} = m^*|_{bs}(1+\lambda_{e-ph}+\lambda_{e-e}) \qquad \text{A.3.}$$

such that both band structure and screening corrections to the free electron model are included. This approximation effectively assumes a parabolic dispersion relation (constant m^*) in the relevant bands. We extract the Fermi wave vector k_F through $A_F=\pi k_F^2$. That assumes k_F is a reasonable approximation to the average radius of the cross sectional area. Including the corrections due to screening, we average the contributions of the different bands and obtain for tantalum $v_{F,Ta} = 3.6 \pm 0.8 \cdot 10^6$ m/s. The comparably large error bars

reflect the variations of v_F in the various bands and the systematic uncertainties in the above derivation. It is somewhat reassuring that this value of the Fermi velocity agrees reasonably well with the measured coherence length of $\xi_0 = 925 \pm 40$ Å in pure tantalum [Auer, 1973] according to the BCS prediction $\xi_0 = 0.18\hbar v_F / k_B T_C$. The table below summarizes the numbers used in this dissertation.

	Tantalum	Aluminum
γ [mJ/moleK^2]	5.88 ± 0.28	1.36 ± 0.01
n [atoms/cm^3]	$5.4 \pm 0.1 \cdot 10^{22}$	$6.0 \pm 0.1 \cdot 10^{22}$
$\lambda_{e\text{-}ph}$	0.7 ± 0.05	0.4 ± 0.05
$\lambda_{e\text{-}e}$	0.2 ± 0.04	0.2 ± 0.04
$n(E_F)$ [states/eVcm^3]	$7.1 \pm 0.3 \cdot 10^{22}$	$2.2 \pm 0.2 \cdot 10^{22}$
v_F [m/s]	$3.6 \pm 1.0 \cdot 10^5$	$2.2 \pm 0.4 \cdot 10^6$

Table App. A: Materials parameters of tantalum and aluminum

Appendix B: Summary of Important Runs

Date (Ref.)	Device/ Source	T [K]	R_{dyn} [kΩ]	DC bias	Crosstalk? / Pickup?	Noise [pA/√Hz]	Pulses [eV]	X-rays [eV]	Range [μm]	Physics issues studied/ Conclusions
08/12/95	Ta 30 mCi	0.3	1	I	Y / ?	--	87	176	160	148 eVwith current pulses switching events straight Q_1 vs. Q_2 scatter plot
11/20/95 Ch. 5.1 4.3	Ta/Al 30 mCi	0.29	4	I	Y / N	0.4	40	116	60	Slow trapping in Ta/Al device Substrate events add to noise
11/30/95 Ch. 5.4	Ta/Al 30 mCi	0.30	1	I	Y / N	0.5	--	128	≈30	Two pinhole mask: masking does not improve resolution
12/07/95 Ch. 4.3	Ta 0.5 mCi	0.31 0.34	1.5 0.5	I	Y / N	0.6	44	48	23	Straight Q_1 vs. Q_2 suspect slow diffusion
07/01/96	Ta 0.5 mCi	0.24	10	V	N / Y	0.25 + pickup	--	120	160	Curved Q_1 vs. Q_2, surprising $D_{Ta} = 8\ cm^2/s$
08/02/96 Ch. 3.3 5.3,5.4	Ta 0.5 mCi	0.24	10	V	N / N	0.25	13	87 54	160 30	Curved Q_1 vs. Q_2 Noise vs. bias Mac and scope screens off
08/07/96 Ch. 4.5	Ta 0.5 mCi	0.24 0.28 0.34	10 4 0.5	V	N / N	0.3 0.5 0.9	20 30 48	88 / 54 92 / 61 133	160 / 35 160 / 30 140	Curved Q_1 vs. Q_2 for all T No distortion of inj. pulses Fit $Q(x_0)$ and $I_{pp}(x_0)$ with one set of parameters
10/17/96 Ch.4.2	Ta/ Al 0.5 mCi	0.24	10	V	N / N	0.25	--	116	35	$D_{Al} = 60\ cm^2/s$: understand origin of backtunneling $\tau_{trap} \approx 10\ \mu s$ for Ta/ Al device
01/20/97 Ch. 4.4	Ta 0.5 mCi	0.24	10	V	N / Y	0.3	13	102	160	Bias test, V_{bias} fluctuates Curved Q_1 vs. Q_2 for all V_{bias} Explain Q vs. V_{bias}

Note: All devices are from fabrication run XN93. For details of the fabrication process, see [Gaidis, 1994]
The entry in the first column refers to the chapter in which the data are discussed.

Appendix C: Device Parameters for Sample XN93

Sample dimensions:

Absorber: 200 μm x 100 μm x 6000 Å ⇒ 12000 μm^3

Trap: 1500 Å x 4700 μm^2 ⇒ 700 μm^3

Counterelectrode + wiring: 3700 Å x 35 μm x 220 μm ≈ 2800 μm^3

Junction area: 1750 μm^2

Fabrication:

Ta absorber: 6000 Å dc sputtered at 40 Å/s and a substrate temperature of 700 °C

⇒ $\rho_{N,Ta}$ = 14.5 μΩcm at room T, RRR = 30

Nb contact: 2000 Å dc sputtered at 10 Å/s

Al trap: 1500 Å thermally evaporated at 200 Å/s

⇒ $\rho_{N,Al}$ = 2.9 μΩcm at room T, RRR = 13

Barrier: Thermal oxide (room T) in 600 mTorr of oxygen for 3 hours

Al counterelectrode: 700 Å thermally evaporated at 15 Å/s

SiO insulator: 1500 Å thermally evaporated at 14 Å/s

Al wiring: 3000 Å thermally evaporated at 40 Å/s

Junction characteristics:

Normal state resistance: R_{NN} = 0.5 Ω

Critical current density: j_C = 30 A/cm^2; I_C = 500 μA

Bias current (V_{bias} = 70 μV): 30 nA (0.24 K); 100 nA (0.27 K); 300 nA (0.3 K)

Maximum R_{dyn}: ≈10 kΩ (0.24 K); 5 kΩ (0.27 K); 1 kΩ (0.3 K)

References

Auer, J., H. Ullmaier, *Phys. Rev.* **B7**, 136 (1973)

Bardeen, J., L.N. Cooper, J. Schrieffer, *Phys. Rev.* **108**, 1175 (1957)

Bardeen, J., *Phys. Rev. Lett.* **6**, 57 (1961)

Booth, N.E., *Appl. Phys. Lett.* **50**, 293 (1987)

Booth, N.E., G.L Salmon, (ed.) *"Low Temperature Detectors for Neutrinos and Dark Matter IV"*, Gif-sur-Yvette Cedex, France: Editions Frontieres (1992)

Bostock, J.L., M.L.A. Vicar, in *"Anisotropy Effects in Superconductors"*, Plenum Press, New York (1976)

Brennan, S., *Rev. Sci. Inst.* **63**, 850 (1992)

Brogiato, L., D.V. Camin, E. Fiorini (ed.),*"Low Temperature Detectors for Neutrinos and Dark Matter III"*, Gif-sur-Yvette Cedex, France: Editions Frontieres (1990)

Broom, R.F. *IBM J. Res. Dev.* **24**, 178 (1980)

Charles, P.A., F.D. Seward, *"Exploring the X-Ray Universe"*, Cambridge University Press (1995)

Chi, C.C., M.M.T. Roy, D.C. Cronemeyer, *Phys. Rev.* **B23**, 124 (1981)

de Gennes, P.G., *Rev. Mod. Phys.* **36**, 225 (1964)

de Korte, P.A.J., M.L. van den Berg, M.P. Bruijn, M. Frericks, J.B. le Grand, J.G. Gijsbertsen, E.P. Houwman, J. Flokstra, *Proc. SPIE* **1743**, 24 (1992)

Dubeck, L., K.S.L. Setty, *Phys. Lett.* **27A**, 334 (1968)

Eck, R.E., D.J. Scalapino, B.N. Taylor, in *Proc. 9th Intl. Conf. on Low Temp. Phys.*, ed. by J.G. Daunt, (New York: Plenum), 415 (1964)

Faber, T.E., A.B. Pippard, *Proc. Roy. Soc.* **A231**, 336 (1955)

Face, D.W., D.E. Prober, *J. Appl. Phys.* **62**, 3257 (1987)

Fano, U., *Phys. Rev.* **72**, 26 (1947)

Fiske, M.D., *Rev. Mod. Phys.* **36**, 221 (1964)

Frank. M., C.A. Mears, S.E. Labov, F. Azgui, M.A. Lindemann, L.J. Hiller, H. Netel, A. Barfknecht, *Nucl. Inst. Meth.* **A370**, 41 (1996)

Friedrich, S., K. Segall, M.C. Gaidis, C.M. Wilson, D.E. Prober, P.J. Kindlmann, A.E. Szymkowiak, S.H. Moseley, accepted for publication in *IEEE Trans. Appl. Supercond.* **7** (1997)

Gaidis, M.C. *"Superconducting Tunnel Junctions as Single Photon X-Ray Detectors"*, Ph.D thesis, Yale University (1994)

Gaidis, M.C., S. Friedrich, K. Segall, D.E. Prober, A.E. Szymkowiak, S.H. Moseley, *IEEE Trans. Appl. Supercond.* **6**, 1 (1996)

Gaitskell, R.C. *"Non-Equilibrium Superconductivity in Niobium and its Application to Particle Detection"*, Ph.D. Thesis, University of Oxford (1993)

Gell-Mann, M., *Phys. Rev.* **106**, 369 (1957)

Gijsbertsen, J.G., *"Superconducting Tunnel Junctions for X-Ray Detection"*, Ph.D. thesis, University of Twente (1995)

Girard, T.A., A. Morales, G. Waysand (eds.), *"Proceedings of the International Workshop on Superconductivity and Particle Detection"*, (Toledo, Spain) Singapore: World Scientific (1995)

Gschneidtner, K.A., *Solid State Phys.* **16**, 275 (1964)

Goldie, D.J., P.L. Brink, N.E. Booth, G.L. Salmon, *Appl. Phys. Lett.* **64**, 954 (1994)

Golubov, A.A., E.P. Houwman, J.G. Gijsbertsen, J. Flokstra, H. Rogalla, J.B. leGrand, P.A.J. deKorte, *Phys. Rev.* **B49**, 12953 (1994)

Golubov, A.A., E.P. Houwman, J.G. Gijsbertsen, V.M. Krasnov, J. Flokstra, H. Rogalla, M.Y. Kuprianov, *Phys. Rev.* **B51**, 1073 (1995)

Graeme, J., *"Photodiode Amplifiers"*, McGraw-Hill, New York (1995)

Gray, K., *J. Phys. F. Metal Phys.* **1**, 290 (1971)

Gray, K., *Appl. Phys. Lett.* **32**, 392 (1978)

Gutsche, M., P. Hettl, J. Jochum, B. Kemmather, H. Kraus, *Nucl. Inst. Meth.* **A370**, 91 (1996)

Halbritter, J., *Appl. Phys.* **A 43**, 1 (1987)

Halloran, M.H., J.H. Condon, J.E. Graebner, J.E. Kunzler, F.S.L. Hsu, *Phys. Rev.* **B1**, 366 (1970)

Horowitz, P., W. Hill, *"The Art of Electronics"*, 2nd ed., Cambridge University Press, Cambridge (1989)

Irwin, K.D., *Appl. Phys. Lett.* **66**, 1998 (1995a)

Irwin, K.D., *"Phonon Mediated Particle Detection Using Superconducting Tungsten Transition Edge Sensors"*, Ph.D. thesis, Stanford University (1995b)

Jochum, J., H. Kraus, M.Gutsche, B. Kemmather, F.v. Freilitzsch, R.L. Mössbauer, *Ann. Physik* **2**, 611 (1993)

Jochum, J., H. Kraus, M.Gutsche, B. Kemmather, F.v. Freilitzsch, R.L. Mössbauer, *Nucl. Inst. Meth.* **A338**, 458 (1994)

Josephson, B.D., *Phys. Lett.* **1**, 251 (1962)

Kaplan, S.B., C.C. Chi, D.N. Langenberg, J.J. Chang, S. Jafarey, D.J. Scalapino, *Phys. Rev.* **B14**, 4854 (1976)

Kaplan, S.B., *L. Low Temp. Phys.* **37**, 343 (1979)

Keller, W.E., *Phys. Rev.* **98**, 1571 (1955)

Kraus, H., F. v. Freilitzsch, J.Jochum, R.L. Mössbauer, T. Peterreins, F. Pröbst, *Phys. Lett.* **B 321**, 195 (1989a)

Kraus, H., *"Quasiteilchen-Einfang in Supraleitenden Tunneldioden - Ein neues Detektorkonzept"*, Ph. D. Thesis, Technical University Munich (1989b)

Kraus, H., private communication.

Kurakado, M., *Nucl. Inst. Meth* . **A196**, 275 (1982)

Lounasmaa, O.V., *"Experimental Principles and Methods below 1K"*, Academic Press, London (1974)

Labov, S.E., and B.A. Young, *"Proceedings of the Fifth International Workshop on Low Temperature Detectors"*, J. Low. Temp. Phys. **93**, Nos. 3/4 (1993)

Labov, S.E. L.H. Hiller, C.A. Mears, M. Frank, H.Netel, F. Azgui, A.T. Barfknecht, *IEEE Trans. Appl. Supercond.* **5**, 3034 (1995)

Luiten, O.J., L.J. van Lieshout, F.A. Michels, P. Valko, M.P. Bruijn, F. Kiewiet, P.A.J. de Korte, D.J. Adlerhof, A.W. Hamster, C.G.S. Brons, J. Flokstra, *Nucl. Inst. Meth.* **A370**, 72 (1996)

Martin, J., S. Lemke, R. Gross, R.P. Hübener, P. Videler, N. Rando, T. Peacock, P. Verhoeve, F.A. Jansen, *Nucl. Inst. Meth.* **A370**, 88 (1996)

Mate, C.F., R. Harris-Lowe, W.L. Davis, J.G. Daunt, *Rev. Sci. Inst.* **36**, 369 (1965)

Mattheis, L.F., *Phys. Rev.* **B1**, 373 (1970)

McCammon, D. W. Cui, M. Juda, P. Plucinski, J. Zhang, R.L. Kelley, S.S. Holt, G.M. Madejski, S.H. Moseley, A.E. Szymkowiak, *Proc. PANIC XII*, **A527**, 821c (1991)

McMillan, W.L., *Phys. Rev.* **167**, 331 (1967)

McMillan, W.L., *Phys. Rev.* **175**, 537 (1968)

Mears, C.A., S.E. Labov, A.T. Barfknecht, *Appl. Phys. Lett.* **63**, 2691 (1993)

Mears, C.A., S.E. Labov, M. Frank, M.A. Lindemann, L.J. Hiller, H. Netel, A. Barfknecht, *Nucl. Inst. Meth.* **A370**, 53 (1996)

Nahum, M., J.M. Martinis, *Appl. Phys. Lett.* **66**, 3203 (1995)

Narayanamurti, V., R.C. Dynes, P. Hu, H. Smith, W.F. Brinkman, *Phys. Rev.* **B18**, 6041 (1978)

Netel, H., M. Frank, S. Labov, G.H. Campbell, C.A. Mears, E. Brunet, L.J. Hiller, M.A. Lindemann, *Nucl. Inst. Meth.* **A370**, 47 (1996)

Ott, H.R., A. Zehnder (eds.), *"Proceedings of the Sixth International Workshop on Low Temperature Detectors"*, Amsterdam: Elsevier (1996)

Peterson, R.L., *Cryogenics* **31**, 132, (1991)

Porter, F.S., D. van Vechten, M.G. Blamire, G. Burnell, *Nucl. Inst. Meth.* **A370**, 50 (1996)

Press, W.H., B.P. Flannery, S.A. Teukolsky, W.T. Vetterling, *"Numerical Recipes in Pascal"*, Cambridge University Press (1989)

Pernic, R., Yerkes Observatory, Williams Bay, WI, (414) 245-5555, private communication (1995)

Richards, P.L., *J. Appl. Phys.* **76**, 1 (1994)

Rando, N., Nucl. Inst. Meth. **A313**, 173 (1992)

Roberts, T.R., S.G. Sydoriak, *Phys. Rev.* **98**, 1672 (1955)

Roberts, T.R., *J. Natl. Bur. Stand.* **68A**, 567 (1964)

Rogovin, D., D.J Scalapino, *Ann. Phys.* **86**, 1 (1974)

Rothwarf, A., B.N. Taylor, *Phys. Rev. Lett.* **19**, 27 (1967)

Rothmund, W., A. Zehnder in *"Superconductive Particle Detectors"* , A. Barone (ed.), Singapore: World Scientific (1988)

Swihart, J.C., *J. Appl. Phys.* **32**, 461 (1961)

Szymkowiak, A.E., R.L. Kelley, S.H. Moseley, C.K., *J. Low Temp. Phys.* **93**, 281 (1993)

Twerenboldt, D., *Phys. Rev.* **B34**, 7748 (1986)

Usadel, K.D., *Phys. Rev. Lett.* **25**, 507 (1970)

Van Duzer, T., C.W. Turner, *"Principles of Superconducting Devices and Circuits"*, Elsevier North Holland, New York (1981)

Verhoeve, P., N. Rando, P. Videler, A. Peacock, A. van Dordrecht, D.J. Goldie, L.M. Lumley, J. Howley, M. Wollis, R. Venn, *SPIE Proc.* **2283**, 172 (1994)

Verhoeve, P., N. Rando, A. Peacock, A. van Dordrecht, D. Lumb, D.J. Goldie, R. Venn, Nucl. Inst. Meth. **A370**, 136 (1996)

Verhoeve, P., N. Rando, A. Peacock, A. van Dordrecht, A. Poelaert, D.J. Goldie, to be published in *IEEE Trans. Appl. Supercond.* **7** (1997)

White, G.K., *"Experimental Techniques in Low Temperature Physics"*, Clarendon Press, Oxford (1989)

Wollmann, D.A., K.D. Irwin, G.C. Hilton, J.M. Martinis, *Bull. Am. Phys. Soc.* **42**, No. 1, 142 (1997); presented at the APS March Meeting, Kansas City (1997)

Zehnder, A., *Phys. Rev.* **B52**, 12858 (1995)